RICE UNIVERSITY

Bleach Imaged Plasmon Propagation (BIIPP) of Metallic Nanoparticle Waveguides

by

David Enrique Solis Jr.

A THESIS SUBMITTED IN PARTIAL FULFILLMENT OF THE REQUIREMENTS FOR THE DEGREE

Doctor of Philosophy

APPROVED, THESIS COMMITTEE:

Stephan Link,
Assistant Professor of Chemistry,
Assistant Professor of Electrical and Computer Engineering

Christy Landes,
Assistant Professor of Chemistry,
Assistant Professor of Electrical and Computer Engineering

Bruce Johnson
Distinguished Faculty Fellow
Department of Chemistry

HOUSTON, TEXAS

April 5, 2013

ABSTRACT

Bleach Imaged Plasmon Propagation (BlIPP) of Metallic Nanoparticle Waveguides

by

David Enrique Solis Jr.

The high speed transfer of information in materials with dimensions below the sub-diffraction limit is essential for future technological developments. Metallic nanoparticle (NP) waveguides serve a unique role in efficient energy transfer in this size regime. Light may be confined to metallic structures and propagate along the surface of the waveguide via propagating plasmon waves known as surface plasmon polaritons (SPPs). Plasmon propagation of energy in metallic structures is not perfect however and damping losses from the waveguide material lead to a characteristic exponential decay in the plasmon near field intensity. This decay length is known as the propagation length and serves as an excellent metric to compare various waveguide materials and structures to one another at particular excitation wavelengths.

This thesis presents recent work in the development of a novel measurement technique termed bleach imaged plasmon propagation (BlIPP). BlIPP uses the photobleaching property of fluorophores and far field fluorescence microscopy to probe the near-field intensity of propagating plasmons and determine the propagation length. The experimental setup, image analysis, conditions, and application of BlIPP are developed within this thesis and an in depth review of the 1-photon photobleaching mechanism is also investigated.

The BlIPP method is used to investigate long plasmon propagation lengths along straight chains of tightly packed Au NPs through the coupling of light to sub-radiant

propagating modes, where radiative energy losses are suppressed. The findings of this work reveal, experimentally, the importance of small gap distances for the propagation of energy. Complex chain architectures are then explored using BlIPP measurements of tightly packed straight and bent chains of spherical silver NPs. We observe the highly efficient propagation of energy around sharp corners with no additional bending losses.

The findings of this thesis demonstrate the advantages and capabilities of using BlIPP propagation length measurement. Further, BlIPP is used to reveal the advantage of coupling light to sub-radiant modes of NP chains, which demonstrate the ability to guide light efficiently across long distances and around complex structures, bringing us a step closer to the goal of applying plasmonic devices and circuitry in ultra compact opto-electronic devices.

To my loving parents David and Gloria Solis,
and to the memory of my cousin Jesus Juan Esquivel (J. J.),
you were with me every step of the way.

ACKNOWLEDGEMENTS

I would firstly like to thank my advisor and mentor Stephan Link for his guidance and support throughout the PhD. Working with Stephan during a summer REU inspired me to apply for graduate level studies and go for the PhD. His leadership both academically and personally have been essential to my development as a scientist. It has been both a pleasure and a privilege working with him.

Special thanks to professor Christy Landes for her support and guidance throughout the PhD. Thanks also to Naomi Halas and Peter Nordlander, whose experience and expertise have brought forward questions and conversations, which in turn have lead to new perspectives, insights, and motivations for my research. Thanks also to my professors from the University of Dallas, Richard Olenick, David Andrews and my physics mentor Dr. Sally Hicks, who prepared me well to face the many challenges of an experimentalist with creativity and resourcefulness.

Thanks also to Professors Bruce Johnson and Kevin Kelly whose mentorship on a personal level throughout graduate school have been essential to navigating the many struggles that an applied physics graduate student encounters daily. I'm also thankful to you both for volunteering me into APGSA. Your support has been invaluable. Thanks also to Jennifer Burnett, Chad Byers, Brent Carey, Eteri Svanidze, and Matt Turner for helping to start and continue this group into the future.

I would also like to thank the many administrative assistants and staff members that have helped behind the scenes to keep Rice research running smoothly. Special thanks to Carolyn Aresu, Gabriela Galvan, Sofia Medrano, Umbe Cantu, Theresa Chatman and my favorite Cowboys fan Sue Friend.

I'm blessed to have been part of such a great lab where I am constantly surrounded by brilliant researchers and friends. Thanks to Aniruddha Paul, Sergio Dominguez-Medina, Britain Willingham, Liane Slaughter, Wei-Shun Chang, Lin-Yung Wang, Scott Nauert, Jana Olson, Pattanawit Swanglap, Saumyakanti Khatua, Alexei Tcherniak, Carmen Reznik, Nick Taylor, Charlisa Daniels, Lydia Kisley, Leonid Vigderman, Kui Bao, Bishnu Khanal, Yurong Zhen, Andres Rodela, Dorianne Castillo-Rivera, Dena Wiltz, Sean Walsh and all members of the Stephan and Christy supergroup. Working with you guys has made graduate school a truly awesome experience.

I've made so many great friends at Rice that I don't think I could thank them all in these pages, so I'll leave them with this: "Valhalla, I salute you, and all those who enter your halls. May your kegs never run dry, your sandwiches always stay fresh and your supply of Reese's Pieces never go empty! Viva Valhalla!"

Finally, and most importantly, I thank God, my parents David and Gloria Solis, my brothers Jason and Kevin, my bros from UD, James Taula'i, Jose Tovar, David Okun, and Rafael Carrasco, my grandfather Pedro Esquivel, the Esquivel's, the Forney's, the Cortez's, the Solis's, the Rodriguez's, and all the rest of the familia. I am who I am because of you; words can never express how much your love and support mean to me.

TABLE OF CONTENTS

LIST OF FIGURES

66 nW acquired with an integration time of 10 ms/pixel. The large gap in fluorescence in the middle of the NW (highlighted by the dotted line) was created by photobleaching the dye by direct excitation at that spatial location by 785 nm laser light at an exposure power of 10 μW for 5 minutes. **(e)** Fluorescence image of the same area in **d** after exposure to 10 μW of 785 nm laser light for 40 minutes at the left end of the NW. **(f)** Difference image created by subtracting **e** from **d**. Photobleaching due to plasmon propagation is clearly visible along the entire length of the NW despite the noticeable gap in the fluorescence in the middle of the wire. The sample was prepared by drop-casting a solution of Au NWs (12-18 μm x 50-100 nm) onto a cleaned glass slide. The thin film dye coating was created by spin coating 30 μL of a 0.05% solution of cardiogreen in methanol onto the sample at 6000 rpm. No methanol rinse was performed after the spin coating procedure, which causes a larger residual background fluorescence in these images compared to the NP chains. Both Au NWs were found to have comparable propagation distances indicating that the presence of the dye has no significant effect on the determination of the propagation distance. This experiment was performed because gain media like dye molecules can in principle compensate absorption losses and therefore enhance the plasmon propagation distance. This however, requires strong optical pumping of the gain medium

taken at the same location as the extinction spectra. **(B)** 785 nm excitation BlIPP difference image of the AgNP chain after bleaching for 20 min. at a bleach power of 12.6 μW. **(C)** Width average line section BlIPP data at 785 nm excitation is shown in red. The BlIPP fit in green yields a propagation length of L_0 = 3.6 μm. The blue line shows the photobleaching associated with direct excitation from the laser beam.

CHAPTER 1

INTRODUCTION

1.1 Motivation and background

Movies, music, internet, and an entire catalog of applications can all be accessed and displayed on a device that fits in the palm of your hand. The demand for high speed, miniaturized electronic devices continues to increase, and with it the need to develop new technologies capable of supporting high speed broadband information transfer at the nanoscale.[1, 2]

In small electronic processor chips the mechanism involved when transporting information is the movement of electrons through a conductive wire from one point to another. Pattern design techniques used to create wires and components on a chip such as electron beam lithography have made it possible to design structures with features down to ~5 - 10 nm.[3, 4] However, despite the ability to write structures in this size regime, leakage current in transistors, thermal noise, and crosstalk can lead to false bits and calculation errors, thus holding back the writing technology from practical miniaturization below 40 nm.[5, 6] Further, using electrons to transfer information limits the device to the speed of an electron in a wire, known as the communications bottleneck.[7] For very small wires, as used in processor chips, the delay time of electrons traversing a wire may be larger than the switching time for a transistor. To counter these disadvantages in speed and design size, engineers have created chips with parallelized processor architectures. These complex designs allow for higher processing speeds

because two or more processors are designed to work together in processing information simultaneously. However the speed of an electron traversing the wire remains unaffected.

Electronic optical interconnects offer several advantages which traditional electronics could never deliver. For example, fiber optics rely on the ability to guide light waves in various wavelength ranges at speeds ~0.67 times the speed of light in a vacuum (the speed of light in glass), yielding a delay time ~ 0.2 ps / mm of cable, which is approximately 35 times faster than the delay time of an electron traveling through a wire in a chip (7 ps / mm in Si wire on SiO_2)[6]. Another large advantage is the ability to send multiple wavelengths of light along the same fiber optic cable where each wavelength represents a different stream of information. The high speed nature of using light to transfer information as opposed to electron packets increases the speed of electronic devices drastically and coupled with the ability to transfer multiple streams of information on the same wire, allows for the reduction of complexity in circuit architecture. However, optical devices such as lenses and fiber optic cables, suffer a major disadvantage when it comes to miniaturization due to the diffraction limit of light,[8] which sets a lower limit on how small a device can be made depending on the wavelength of light being used.

Recently plasmonic structures, which rely on metallic waveguide structures for light transfer, have demonstrated excellent properties for confining light to sub-diffraction limited dimensions[1, 9-12] and transferring light across distances of hundreds of microns depending on the waveguide material and excitation wavelength.[13-16] A plasmon is the collective oscillation of conductive electrons in a metal driven by the oscillating electric field of an incident light wave and is bound to the surface of the material.[17-19] For

extended metallic structures like thin films,[20, 21] stripes,[22] grooves,[23, 24] NWs,[25-28] and chains of particles,[29-32] this plasmon may form a propagating wave along the surface of the waveguide, known as a surface plasmon polariton (SPP), or propagating plasmon. [33-35] For NWs, a photon may couple to the SPP at a break in the geometry of the NW, such as an end tip of the wire,[36, 37] a rough surface[33] or nearby antenna particle[38, 39]. At these breaks, the incident light has the ability to scatter on the surface at multiple angles, which allow momentum matching conditions of the material to be satisfied resulting in successful coupling of light to the SPP.[33] As the plasmon propagates along the NW it generates a near-field intensity along its surface which decays exponentially from its point of excitation due to intrinsic damping losses of the material typically resulting in phonon coupling and heating of the material.[33, 34] The characteristic length of this exponential decay, the length where the intensity decays to 1/e of the original intensity, known as the plasmon propagation length, L_0, is an excellent value for characterization and comparison of metallic waveguides at particular wavelengths. If the propagation length is long enough, then when the plasmon reaches the far end of the waveguide, the intensity of the plasmon may recouple to a photon and scatter from that end,[37, 38] or reflect back into the waveguide where it may create standing waves known as Fabry-Perot resonances.[40 41]

Many experimental techniques have been developed for the measurement of the propagation length such as near-field scanning optical microscopy (NSOM),[18, 35] leakage radiation microscopy,[22, 42] direct imaging,[37, 38] and fluorescence visualization techniques such as direct fluorescence visualization[26, 28, 43] and bleach imaged plasmon propagation (BlIPP).[26, 27, 29, 44] With NSOM the propagating mode is excited by a laser while a small

fiber optic tip is used to probe directly the evanescent field of the propagating plasmon. [41, 45]The measurement is rather expensive due to the need for multiple specialized 3-dimensional piezo motors, and specialized probing tips.

Leakage radiation microscopy has been used for metallic stripes or waveguide structures with strong breaks in the waveguide geometry that exist throughout the waveguide.[20, 46, 47] In the case of stripes the break in geometry exists on the corners of the rectangular cross sections of the stripes.[22] While the plasmon propagates in such structures, at these corners the plasmon may couple to photons and scatter from the edges. By capturing a wide field image with a CCD camera while the waveguide is excited, the radiation intensity leaked from these edges may be used as an indicator for the plasmon intensity. By measuring the intensity profile of the leakage radiation, the plasmon propagation length may be measured. Though an efficient means of measuring the propagation length, the energy lost radiatively from the corners results ultimately in a reduced propagation length.[47]

Direct imaging, which follows similarly to leakage radiation microscopy, is used for structures such as smooth NWs where only a few breaks in the geometry are present, such as end tips and any particles near the NW which serve as antennas.[25, 38, 48] A wide field image taken while the waveguide is being excited is used to determine whether or not light radiates outwards from a far tip or coupling site for a NW of a particular length. In some cases antenna particles are used along the sides of the waveguide in order to approximate a propagation length, though again the propagation length is reduced due to the loss of energy from these coupling sites.[46]

Fluorescence visualization techniques such as direct fluorescence imaging and BlIPP have been developed very recently.[26-29, 43, 44, 48] These methods use far-field measurement techniques like wide-field fluorescence imaging with a CCD camera, or fluorescence confocal microscopy to image the fluorescence response of fluorescent dye films, which probe the near-field intensity of the propagating plasmon. In this work we focus on the development of the BlIPP method and its use for the measurement of the propagation length of Au NWs, chains of Au NPs and bent chains of Ag NPs.

The BlIPP method was developed to determine plasmon propagation by comparing the strength of photobleaching to the exponential decay intensity of the propagating plasmon.[27, 29, 44] A waveguide sample deposited on a glass substrate is coated with a fluorescent dye film. Under high power excitation on an end of a waveguide, the near-field of the launching plasmon interacts with the dye causing it to fluoresce.[43, 44] Over time, at high exposure powers the plasmon intensity begins to photobleach the dye in the film above the waveguide. Using image processing techniques we are able to compare before bleach and after bleach fluorescence images and look directly at the fluorescence intensity that has been photobleached during the exposure period.[26, 27, 29, 44] By taking into account the laser excitation profile and other experimental conditions, the characteristic exponential decay curve of the plasmon intensity may be simulated as we fit the bleach intensity function to the bleach intensity distribution gathered from a line section taken from the photobleach image data over a waveguide. In our first studies with the use of BlIPP we investigated smooth short Au NW waveguides at an excitation wavelength of 532 nm using the conjugated polymer poly[2-methoxy-5-(2-ethylhexyloxy)-1,4-phenylenevinylene] (MEH-PPV) as our dye film.[27]

Smooth single crystalline nanowires are the usual choice for waveguiding studies since their smooth surfaces provide excellent confinement of energy along the surface. [40, 49] However, nanowires are typically made in bulk and stored as free floating nanowires in solution.[26, 27, 50, 51] For plasmonic circuitry to develop it will be necessary in the future to move these nanowires from solution and place them onto a chip in specific designs with full control over long axis orientation and position. Some methods exist for such placement of particles from solution onto a substrate such as the use of micromanipulators[48] or optical trapping.[52, 53] These techniques however, require the placement of a single particle into position at a time. For chips, thousands of transistors would need wire connections which would not be possible if each wire takes up to 20 s or more to trap and write.[52]

Typically e-beam lithography is used to create a pattern, which is then coated with a metal via thermal evaporation followed by a resist lift off procedure though other lithography methods are also popular.[4, 15] This technique has proved well in industry for the creation of small feature circuit boards. Plasmonic metallic stripe structures have been created with this method as well and have shown decent propagation lengths in previous measurements.[15, 22, 54] However, these waveguides suffer from extra radiative leakage losses of energy due to their rough polycrystalline structure and the sharp corners of their rectangular prism shape.[22, 54]

Recently similar lithography techniques have been developed to organize small nanoparticle structures into tight packed large assemblies of nearly any shape and design.[55-57] Here we investigate the waveguiding properties of tightly packed spherical particles in wire formations using BlIPP. Chain structures, made up of closely spaced

small nanoparticles, have been studied previously with chains made with particle gaps of nearly 50 nm, and yielded a propagation length of ~ 289 nm[32] using e-beam lithography for design. In 2011, Willingham et al. demonstrated with the use of Mie theory simulations that when NPs are brought within 3 nm or less of each other in chain structures the interaction between particles may lead to the formation of collective super- and subradiant modes.[30] In charge plots of various wavelength excitation regimes it was determined that these collective modes could align such that one particle's dipole moment would align with the dipole moment of its fellow neighbors leading to a large collective dipole moment for the structure.[30, 57] The large dipole moment favors radiative energy decay paths when excited and for this reason is known as the super-radiant mode. It was also discovered that other modes could lead to a particle's dipole moment aligning in direct opposition to its neighbor's dipole moment leading to a much smaller collective dipole moment for the structure. In comparison to the super-radiant mode, this particular kind of coupling would lead to a suppression of energy losses via radiative decay channels and is known as a dark mode or sub-radiant mode. When a sub-radiant mode is excited the suppression of radiative energy losses results in longer propagation lengths. In this work, we used BlIPP to experimentally verify this hypothesis of long propagation lengths in tightly packed long chain structures.

Because e-beam lithography is used to create the chain pattern, any number of complex designs and structures could be created to further investigate the plasmon propagation of chains. In this work, we explore the possibility of creating bent NP chain structures and use BlIPP to investigate the efficiency of plasmon propagation around sharp corners. The findings of this study demonstrate that by coupling to sub-radiant

propagating modes of chains we are able to propagate energy around bent structures with high efficiency and with insignificant bending losses.

1.2 Specific aims

Photobleaching a fluorescent dye film with the near-field intensity of a propagating plasmon serves as a new and sensitive mechanism for the determination of the plasmon propagation length.[26, 27, 29, 44] The goal of this work is to develop the BlIPP method for measuring the propagation length of plasmonic waveguides and use this technique to investigate plasmonic propagation through sub-radiant plasmon modes in straight and bent NP chains.

Specific aim 1

To develop a measurement method for determining plasmon propagation with the use of fluorescent probes and far-field imaging.

Specific aim 2

To demonstrate the effectiveness of BlIPP on novel metallic waveguide structures, specifically metallic NWs and chains of small metallic NPs.

Specific aim 3

To investigate waveguiding around bent chains of NPs via sub-radiant propagation modes.

1.3 Overview

This thesis contains chapters that are based on publications relevant to the research topic. Chapter 2 presents the first use of BlIPP for the measurement of the

propagation length of short Au NWs.[27] The chapter specifically covers the experimental conditions used for BlIPP measurements and how BlIPP analysis is performed. Theoretical simulations were also performed to support the propagation lengths measured. The work was published in *Nano Letters* in 2010.[27]

In Chapter 3, BlIPP is used to measure the propagation length of Au NP chains. This work uses BlIPP to demonstrate the benefit of coupling light to sub-radiant propagating modes as predicted in previous theoretical work for tightly packed NP chains.[30] For the first time we demonstrate that by propagating energy through dark modes we can transfer energy through chains of particles over distances nearly an order of magnitude longer than previous measurements. The work was published in *Nano Letters* in 2012.[29]

Chapter 4 revisits the photobleaching mechanism of the BlIPP method. We determine experimentally through decay rate measurements that BlIPP uses a 1-photon photobleaching mechanism rather than a 2 photon photobleaching mechanism. We also present in detail the derivation of the BlIPP fitting equation used to determine the propagation length. The work was published in *The Journal of Physical Chemistry B* in 2013.[44]

In Chapter 5, we further explore plasmon propagation along chain waveguides. In particular, we study the efficient propagation of energy around bent Ag chain waveguides using BlIPP. By propagating energy through sub-radiant modes, we demonstrate that by using tightly packed bent structures of NPs we may transfer energy around the waveguide with nearly zero bending losses.

CHAPTER 2

BLEACH IMAGED PLASMON PROPAGATION (BLIPP) IN SINGLE GOLD NANOWIRES[1]

2.1 Abstract

Here, we present a novel approach to visualize propagating SPPs through plasmon-exciton interactions between single gold nanowires (Au NWs) and a thin film of a fluorescent polymer. A plasmon polariton was launched by exciting one end of a single Au NW with a 532 nm laser. The local near-field of the propagating plasmon modes caused bleaching of the polymer emission. The degree of photobleaching along the NW could be correlated with the propagation distance of the SPPs. Using this method of bleach-imaged plasmon propagation (BlIPP), we determined a plasmon propagation distance of 1.8 ± 0.4 μm at 532 nm for chemically grown Au NWs. Our results are supported by finite difference time domain electromagnetic simulations.

2.2 Introduction

One-dimensional metallic nanostructures such as NWs, stripes, or NP chains are widely studied as potential optical waveguides.[22, 25, 31, 32, 36, 37, 40, 58, 59] By coupling electromagnetic waves to collective electron oscillations in the metal known as SPPs,[33, 34] light can be guided over distances exceeding tens of micrometers and then emitted at the opposite end of the plasmonic waveguide.[21] Critically important in the design of metallic

[1] Reprinted (adapted) with permission from "Bleach Imaged Plasmon Propagation (BlIPP) in Single Gold Nanowires" by David Solis Jr., Wei-Shun Chang, Bishnu Khanal, Kui Bao, Peter Nordlander, Eugene Zubarev, and Stephan Link, *Nano Letters* **2010,** 10, (9), 3482-3485. Copyright 2013 American Chemical Society.

waveguide structures is the minimization of radiative and nonradiative losses that cause reduced SPP propagation distances. The high crystallinity and smooth surfaces of chemically prepared Ag NWs have been shown to drastically improve SPP propagation distances compared to lithographically fabricated structures.[25, 40, 58, 59] For this reason, NWs are promising as interconnects in integrated optical and electronic circuits.

Chemically grown Au NWs have in principle the same advantages as Ag NWs, but Au is intrinsically more lossy, especially at optical frequencies.[60] This makes it more difficult to accurately determine SPP propagation distances in Au NWs, especially if the NWs are longer than the SPP decay length. In contrast, for NWs shorter than the SPP propagation distance, excitation at one of the NW ends allows for photons to couple with SPP modes, which are then converted back into light at the opposite NW end as observed by far-field distal end emission.[25, 58, 59] Because the SPPs are also partially reflected at the NW ends creating Fabry−Perot type cavity resonances,[40, 41, 61, 62] the emitted light intensity by itself is however not a sufficient parameter for determining the SPP propagation distance. An alternate approach is to use multiple or variable input couplers positioned at different locations along the NW (e.g., sharp NW kinks, closely spaced NP antennas, or other waveguides)[25, 38, 58] but this requires precise control over the launch sites, which can often be difficult.

A different approach, which does not rely on the conversion of SPPs back into photons and hence is applicable to NWs much longer than the propagation distance, is to directly measure the plasmon-induced near-field. This has been accomplished using, for example, near-field scanning optical microscopy or photoemission electron microscopy.[40, 41, 63, 64] Although these are excellent techniques for mapping the SPP near-field intensity

and propagation distance, lower resolution far-field detection can often be less expensive, easier to implement, and more straightforward to interpret. Taking advantage of energy transfer between the SPP field and fluorescent molecules, it has been shown that the optical near-field of SPPs can be visualized using far-field fluorescence microscopy.[43, 65] However, for short SPP propagation distances the fluorescence intensity due to direct laser excitation masks the much weaker signal originating from SPP excited fluorescence. In addition, a drawback of this method can be the irreversible photobleaching of the fluorescent probe.[43] Hence, it remains an important challenge to accurately measure the SPP decay in metallic NWs to address the needs in the fast growing field of plasmonic waveguiding.

Here, we introduce a far-field method that exploits the photobleaching of a thin film of fluorescent polymer coated on top of Au NWs.[27] We demonstrate that the SPP near-field can be imaged through the bleaching of the polymer emission along the NW, thereby obtaining the SPP propagation distance. Because bleach-imaged plasmon propagation (BlIPP) does not rely on light emission at the distal NW end or input couplers along the NW, it can be applied to any plasmonic NW but is particularly suited to measure highly damped SPPs. In particular, we applied BlIPP to determine the SPP propagation distance in chemically grown Au NWs at 532 nm, where interband absorptions strongly damp the SPPs. In conjunction with simulations, we identified several higher order SPP modes with surprisingly long propagation distances.

2.3 Experimental

2.3.1 Materials and Sample Preparation

First, cetyltrimethylammonium bromide (CTAB) coated 30 nm wide NWs (NWs) were synthesized by tip selective growth of purified pentahedrally twinned Au nanorods[50]. The NWs used in this study were then grown by fast side wise deposition of Au on the pre-synthesized NWs. The lengths and widths were determined by scanning electron microscopy (SEM). The Au NWs were measured to have average dimensions of 6.1 ± 1.2 μm x 400 ± 80 nm from SEM images taken at a magnification of 2,000 (Figure 2.1A) and 11,000 (Figure 2.1B) on a JEOL 6500F SEM operating at a voltage of 15 kV.

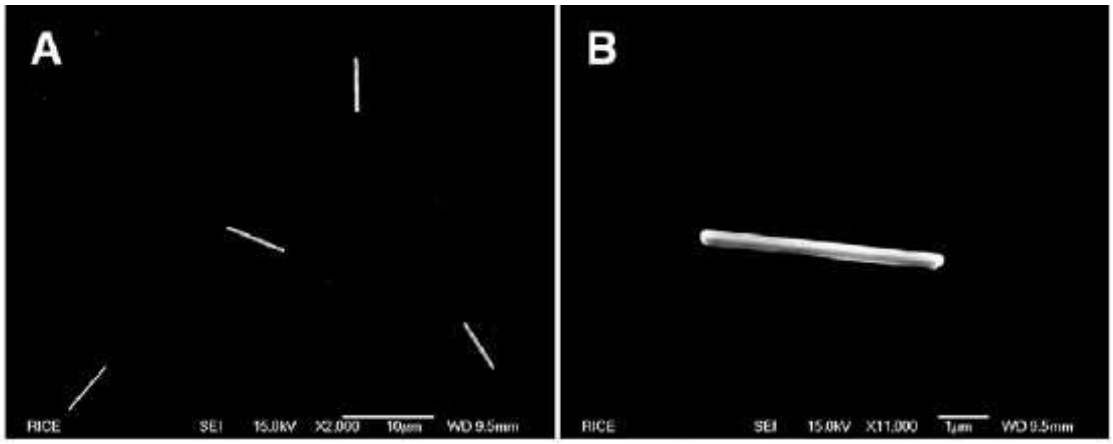

Figure 2.1 (A) shows an SEM image of Au NWs taken at a magnification of 2,000. **(B)** shows an SEM of a single Au NW taken at a magnification of 11,000.

A drop of the Au NW solution was spin cast (Headway Research Inc.) at 2000 rpm for 40 seconds onto a glass coverslip (Fisher Scientific). The coverslips were first sonicated (Branson 2510) for 15 minutes in Acetone (Fisher Scientific) and then oxygen plasma cleaned (Harrick Plasma). The sample was then dipped in warm deionized water and dried with a low nitrogen flow in order to remove excess CTAB. Afterwards a 8.5*10-3 g/mL solution of poly[2-methoxy-5-(2-ethylhexyloxy)-1,4-phenylenevinylene] (MEH-PPV, M_n = 40,000-70,000, Sigma Aldrich) in toluene (Fisher Scientific) was spin

cast onto the Au NWs at 3000 rpm for 40 seconds which created a continuous 60 nm thick MEH-PPV film covering the Au NWs as well as the glass surface. The film thickness of the fluorescent polymer was measured by scratching the polymer film and imaging the scratch using atomic force microscopy (Digital Instrument Nanoscope IIIA).

2.3.2 Experimental Setup

Fluorescence images were acquired using a 532 nm laser excitation source (Coherent Verdi V6), an XY translation piezo stage (Physik Instrumente P-517.2CL), an inverted microscope (Zeiss Observer), a 100x magnification 0.75 NA objective (Zeiss Epiplan), and an avalanche photodiode detector (Perkin Elmer, SPCM-AQRH-15-FC). The laser beam was focused to a diffraction limited spot size (FWHM = 300 nm) at the sample. Circular and linear polarizations were controlled by a quarter and half waveplate (Thorlabs), respectively. To make sure that only fluorescence was detected, a 532 nm notch filter was placed into the detection path and an appropriate dichroic was used in the microscope. Photons collected by the detector were digitized as TTL signals and counted by a counting board (National Instruments DAQ PCI-6602). The photon counting board and scanning stage were controlled by a LabVIEW program. Typically, sample scanned fluorescence images were taken of 10 x 10 μm areas with an integration time of 5 ms/pixel and a resolution of 256 x 256 pixels. Fluorescence spectra in the wavelength range of 400 – 800 nm were acquired by redirecting the fluorescence to a monochromator (Horiba Jobin Yvon TRIAX 190) coupled to a liquid nitrogen cooled CCD camera (Horiba Jobin Yvon Symphony). Note that the MEH-PPV film covered both the NW and

the surrounding area and was facing the excitation light. The laser focus was optimized carefully for each measurement.

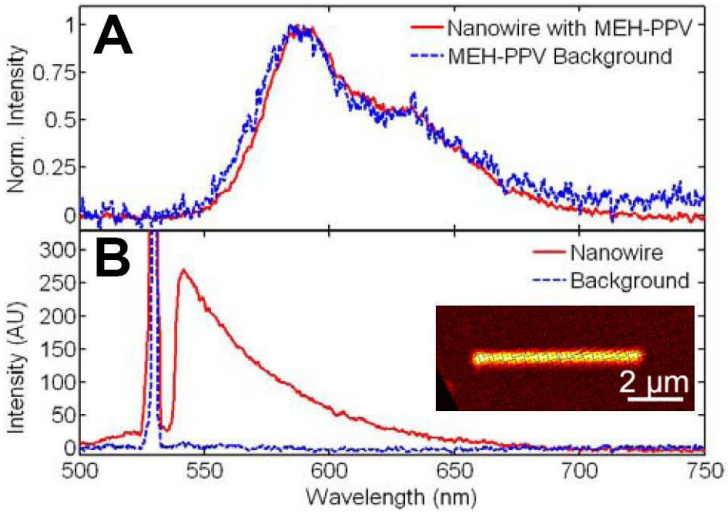

Figure 2.2 (A) shows spectra taken from a MEH-PPV coated Au NW sample on (red solid line) and next to (blue dashed line) a single NW. The excitation power was 34 pW. **(B)** shows spectra taken from a non-coated NW sample on (red solid line) and next to (blue dashed line) a single NW. The inset shows a fluorescence image of a non-coated Au NW. The peak at 532 nm corresponds to the laser excitation wavelength which could not be entirely blocked at a higher laser power of 109 µW.

Fluorescence spectra of a MEH-PPV coated Au NW sample recorded with a 10 seconds exposure time and an excitation power of 34 pW are shown in Figure 2.2A. The fluorescence spectrum taken from an area on top of a Au NW is indistinguishable from the MEH-PPV fluorescence collected next to the NW. This shows that only the intensity was enhanced while the spectrum of the conductive polymer did not change.

To ensure that intrinsic luminescence from the NW did not contribute to the observed intensity, we measured the fluorescence image of the Au NW before coating it with the MEH-PPV film. At the same excitation power as used for the NW – MEH-PPV sample we did not observe any luminescence from the Au NW. Only after increasing the laser power by more than a million was the intrinsic luminescence from the NW

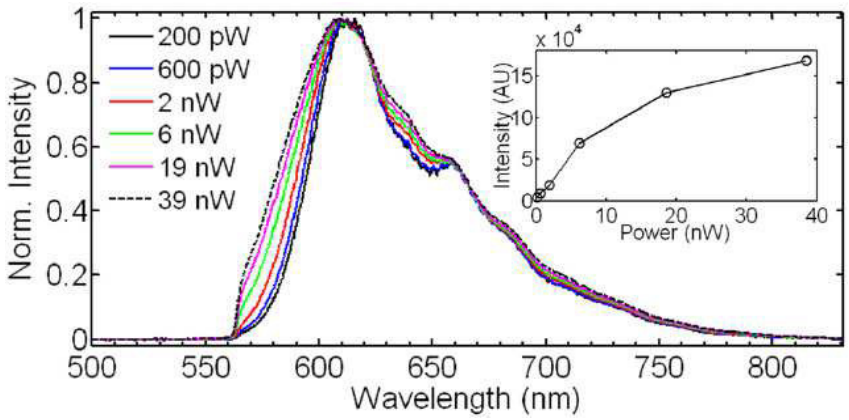

Figure 2.3 Fluorescence spectra taken from a MEH-PPV coated Au NW as a function of excitation power. The inset shows a plot of the fluorescence intensity at the maximum wavelength vs. laser power

detectable. Figure 2.2B shows the luminescence spectrum of a Au NW using an excitation power of 109 mW. A fluorescence image of a non-coated Au NW is shown in the inset. The background spectrum in Figure 2.2B was collected with the laser positioned next to the NW. All spectra were corrected by subtracting detector dark counts.

We also performed a power dependence measurement for the MEH-PPV fluorescence collected from an area above a Au NW. The normalized spectra are shown in Figure 2.3 and the inset is a plot of the fluorescence intensity at the maximum wavelength (610 nm) vs. laser power. The spectra slightly broaden with increasing excitation power as also observed for spectra of MEH-PPV without Au NWs present. More importantly, no spectral narrowing indicative of stimulated emission was observed as otherwise expected for gain due to plasmon-exciton interactions. The intensity furthermore follows initially a linear power dependence and then saturates at higher excitation powers, probably due to photobleaching (see inset).

The fluorescence enhancement of the MEH-PPV film was found to be independent on the laser polarization. Figure 2.4 illustrates that fluorescence images of a MEH-PPV coated Au NW showed no difference in the measured intensity when light

polarized parallel (Figure 2.4A) or perpendicular (Figure 2.4B) to the long NW axis was used. The excitation power was carefully adjusted to the same value of 30 pW for both laser polarizations.

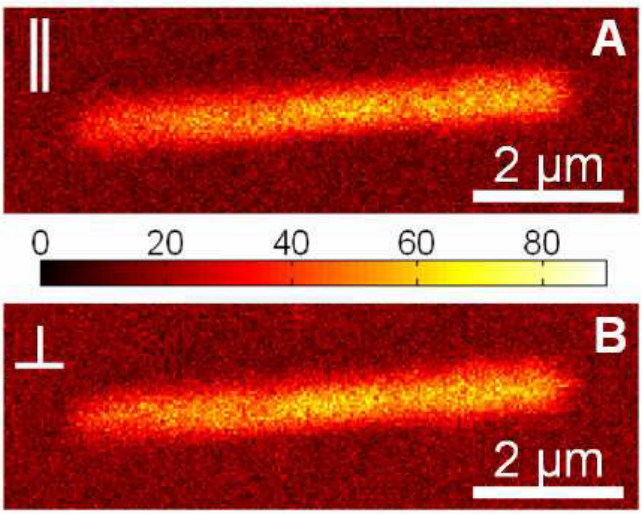

Figure 2.4 (A) shows a sample scanned fluorescence image of a MEH-PPV coated NW. The excitation source was polarized parallel to the long axis of the NW. **(B)** shows a sample scanned fluorescence image of the same NW as in Figure 2.4A except that in this image the excitation source was polarized perpendicular to the long axis of the NW. The laser power for both images was 30 pW.

2.3.3 Description of BlIPP Method

For the BlIPP experiments, a fluorescence image was first taken of a single MEH-PPV coated Au NW using a low excitation power of a few picowatts, shown in Figure 2.5A. The excitation power was adjusted with neutral density filters so that the fluorescence collected from on top of a NW was around 50 counts per 10 ms integration time. The exact power therefore varied slightly from NW to NW, probably due to a small variation in the thickness of the MEH-PPV film. The piezo scanning stage was then positioned such that the laser was focused onto one end of the Au NW and the laser power was raised by a factor of 10,000 (OD filter of 4) for a certain exposure time.

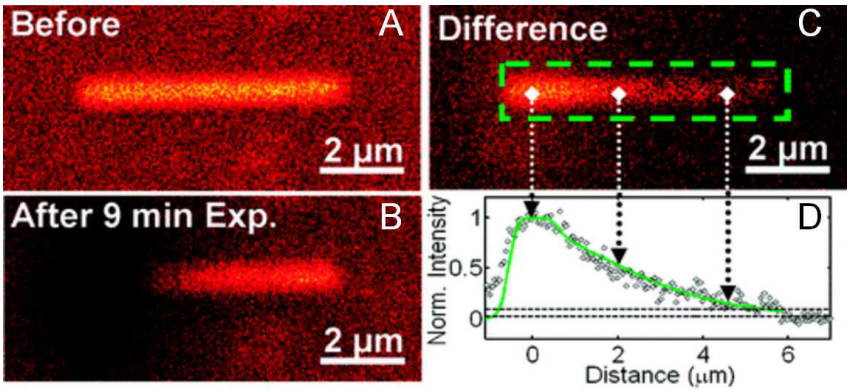

Figure 2.5 (A) Shows a fluorescence image taken over an area with Au NW present as shown by the area with enhanced fluorescence signal. **(B)** Shows the fluorescence image of the same area taken after a 9 min high power laser exposure. **(C)** Shows the difference image created by subtracting (B) from (C). The green highlighted area is then made into a width averaged line section as shown in (D). **(D)** Also shows a green line which is a fit of the data using the derived bleach intensity function, Equation 2.5.

During laser exposure at the Au NW tip, photons met the momentum matching criterion due to the sharp break in symmetry at the NW tip and successfully launched SPPs. Because of the MEH-PPV coating, the propagating SPP waves along the Au NW interacted with excitons of the MEH-PPV causing the MEH-PPV near the Au NW to fluoresce. At high excitation powers and long exposure times the MEH-PPV photobleached due to both direct laser excitation at the focal point near the NW tip and along the Au NW due to plasmon-exciton coupling.

To probe the MEH-PPV photobleaching, the laser power was lowered again to the previous level and a second fluorescence image was taken of the same area, Figure 2.5B. Therefore a destructive technique, namely photobleaching, was used to image plasmon propagation along the Au NW. Note that the laser power and exposure time per pixel were so low for the acquisition of the fluorescence images that photobleaching can safely be neglected. It also needs to be mentioned that during the continuous laser exposure we ensured that the laser remained in focus and sample drift was minimal. For each fluorescence image, the microscope focus was furthermore carefully optimized.

To create images of photobleach intensity the second image taken after the laser exposure was subtracted from the initial image using a program written in MATLAB (version R2007b). This created a difference image shown in Figure 2.5C, which visualized the effect of SPP assisted photobleaching of the MEH-PPV thin film coating. The difference image was analyzed to determine the SPP propagation distance as outlined in the next section.

However, before subtracting the two fluorescence images obtained before and after photobleaching, a background correction factor was determined to correct for small fluctuations in background intensity either due to a slightly different focus or small change in laser power. The background correction factor was calculated by choosing a small background area of 40 x 40 pixels from the same areas in both fluorescence images. All pixels in these areas were first averaged and then their ratio determined, thus yielding the correction factor.

Next, in order to create a width averaged photobleach intensity line section along the long NW axis from the difference image, the width of the NW in the image was first determined by taking an intensity line section perpendicular to the NW. A Gaussian curve was then fitted to this line section using the curve fitting tool in MATLAB. The number of pixels contained within the full width at half maximum of the Gaussian curve was chosen as the NW width. This width and a user defined distance along the NW were used to create an area of interest for the NW in the difference image. Pixels within this area were then averaged in the direction perpendicular to the NW, thereby creating a width averaged line section which covered a user defined distance along the NW in units of pixels, as shown in Figure 2.5D. The physical distance in micrometer was obtained from

the known dimensions of a pixel for a typical scan area of 10 x 10 μm and pixel resolution of 256 x 256 pixels.

2.3.4 Data Analysis Routine BlIPP

The SPP propagation distance was determined by fitting the width averaged line sections to the following model, which considered the MEH-PPV photobleaching as a first order decay reaction due to two components: direct laser excitation at one end of the Au NW modeled by a Gaussian intensity profile and indirect excitation through plasmon-exciton coupling between the MEH-PPV and the exponentially decaying SPP near-field along the Au NW. The MEH-PPV concentration as a function of time t is given by:

$$\frac{[MEH-PPV]_t}{[MEH-PPV]_0} = \exp\left(-kI_G(x)t - kI_{SPP}(x)t\right) \qquad \textbf{Equation 2.1}$$

Here $[MEH\text{-}PPV]_0$ and $[MEH\text{-}PPV]_t$ are the initial concentration of MEH-PPV and the concentration at time, t. kI_{SPP}, and kI_G are the products of the photobleaching rate constant k of MEH-PPV and the incident intensities due to the SPP near-field and the Gaussian laser excitation, respectively. The intensities for both processes are given by spatially varying functions assuming an exponential decay of the SPP intensity along the NW and a Gaussian profile for the laser beam according to:

$$I_{SPP}(x) = I_{SPP,0}\exp\left(-x/x_0\right) \qquad \textbf{Equation 2.2}$$

$$I_G(x) = I_{G,0}\exp\left(-x^2/\sigma^2\right) \qquad \textbf{Equation 2.3}$$

x_0 is the inverse propagation distance of the SPP and σ the width of the Gaussian laser beam. By inserting Equations 2.2 and 2.3 into Equation 2.1, the following expression for the time varying concentration of fluorescent MEH-PPV species is obtained:

$$\frac{[MEH-PPV]_t}{[MEH-PPV]_0} = \exp\left(-kI_{G,0}t\exp\left(-x^2/\sigma^2\right)-kI_{SPP,0}t\exp\left(-x/x_0\right)\right) \qquad \textbf{Equation 2.4}$$

The bleach intensity as a function of x and t as measured in the BlIPP experiments is then given by:

$$I_{bleaching}(x,t) = 1-\exp\left(-kI_{G,0}t\exp\left(-x^2/\sigma^2\right)-kI_{SPP,0}t\exp\left(-x/x_0\right)\right) \qquad \textbf{Equation 2.5}$$

The fits in Figures 2.5 and 2.6 (shown in the next section) were created by fitting Equation 2.5 and adjusting the variables x_0, $kI_{SPP,0}$, and $kI_{G,0}$ to obtain the best agreement with the experimental data. This model well describes the experimental photobleach intensity profiles and accounts for the contributions from both the direct laser excitation and the SPP near-field. In particular, the increasing offset for BlIPP experiments as a function of exposure time, t for the same Au NW is well explained by this model yielding the same propagation distance for each image. We also verified that $kI_{SPP,0}$ does not depend on the radial distance from the NW in the x,y sample plane by comparing the results between width averaged line sections with photobleach intensity profiles that were taken along the center of the NW and not averaged over the NW width.

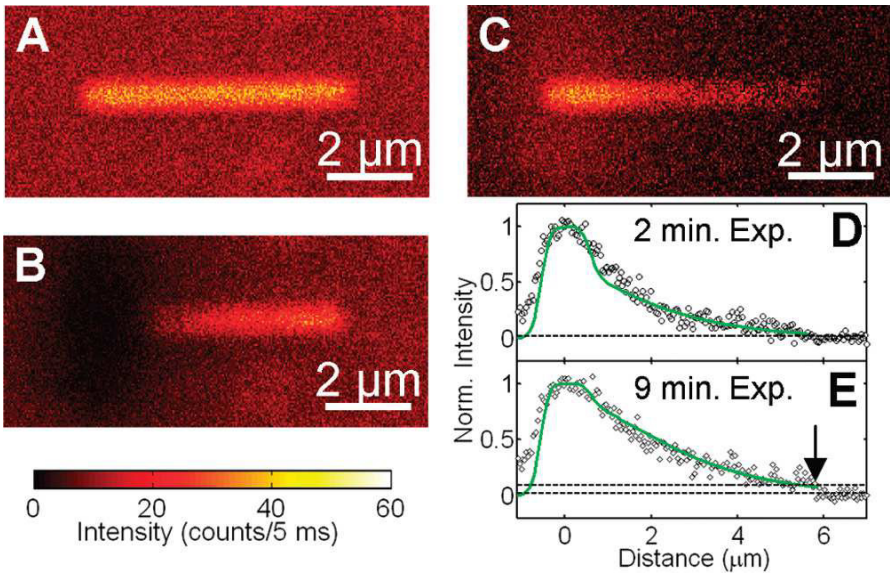

Figure 2.6 Confocal fluorescence images recorded with 4 pWof 532 nm laser light for a MEH-PPV coated 6 µm long Au NW before **(A)** and after **(B)** continuous excitation of the left NW end for 9 min with a power of 40 nW. **(C)** Difference image generated by subtracting (B) from (A). **(D)** Width averaged intensity line section (points) taken along the long NW axis from a difference image taken after a 2 min exposure. The green line is a fit to the data yielding a SPP propagation distance of 1.7 µm.. **(E)** Width averaged line section (points) and fit (green line) obtained from the difference image shown in (C) for a 9 min exposure time. The arrow marks the end of the NW where after the longer exposure time an offset in the photobleached intensity became visible due to continued SPP aided photobleaching. The recovered SPP propagation distance remained unchanged consistent with the described photobleaching mechanism.

2.4 Results and discussion

2.4.1 BlIPP on NWs

Figure 2.6A shows a confocal fluorescence image of a Au NW that has been coated with a 60 nm thick film of MEH-PPV. Excitation was carried out with a circularly polarized 532 nm laser coupled into an inverted single-molecule microscope equipped with a scanning stage and an avalanche photodiode. The Au NWs used in this study had an average length and thickness of 6.1 µm and 400 nm, respectively. At a wavelength of 532 nm these NWs were too long to cause observable distal end emission due to SPP propagation. The Au NW in Figure 2.6A is visible because the fluorescence of the MEH-PPV is enhanced by the plasmonic near-field compared to the background.[66-69] Fluorescence enhancement near plasmonic NPs depends strongly on the distance to the

metal surface as at very close separations the fluorescence is instead quenched.[66, 70] Although the distance between the MEH-PPV film and the Au NW was not controlled, direct contact between MEH-PPV and the Au was avoided by the presence of the CTAB coating of the chemically prepared NWs. We calculated a fluorescence enhancement factor of 3 by taking the ratio of the background signal and the intensity at the center of the NW.

To investigate SPP propagation for the Au NW in Figure 2.6, we first positioned the sample such that the laser was focused at the left NW end. After raising the laser power to 40 nW, the NW was exposed to continuous excitation with 532 nm light for 9 min, which was followed by acquiring a second fluorescence image at the initial power of 4 pW. As shown in Figure 2.6B, the fluorescence intensity of the MEH-PPV film decreased to about zero in a circular area around the left NW end, which can be assigned to photobleaching of the MEH-PPV due to direct photoexcitation by the 532 nm laser.

However, a closer inspection of the fluorescence image in Figure 2.6B furthermore reveals that the MEH-PPV film was also photobleached along the NW, but in no other directions from the laser spot. To better visualize this effect, image Figure 2.6B was subtracted from panel A, creating a difference image given in Figure 2.6C, where a higher intensity corresponds to a larger degree of MEH-PPV photobleaching.

The SPP near-field can be related to the photobleach intensity in Figure 2.6C. While the laser was focused on the NW end, SPPs were excited and propagated along the NW. The SPPs interacted with the MEH-PPV through plasmon-exciton coupling.[71-73] The excitations in the MEH-PPV film then decay radiatively by fluorescence or through nonradiative channels, which include a small but significant yield of irreversible

photochemical reactions permanently turning off the MEH-PPV fluorescence (photobleaching). The concentration of photobleached polymers as measured by the photobleach intensity is directly related to the rate of photobleaching and the spatial distribution of the incident excitation intensity, which is governed by the laser power, strength of the plasmonic near-field, and the exposure time.

The effect of the exposure time is illustrated in Figure 2.6D,E, which shows the width averaged line sections along the major NW axis taken from the difference images after exposure times of 2 (Figure 2.6D) and 9 (Figure 2.6E) min. The photobleach intensity profiles consisted of contributions from the direct laser excitation at the left NW end and the indirect excitation of the MEH-PPV film through plasmon-exciton interactions. Direct photobleaching by the laser was more efficient as can be seen from the complete bleaching of the MEH-PPV within the laser spot even for the shortest exposure time. In contrast, because of the much weaker indirect excitation of the MEH-PPV by the plasmonic near-field, the degree of bleaching increased with time. As indicated by the arrow in Figure 2.6E, this can be seen by the offset in the photobleach intensity at the right NW end. A higher laser power had the same effect as a longer exposure time as the laser power determined the initial amplitude of the SPP modes (data not shown).

Assuming that the rate of MEH-PPV photobleaching as a function of incident intensity follows a first order decay process, the measured photobleach intensity along the NWs can be quantitatively described by considering the contributions from direct laser excitation and the SPP near-field. The laser intensity was modeled by a Gaussian profile and the damping of the SPPs along the NWs by an exponential function.[33] The fit

using Equation 2.5 then yielded the same SPP propagation distance of 1.7 μm for the 2 and 9 min exposure times. The independence of the SSP propagation distance on the exposure time and the drop in photobleach intensity at the right NW end are furthermore consistent with the described plasmon-exciton mediated photobleaching mechanism.

To characterize the nature of the SPP modes in these Au NWs, we performed BlIPP experiments with excitation polarized parallel and perpendicular to the main NW axis as shown in Figure 2.7A,B, respectively. The insets show the difference images for two NWs with similar lengths and the same exposure time of 8 min and laser power of 90 nW. The fluorescence enhancement was found to be independent of laser polarization (Figure 2.4) and no further corrections were necessary. The fits to the experimental data in Figure 7A,B give SPP propagation distances of 2.1 and 1.7 μm, respectively. The mean SPP propagation distances as obtained from a total of 20 NWs were 1.9 ± 0.4 and 1.7 ± 0.2 μm for parallel and perpendicular excitation, suggesting that the SPP propagation distance is only weakly dependent on the excitation polarization. However, a direct comparison of the fits shown in Figure 2.6C reveals that the amplitude of the SPP near-field is larger for excitation with parallel polarized light because of the larger offset in the photobleach intensity. These measurements demonstrate that although both longitudinal and transverse polarized SPPs were excited, parallel excitation was more efficient.

The histogram in Figure 2.7D summarizes the SPP propagation distances obtained for 27 independent BlIPP measurements on Au NWs. The average propagation distance was 1.8 ± 0.4 μm. The width of the distribution can be attributed to several factors including the variation in NW diameters and tip shape as well as differences in surface

roughness which influence the confinement and damping of the SPP modes.[33, 59] In addition, the MEH-PPV film thickness and homogeneity including locally varying polymer chain conformations could cause changes in the MEH-PPV photobleaching rate and hence affect the fitted SPP propagation distances.

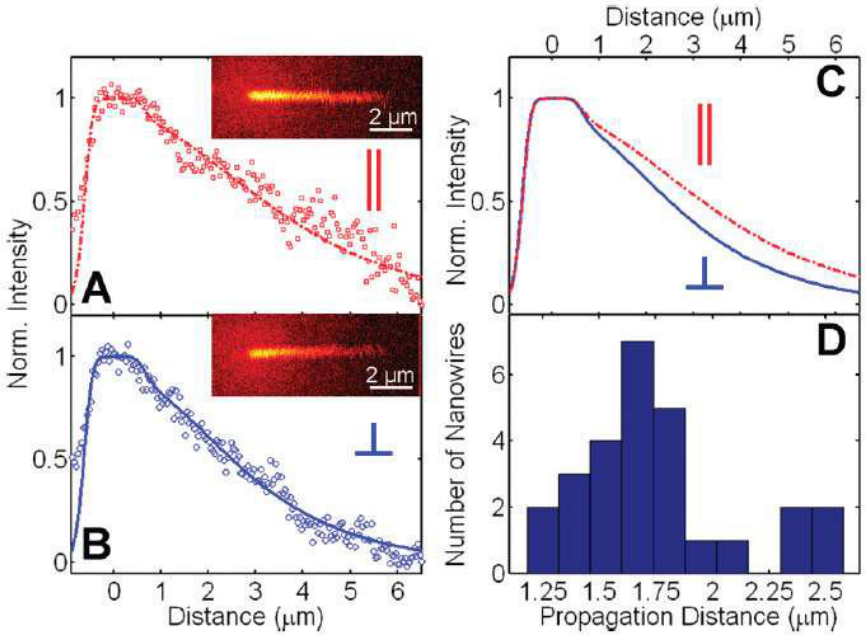

Figure 2.7 Width-averaged intensity line sections and fits obtained from the difference images shown in the insets for excitation polarization parallel **(A)** and perpendicular **(B)** to the long NW axis. The difference images were obtained after 8 min exposure to an excitation power of 90 nW. For the fluorescence imaging a laser power of 9 pW was used. **(C)** Comparison of the fits to the plasmon bleach intensity for the two NWs shown in (A) and (B). The larger offset for parallel polarized excitation (red) indicates a larger SPP amplitude for this polarization. **(D)** Histogram of SPP propagation distances measured by BlIPP for 27 individual Au NWs.

2.4.2 Finite Difference Time Domain (FDTD) Simulations

To further verify our experimental results we performed finite difference time domain (FDTD) simulations, the results of which are shown in Figure 2.7. A Gaussian excitation beam with parallel (Figure 2.8A) and perpendicular (Figure 2.8B) polarization coupled to several SPP modes at the left NW tip. The initial decay of the electric field intensity was due to a superposition of mostly localized and higher order multipolar SPs. At 1 μm from the NW tip, the dominant SPP with a propagation distance of 1.1 μm was the m = 2 mode as identified by cross sectional views of the surface charge distribution. In agreement with experiment, this quadrupole SPP mode could be excited with parallel and perpendicular polarization, slightly favoring parallel excitation as seen by the larger amplitude. A weaker m = 1 SPP mode with an even longer propagation distance of 4 μm

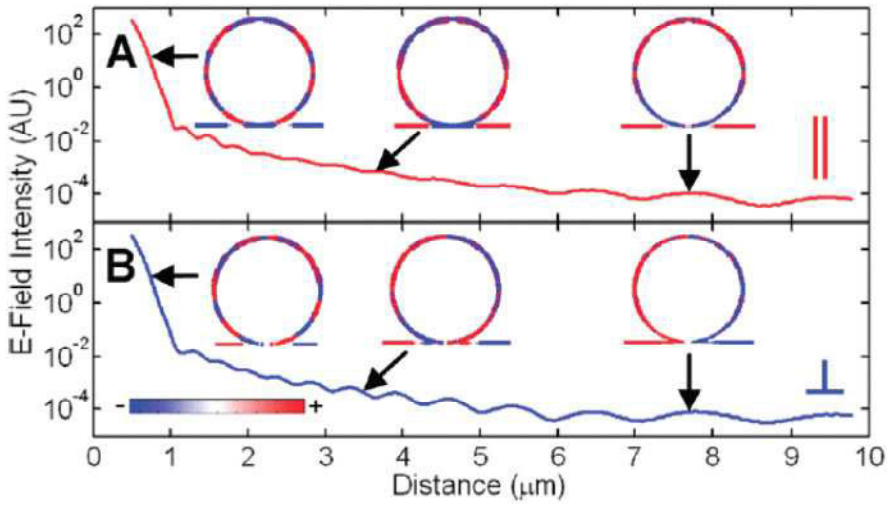

Figure 2.8 FDTD simulations for a 400 nm thick Au NW with a 532 nm Gaussian laser beam (fwhm = 330 nm) having parallel **(A)** and perpendicular **(B)** polarization incident on the left NW end. Several SPP modes were excited and identified based on their surface charge distributions. Cross sectional views of the surface charges are shown as insets, where the scale from red to blue represents changes from positive to negative. The fast decay of the electric field intensity at the NW tip can be assigned to a mixture of mostly localized plasmon modes. Further along the NW the dominant SPP is the m = 2 mode followed by a less intense and slower decaying m = 1 SPP.

was also supported by this NW. The length of the simulated NW was chosen to be 10 μm in Figure 2.8 to clearly identify the m = 1 mode.

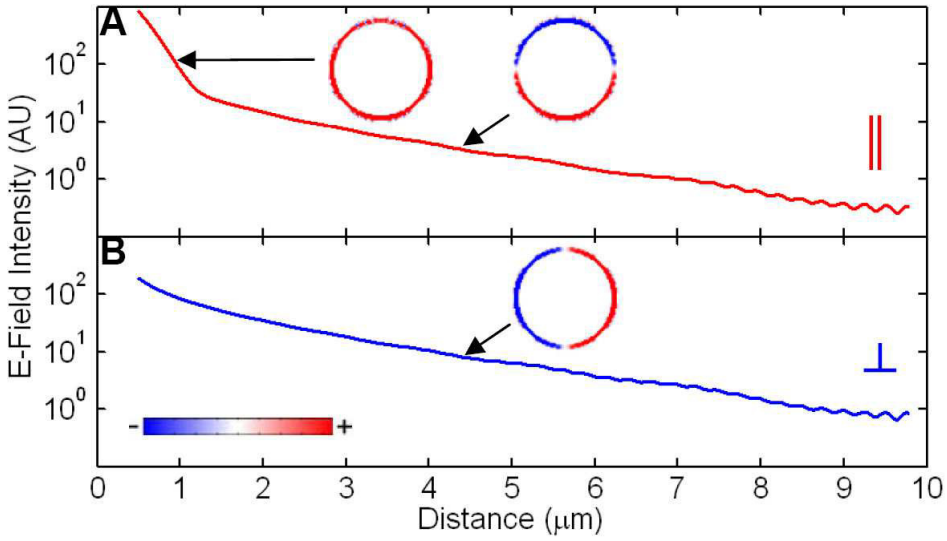

Figure 2.9 FDTD simulations for a 120 nm thick Au NW with a 532 nm plane wave having parallel **(A)** and perpendicular **(B)** polarization incident on the left NW end. The length of the NW was 10 μm. Cross sectional views of the surface charges for the NW in a vacuum medium are shown as insets, where the scale from red to blue represents changes from positive to negative. The main decay of the electric field intensity for parallel and perpendicular excitation can be assigned to the m =1 SPP with a propagation distance of 2.0 mm for both polarizations. The fast decay for parallel polarization corresponds to the m = 0 SPP mode, which is localized at the NW tip. Fitting a decay constant for the m = 0 mode is difficult because of the overlap with localized plasmons excited by the plane wave.

While the m = 2 SPP is the dominant mode, the m = 1 mode also contributed to the measured averaged propagation distance of 1.8 μm. In particular, the relative amplitudes of these two modes depend critically on the NW diameter as well as the shape of the NW tip.[59] The latter strongly determines the coupling efficiency of the laser light to different SPP modes. FDTD simulations for different Au NW diameters, the smallest of which 120 nm diameter is shown in Figure 2.9, furthermore show that the m = 1 SPP mode starts to dominate for thinner NWs as the m = 2 mode could no longer be supported. Interestingly, the fundamental m = 0 mode was always strongly localized at the NW tip with a large damping yielding sub-micrometer propagation distances independent of NW diameter.

Because the FDTD simulations treated the MEH-PPV film as a simple dielectric, the interactions between NW plasmons and MEH-PPV excitons were entirely neglected. Hence, possible gain due to conversion of excitons back into plasmons along the NW effectively increasing the SPP propagation distance were not taken into account and could also explain the longer SPP propagation distance in the BlIPP studies. However, the good agreement between the FDTD calculations and the experimental and modeled photobleach intensity line sections for all NWs including time dependent BlIPP measurements on the same NWs suggests that gain, if at all, was only a minor contributor to the measured SPP propagation distance. A laser power dependence on the fluorescence spectra also showed no spectral narrowing indicative of stimulated emission and gain.[74]

2.5 Conclusions

In summary, we report a new method, BlIPP, by which it is possible to visualize SPP propagation in the far-field via plasmon-exciton coupling mediated photobleaching of an organic chromophore coated on top of a plasmonic waveguide. BlIPP creates a permanent record of the spatial intensity profile of the SPP near-field, particularly suited to read out short SPP propagation distances without the interference by a much stronger signal from the excitation source. We applied BlIPP to visualize SPPs in chemically prepared highly crystalline 6.1 μm × 400 nm Au NWs. Even for a wavelength of 532 nm, where interband absorption losses are significant in Au, we found a propagation distance of 1.8 ± 0.4 μm. These results are in very good agreement with FDTD simulations and the analysis of the surface charge distribution revealed that the main SPP is a quadrupole mode that can only be supported by these thicker NWs. We expect that the simplicity of

the BlIPP method, and its utility in investigating even strongly damped SPPs, will make it a useful tool to determine SPP propagation distances in a wide range of plasmonic materials.

2.6 Acknowledgement

Support was provided by the Robert A. Welch Foundation (C-1664 to S.L., C-1703 to E.R.Z., C-1222 to P.N.), 3M (S.L.), NSF (CHE-0955286 to S.L., DMR-0547399 and CBET-0506832 to E.R.Z.), TATRC (W8XWH-07-2-0101 to E.R.Z.), Alfred P. Sloan Foundation (E.R.Z.), and the Center for Advanced Solar Photophysics, an EFRC funded by DoE (P.N.). D.S. was supported by an NSF Graduate Research Fellowship and W.S.C. by a Peter and Ruth Nicholas Fellowship from the Smalley Institute. We thank the reviewer for invaluable feedback, Dr. Matthew Pelton, Dr. Christy Landes, and the Landes group for useful discussions, and Britain Willingham for help with the data analysis.

CHAPTER 3

ELECTROMAGNETIC ENERGY TRANSPORT IN NANOPARTICLE CHAINS VIA DARK PLASMON MODES[2]

3.1 Abstract

Using light to exchange information offers large bandwidths and high speeds, but the miniaturization of optical components is limited by diffraction. Converting light into electron waves in metals allows one to overcome this problem. However, metals are lossy at optical frequencies and large-area fabrication of nanometer-sized structures by conventional top-down methods can be cost-prohibitive. We show electromagnetic energy transport with Au NPs that were assembled into close-packed linear chains. The small inter-particle distances enabled strong electromagnetic coupling causing the formation of low-loss sub-radiant plasmons, which facilitated energy propagation over many micrometers. Electrodynamic calculations confirmed the dark nature of the propagating mode and showed that disorder in the NP arrangement enhances energy transport, demonstrating the viability of using bottom-up NP assemblies for ultra-compact opto-electronic devices.

3.2 Introduction

Minimizing losses is a critical goal in energy and information transport applications that range from electricity transmission to fiber optic communication[2, 75-77].

[2] Reprinted (adapted) with permission from "Electromagnetic Energy Transport in Nanoparicle Chains via Dark Plasmon Modes" by David Solis Jr., Britain Willingham, Scott Nauert, Liane Slaughter, Jana Olson, Pattanawit Swanglap, Wei-Shun Chang and Stephan Link, *Nano Letters* **2012**, 12, (3), 1349-1353. Copyright 2013 American Chemical Society.

At the same time, a continuing demand for improved technology requires the creation of increasingly smaller transport structures[1]. When using light as the transport vehicle, this goal is hampered by the optical diffraction limit, which puts a large lower boundary on the widths of optical communication fibers[77]. This problem can be overcome by exciting coherent electron waves in metals[9, 12, 23, 78, 79], known as SPs. However, metals are lossy at optical frequencies[2, 75, 76, 80, 81], and large-area fabrication of nanometer-sized structures by conventional top-down methods can be expensive.

Several different waveguide geometries have been explored to guide SPs in sub-wavelength dimensions[9, 32, 82-84]. NP chains are an attractive, complementary structure to straight NWs. Complex chain geometries within which light can be transported around corners, including sharp 90˚ turns[31, 85], could offer flexible interconnects between more rigid waveguides. In groundbreaking work,[32] Maier *et al.* demonstrated experimentally that electromagnetic energy transport is indeed possible in chains of lithographically prepared Ag nanorods with large inter-rod gaps (50 nm), but the relatively short propagation distance (~500 nm) proved discouraging to further exploration of NP chain waveguides. A particularly interesting alternative to structures fabricated by a serial top-down process is parallel bottom-up assembly of metal NPs into chains[55, 86-91]. This approach has the advantage of enabling cost-effective fabrication of arbitrary NP chain geometries - straight, bent, branched, and so forth, over large areas[55, 88]. In addition, chemically synthesized nanostructures are single crystalline, thereby minimizing losses due to scattering of electrons at grain boundaries[40, 49]. Finally, this synthesis method allows much smaller inter-particle spacings (~ 1-5 nm) that result in stronger plasmon

coupling[86, 87, 89, 91-93], which is one prerequisite for increasing propagation distances in these materials.

Here we show that we can increase the propagation distance in assembled chains of closely-spaced Au NPs by at least an order of magnitude compared to previous studies[32]. This is made possible by exploiting enhanced inter-particle coupling and the resulting dark plasmon modes that support low-loss energy propagation[30, 94-98]. Using a novel imaging method, BlIPP[27], we determined a plasmon propagation distance of L_0 = 3.9 ± 0.6 μm for these Au NP chains when exciting the dark modes, in contrast to no measurable propagation when exciting the bright single NP mode. This propagation distance is long enough to be comparable to other promising waveguide structures such as Au NWs[20, 28]. Electrodynamic calculations furthermore showed that plasmon propagation is supported over a large bandwidth and that disorder in the NP arrangement actually enhances energy transport.

3.3 Experimental

3.3.1 Materials

Spherical Au NPs (NPs) were purchased from Nanopartz. Indium tin oxide (ITO) glass used as the substrate had a resistance of 8-12 ohms, was 0.7 mm thick and was obtained from Delta Technologies. A solution of 4% 495 kg/mol poly(methyl methacrylate) (PMMA) in anisole was ordered from MicroChem and used as the photoresist. The developer, 1:3 MIBK (methyl isobutyl ketone) in isopropanol was purchased from Sigma-Aldrich. Rhodamine 6G chloride (R6G) dye (R634) purchased from Invitrogen and Cardiogreen dye (I2633) purchased from Sigma-Aldrich were used

for the 514 and 785 nm excitation experiments, respectively. Methanol and acetone were also purchased from Sigma-Aldrich.

3.3.2 Fabrication of Nanoparticle Chains

Preparation of the chain array sample started by cleaning ITO glass using the RCA-1 procedure beginning with a mixture of 1:4:20 ammonium hydroxide, hydrogen peroxide, and water heated to 60° C. The ITO glass was then plasma cleaned (Harrick Plasma). After the ITO glass was cleaned it was coated with a thin film of PMMA in anisol. Electron beam lithography (JEOL 6500) was used to cut rectangular trenches of size 15 μm x 300 nm into the photoresist. The trenches were developed in MIBK solution for 25 seconds followed by a stop bath of isopropanol. Fully developed trenches were verified by dark-field microscopy using an inverted microscope (Zeiss Axiovert 200) and a 50x Zeiss air-spaced objective with a numerical aperture (NA) of 0.8. The trenches were filled by dropping 5 μL of the NP solution onto the sample. As the solution dried over the trench arrays, the NPs filled in the trenches to form chains of NPs. To create free-standing NP chains as shown in Figure 3.1, the PMMA surrounding the filled trenches was removed by dipping the sample into acetone followed by drying with compressed N_2. In a sense, this assembly method represents a combination of the best of top-down and bottom-up methods in that small inter-particle distances can be achieved because we use chemically-synthesized NPs but the chain itself or any other geometry can be created reproducibly using lithographic preparation methods.

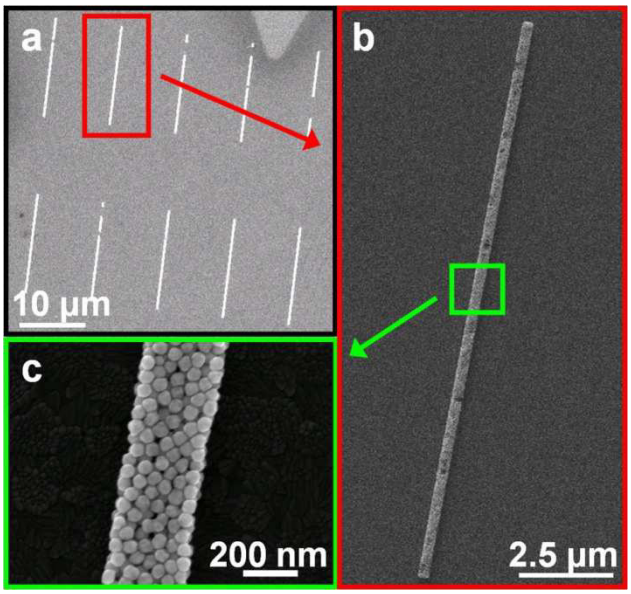

Figure 3.1 SEM characterization of NP chain assemblies. **(a)** SEM image of an array of chains made from 47 ± 4 nm Au NPs. **(b)** SEM image of the NP chain highlighted by the red box in **a**. **(c)** SEM image taken for the green area indicated in **b** to show the close-packed arrangement of the NPs. NPs were assembled in trenches formed in a polymer, which was then removed together with excess NPs not assembled in the designed patterns to yield free-standing NP chains on a glass substrate. Typical chain structures measured 300 nm x 15 µm, were 5 – 6 NPs wide, and approximately 2 – 3 layers high, and contained approximately 1500 particles/layer. Based on the SEM images the average inter-particle distance is estimated to be below 5 nm with the separations likely being smaller considering the limited resolution of the SEM.

Once the NP chain arrays were made, the sample was coated with cardiogreen in a methanol solution with a concentration of 5 mg/mL for 785 nm diode laser (Power Technology Inc.) excitation or R6G in a methanol solution with a concentration of 5 mg/mL for 514 nm Ar^+ laser (Modu-Laser) excitation. For each sample, 60 µL of the dye/methanol solution was spin coated at 6000 rpm for 40 seconds followed by an additional rinse with 5 µL of methanol at 6000 rpm for 40 seconds.

3.3.3 BlIPP Measurement

BlIPP measurement[27] of the dye coated chain sample was performed by first taking a 128 pixel x 128 pixel fluorescence image, *A*, of a 20 µm x 20 µm region of the sample containing a chain assembly at a pixel integration time of 10 ms/pixel. The

fluorescence image was acquired by a sample scanning fluorescence confocal microscope setup (Axiovert 200) with a piezo electric scanning stage (Physik Instrumente) and surface probe controller (RHK Technology) as shown in Figure 3.2a. Circularly polarized laser light was focused through a 50x Zeiss air-spaced objective with a 0.8 NA. Fluorescence light from the laser excited dye molecules was then collected by an avalanche photodiode (APD, Perkin Elmer SPCM-AQR-15). The resolution for 785 nm excitation, shown in Figure 3.2b, was determined by imaging 25 x 86 nm Au nanorods on glass coated with index-matched oil to reduce the background scattering signal. Au nanorods were used for 785 nm excitation because we had no fluorescent dye beads available for this wavelength range. To collect scattering from single Au nanorods, the 785 nm notch filter was replaced with a 4 OD neutral density filter. The image in Figure 3.2b was created by collecting the scattered light with an APD while scanning the sample. The full width at half maximum (FWHM) of the line section for an individual nanorod given in Figure 3.2c is 340 nm. The resolution for 514 nm excitation, shown in Figure 3.2d, was determined by imaging 100 nm fluorescent polystyrene beads. This was achieved in the same way as the BlIPP experiments with 514 nm excitation. The full width at half maximum (FWHM) of the line section for an individual 100 nm bead given Figure 3.2c is 280 nm.

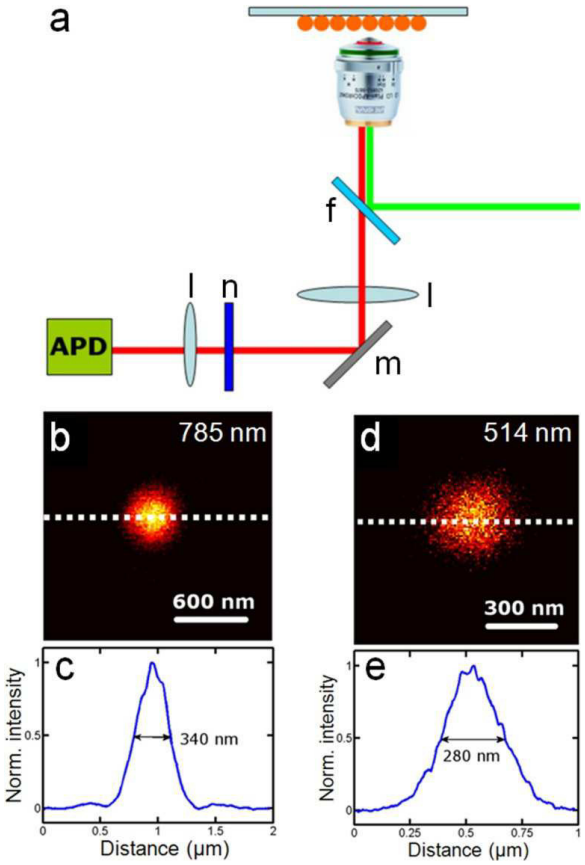

Figure 3.2 Microscope setup and optical resolution. **(a)** The green and red lines represent the excitation and emission paths, respectively. f, is a dichroic filter; l, is a lens; m, is a mirror; n, is a notch filter; APD is an avalanche photodiode detector. The excitation laser (either 514 or 785 nm) was reflected by a dichroic mirror and focused by an objective to excite the dye on the NP chains. The fluorescence of the dye was collected by the same objective and focused on an APD. Scattered laser light was rejected by a notch filter. **(b)** Scattering image of a 25 x 86 nm Au nanorod covered with index-match oil and excited by the 785 nm laser. The scale bar is 600 nm. **(c)** Intensity cross section of the image along the dotted line in **b**. The full width at half maximum (FWHM) is 340 nm. **(d)** Fluorescence image of a 100 nm dye bead excited by the 514 nm laser. The scale bar is 300 nm. **(e)** Intensity cross section of the image along the dotted line in **d**. The FWHM is 280 nm.

After the image was acquired, the stage was positioned so that the laser was focused onto an end of the chain. The laser power was then increased from the low imaging power to a higher exposure power for a given exposure time depending on the sample (imaging power and exposure power are listed in the captions of all BlIPP Figures). During the exposure, light from the laser, whose intensity profile is characterized by a Gaussian curve, launched SPPs along the chain waveguide. The near-field of the propagating plasmons interacted with the dye coating causing the dye to

photo-bleached irreversibly over time. Two intensity profile components are associated with bleaching along the chain: 1) the intensity profile of the Gaussian beam centered about the point of direct laser excitation and 2) the intensity profile of the propagating plasmon near-field which is characterized by an exponential decay function.

After the exposure time period was completed the laser power was adjusted back to the low imaging power. The focus of the microscope was adjusted to insure that the fluorescence intensity collected by the APD was optimal. A second fluorescence image, *B*, of the same region was then acquired.

3.3.4 BlIPP Analysis

The analysis was carried out using Matlab 2010a. To account for small sample and focus drift during the exposure period, before the creation of the difference image, *D*, we performed an image shift correction and background scalar correction. Drift correction of image *B* was accomplished by overlaying image *B* on image *A* to determine the correct shift. A drift corrected image *B'* was then created. Background scalar correction was accomplished by finding the mean value of the same background area from *A* and *B'*, a_{BG} and b'_{BG}. The scalar value of a_{BG}/b'_{BG} was then multiplied to the image matrix of *B'* and image matrix *B''* was created. To highlight the effect of photo-bleaching along the chain that occurred during the high power exposure period, the difference image *D* was created by subtracting image matrix *B''* from image matrix *A*.

Once the difference image *D* was created, we took a width-averaged line section from the area along the chain of interest. This was done by first rotating the image by an angle θ so that the long chain axis in the image lay parallel to the *x* axis using a built-in

Matlab matrix rotation function. The center of the short axis of the chain was then located by finding the peak of a Gaussian curve fitted to a line section taken for the chain along its short axis. The width of the width-averaged line section was 3 pixels centered about the peak of the Gaussian curve along the short axis line section. We established the length of the chain by manually specifying where a chain began and ended from the image. The same area was then taken from image *A* and image *B''* after rotating them by the same angle θ. Width-averaged line sections (WALS) A_{WALS}, B''_{WALS}, and D_{WALS} were then created from the defined regions from *A*, *B''*, and *D*.

To study the photo-bleach intensity as a function of distance *x,* we calculated the normalized line section D_{norm} by normalizing D_{WALS} to A_{WALS} such that $D_{norm}(x)=D_{WALS}(x)/A_{WALS}(x)$. The data from D_{norm} was then analyzed using the following equation:

$$I_{bleaching}(x,t)=1-\exp\left[-kI_{G,0}t\exp\left(-x^2/\sigma^2\right)-kI_{SPP,0}t\exp\left(-x/L_0\right)\right] \qquad \textbf{Equation 3.1}$$

where $I_{bleaching}(x,t)$ is the photo-bleach intensity, t is the exposure time, x is the distance along the chain, σ is the width of the Gaussian laser beam, L_0 is the plasmon propagation distance and $kI_{SPP,0}$ and $kI_{G,0}$ are the products of the photo-bleaching rate constant k of the dye and the maximum incident intensities due to the SP near-field and direct Gaussian laser excitation, respectively. More details about BlIPP can be found in previous work[27].

3.3.5 Numerical Simulations

Numerical simulations were performed with a self constructed version of the partial scattering solution to generalized Mie theory, following the derivation by Gérardy and Ausloos[99]. A parallel implementation facilitated the electrodynamic scattering

solutions of large collections of spherical particles. Electrodynamic fields of up to 1200 50 nm NPs could be fully analyzed at specific wavelengths when using 50 quad-core 2.4 GHz Intel Xeon (Nahalem) CPUs with 8 MB cache. Computer resources were provided by Rice University's research computing support group, specifically the use of the shared-tightly integrated cluster (STIC). Computation times varied depending upon the wavelength of excitation, with normal run times averaging 2 to 3 hours. The particles were assumed to be perfect spheres embedded in a host medium of index of refraction n = 1.5. The material description of each sphere was consistent with the bulk response of Au, with complex dielectric components interpolated from the values tabulated by Johnson and Christy[60].

3.3.6 Generalized Mie Theory

For a single sphere, the electrodynamic solution to Maxwell's equations is the well known Mie-Lorenz theory, in which the scattered and incident fields are represented as a complete expansion of vector spherical harmonics with appropriate weighting coefficients. Subsequent analysis of energy flow provides analytical equations for the optical cross-sections as functions of the scattered field coefficients. By extending this solution to N particles, whereby the incoming scattered fields from neighboring spheres act as further excitations, the scattering coefficients for each of the N spheres is solved by considering a system of linear equations. Analogous to single particle Mie-Lorenz theory for N = 1, analytical solutions for the electrodynamic fields and optical cross-sections can then be formed. Excitation of particle chains is carried out by considering the local approximation to the fundamental TEM_{00} mode of a laser. Here, the integral

representations of the beam expansion coefficients are approximated as an analytical expression[100]. The Gaussian beam, expressed within its local frame, is then translated to particle centers by using the vector spherical wave addition theorem. Incident coefficients are subsequently implemented within the system of linear equations, and the appropriate partial scattering coefficients are solved as in the plane wave case.

Theoretical width-averaged line sections were obtained by averaging the intensity values of the calculated near-field for each 1200 NP chain over a N_x by N_y grid in the x-y plane ($z = 0$). External values of the electromagnetic fields were sampled just outside the structure boundary and throughout the interstitial space between constituent NPs. Values lying in the y-direction, perpendicular to the long-axis of the chain and at the same x-coordinate, were then summed up for each of the N_x columns. Of the N_y positions at each x, only values external to the particle surfaces were accumulated to form the width-averaged line section, allowing each final value along x to be normalized by the total number of collected points at that respective position. Calculations of the width-averaged charge followed the same method, deviating only by accumulating x and y values within the boundaries and along the surface of individual particles.

3.3.7 Particle Array Creation

The psuedo-random particle positions were created using a self constructed, collision-driven molecular dynamics algorithm[101, 102]. The Fortran 90 code creates 2-dimensional packed structures within a lattice formation while considering hard-wall boundary conditions. N point particles are allowed to uniformly grow with time as collision dynamics alters their predicted trajectories. As time evolves, the collisions

become more frequent until eventual particle growth causes the collision rate to diverge, at which time the particles occupy their final resting positions. In this close-packed state, a majority of the particles are touching. All particle sizes are then reduced to their final value of 50 nm in diameter in order to satisfy a minimum surface to surface separation of 1 nm.

3.4 Results and discussion

The increased plasmon coupling for small interparticle distances allows the formation of sub-radiant plasmon modes.[30, 94-98] Sub-radiant plasmons correspond to collective excitations in which the phase for each NP can differ, leading to reduced overall charge separation and reduced coupling to light. The practical advantage in exploiting these dark modes for plasmon propagation is that they have decreased energy losses in comparison to the brightest, super-radiant mode, in which all individual NP plasmons are in phase, or the bright single NP plasmon.

The advantage of dark-mode plasmon propagation, as compared to bright-mode propagation, is illustrated in Figure 3.3. When BlIPP is performed at 785 nm, where dark modes are present, energy propagation persists over several micrometers for the Au NP chain (Figures 3.3a-d and Figure 3.4 for the corresponding SEM image). In contrast, no measurable energy propagation was observed when the chains were excited at the bright single NP mode at 514 nm (Figures 3.3e-h). Figures 3.5 and 3.6 show the scattering and extinction spectra of single 50 nm Au NPs and the chain assembly, respectively, and demonstrate several important points. First, these measurements confirm that exciting at 514 nm coincides with the single Au NP plasmon mode.

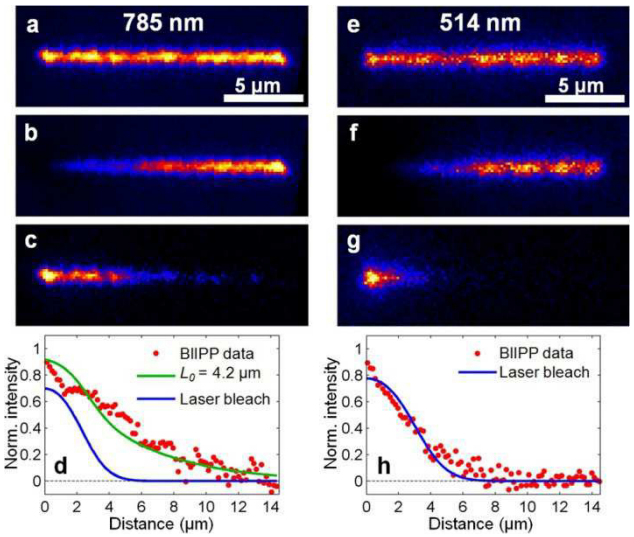

Figure 3.3 BlIPP of a NP chain for 785 and 514 nm circularly polarized excitation. **(a)** Fluorescence image of a chain coated with the dye cardiogreen and excited at 785 nm with a laser power of 66 nW. **(b)** Fluorescence image taken after exposure of the left end of the chain to 7.2 µW of 785 nm laser light for 20 minutes. Photo-bleaching due to plasmon propagation is most apparent in the difference image, **(c)** and the normalized intensity line section (red) along the NP chain, **(d)** Fitting the BlIPP data (green) yielded a plasmon propagation distance of L_0 = 4.2 µm. The contribution from direct laser excitation (blue) to the photo-bleaching is also indicated. **(e)** Fluorescence image of a chain coated with rhodamine 6G and excited at 514 nm with a laser power of 31 nW. **(f)** Fluorescence image taken after exposure of the left end of the chain to 75 µW of 514 nm laser light for 5 minutes. The difference image, **(g)** and the normalized intensity line section (red) along the NP chain**, (h)** show no evidence of plasmon propagation as the BlIPP data was best described by photo-bleaching due to only direct laser excitation (blue).

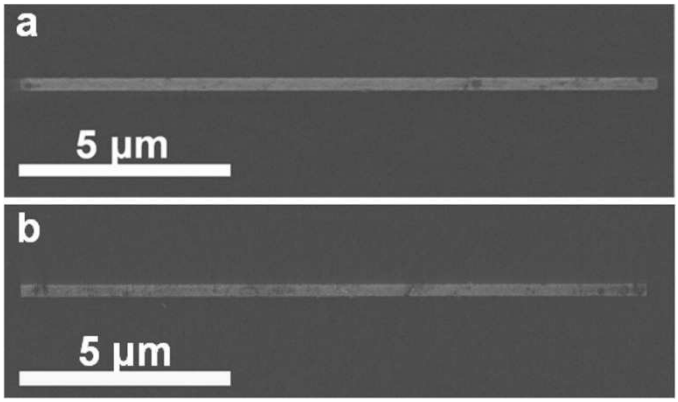

Figure 3.4 SEM image of the chains shown in Figure 3.3. **(a)** SEM image of the chain used for the BlIPP experiment with 785 nm excitation (Figures 3.3a-d). **(b)** SEM image of the chain used for the BlIPP experiment with 514 nm excitation (Figures 3.3e-h).

Next, the NP chain extinction spectrum shows that the lowest energy super-radiant plasmon mode was located at 1150nm, confirming that dark modes were present around 785 nm[30, 94, 96]. Furthermore, the absence of an intense extinction feature at even longer wavelengths confirms that, although the NPs are closely spaced in the strong-coupling regime, the metal surfaces of the NPs were not touching[103].

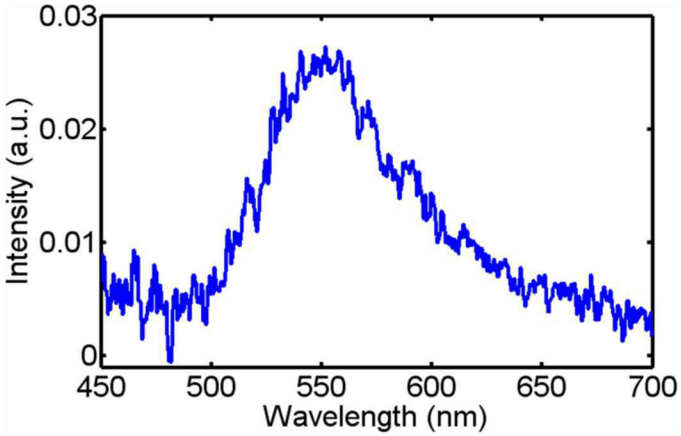

Figure 3.5 Scattering spectrum of a representative single 50 nm spherical Au NP.

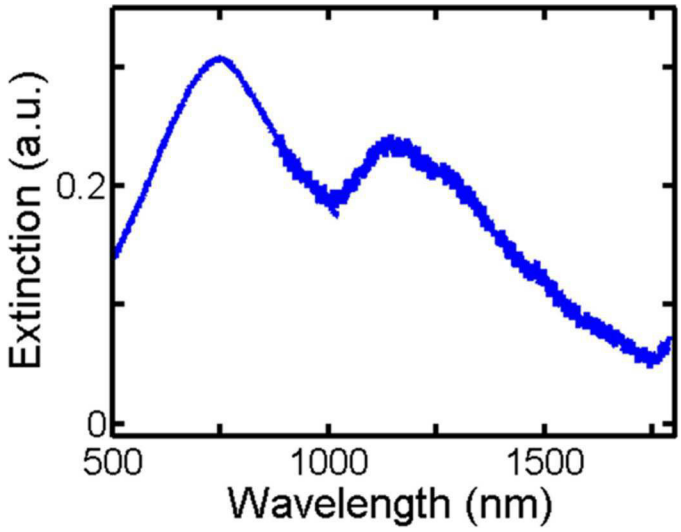

Figure 3.6 Extinction spectrum taken at the end of the chain shown in Figure 3.3. The absence of a plasmon mode at wavelengths longer than the peak at 1150 nm confirms the absence of conductive plasmon coupling of the NPs.

A line section of the photo-bleaching intensity taken along the chain in Figure 3.3c yielded a dark-mode plasmon propagation distance of $L_0 = 4.2\ \mu$m, approximately an order of magnitude longer than measured previously[32] for weakly-coupled NP chains excited at a bright mode. Figure 3.3d shows the data together with the best fit to a previously developed model for BlIPP, which is based on the photo-bleaching kinetics of the dye due to direct laser excitation and indirect excitation by the plasmonic near-field that decays exponentially along the waveguide.

Because coupling strongly depends on the geometry of the waveguide tip, absolute values for the coupling efficiency of light to NWs and NP chains are difficult to assess[59, 104]. Relative coupling efficiencies can be determined though by comparing the bleach intensities for the same incident power and exposure time as was done for parallel and perpendicular polarized excitation at 785 nm. We observed no significant difference in the propagation distances measured by BlIPP or relative coupling efficiency based on the bleach intensity between parallel and perpendicular excitation as shown in Figures 3.7 and 3.8, respectively. Interestingly, coupling to a propagating plasmon mode can also be achieved by exciting away from the waveguide end for these chains yielding again the same propagation distance (Figure 3.9). In contrast to NWs, for which conversion of photons into plasmons only occurs at the NW ends, any NP within the chain can effectively act as an input coupler.

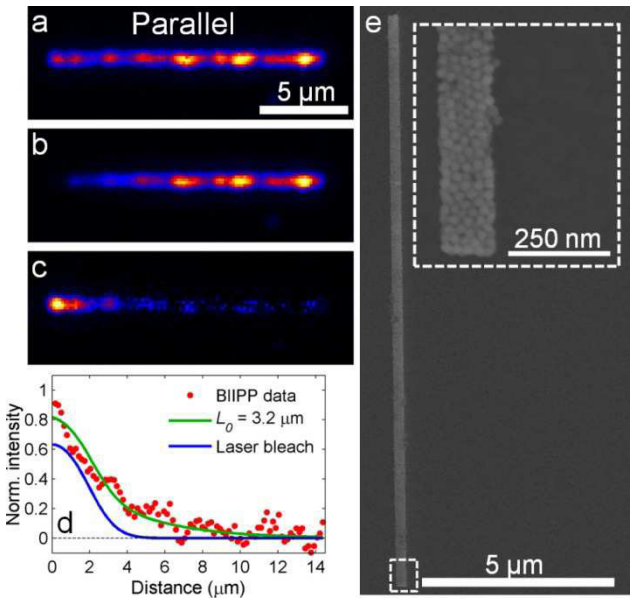

Figure 3.7 BIIPP experiment for a NP chain using 785 nm excitation polarized parallel to long axis of the chain. **(a)** Fluorescence image of a chain using a laser power of 66 nW acquired with an integration time of 10 ms/pixel. **(b)** Fluorescence of the same area in **a** after exposure to 9.8 μW of 785 nm linearly polarized laser light for 20 minutes. **(c)** Difference image created by subtracting **b** from **a**. **(d)** Plot of the normalized width-averaged line section of the photo-bleach intensity along the NP chain in **c** is shown by the red dots. The green line is a fit of the BIIPP data to the model presented above, giving a propagation distance of L_0 = 3.2 μm. The solid blue line indicates the contribution of direct laser bleaching to the BIIPP data. **(e)** SEM image of the chain shown in **a**.

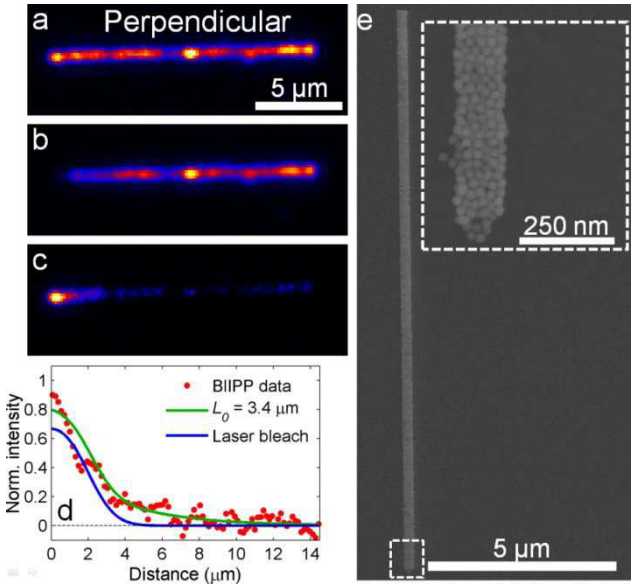

Figure 3.8 BlIPP experiment for a NP chain using 785 nm excitation polarized perpendicular to long axis of the chain. **(a)** Fluorescence image of a chain using a laser power of 66 nW acquired with an integration time of 10 ms/pixel. **(b)** Fluorescence of the same area in **a** after exposure to 9.8 µW of 785 nm linearly polarized laser light for 20 minutes. **(c)** Difference image created by subtracting **b** from **a**. **(d)** Plot of the normalized width-averaged line section of the photo-bleach intensity along the NP chain in **c** is shown by the red dots. The green line is a fit of the BlIPP data to the model presented above, giving a propagation distance of L_0 = 3.4 µm. The solid blue line indicates the contribution of direct laser bleaching to the BlIPP data. **(e)** SEM image of the chain shown in **a.**

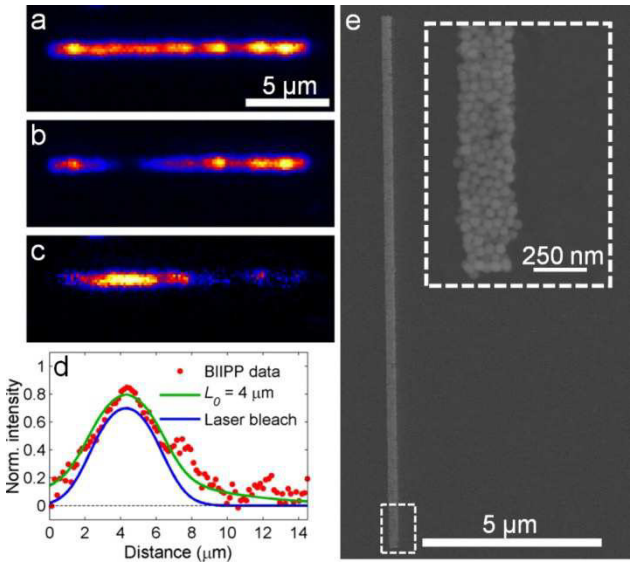

Figure 3.9 BlIPP experiment for a NP chain with 785 nm excitation away from the end of the chain. **(a)** Fluorescence image of a chain using a laser power of 60 nW acquired with an integration time of 10 ms/pixel. **(b)** Fluorescence of the same area in **a** after exposure to 12 µW of 785 nm circularly polarized laser light for 20 minutes. **(c)** Difference image created by subtracting **b** from **a**. **(d)** Plot of the normalized width-averaged line section of the photo-bleach intensity along the NP chain in **c** is shown by the red dots. The green line is a fit of the BlIPP data to the model presented above, giving a propagation distance of L_0 = 4.0 µm even for excitation away from the end of the chain. The solid blue line indicates the contribution of direct laser bleaching to the BlIPP data. **(e)** SEM image of the chain shown in **a**.

In contrast, no energy propagation was observed at 514 nm within the spatial resolution of our BlIPP technique (Figures. 3.3e-h and Figure 3.4). The difference image (Figure 3.3g) and the line section (Figure 3.3h), illustrate that photo-bleaching of the dye occurred only due to direct laser excitation as the bleached area was well described by only a Gaussian beam with no detectable contribution from an exponential plasmon decay. Independent photo-bleaching experiments without the NP chain (Figures 3.10 and 3.11) gave bleached areas with sizes comparable to the Gaussian laser component of the fit in Figure 3.3. The absence of long range energy propagation for 514 nm excitation at the single NP resonance can be attributed to larger radiative losses in combination with interband absorptions[37].

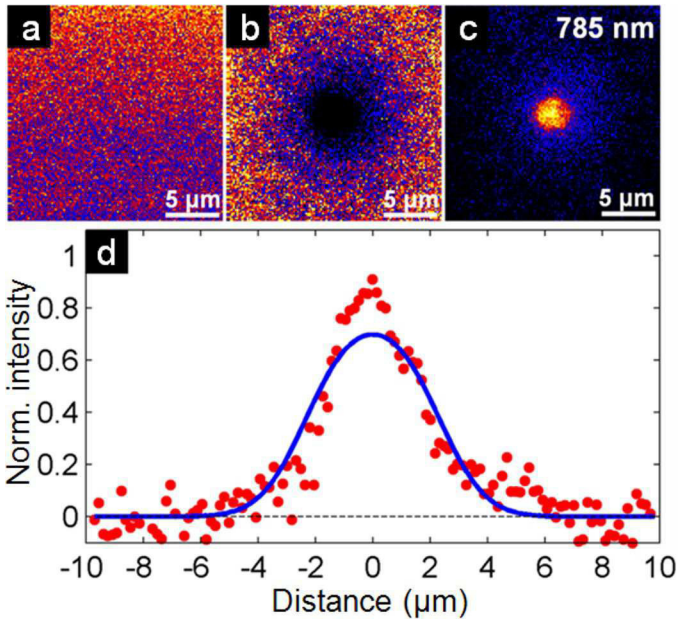

Figure 3.10 Direct photo-bleaching of a dye film excited at 785 nm. **(a)** Fluorescence image of a dye coated glass slide taken with a laser power of 66 nW. The dye film was created by spin coating a glass slide at 6000 rpm for 40 seconds with 3 µL of a cardiogreen/methanol solution having a concentration of 5 mg/mL. **(b)** Fluorescence image of the same area in **a** after high intensity laser exposure at 6.6 µW for 20 minutes. **(c)** Difference image created by subtracting **b** from **a**. **(d)** Plot of the normalized width-averaged line section from the difference image. Data points are given by the red dots yielding a FWHM of 3.4 µm. The solid blue line is a Gaussian curve representing the photo-bleaching due to direct laser excitation and was obtained by fitting the data with Equation 3.1 assuming no plasmon propagation. The width of the Gaussian curve is comparable to the laser component obtained for the analysis of the BlIPP data shown in Figure 3.3d. It is important to note that the conditions (laser power and exposure time) for the dye film were similar to the BlIPP experiments performed on the NP chains.

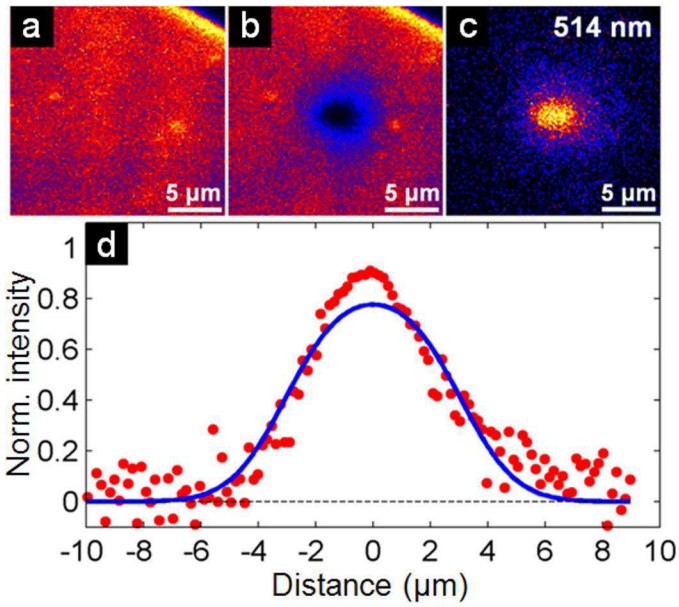

Figure 3.11 Direct photo-bleaching of a dye film excited at 514 nm. **(a)** Fluorescence image of a dye coated glass slide taken with a laser power of 31 nW. The dye film was created by spin coating a glass slide at 6000 rpm for 40 seconds with 3 µL of a rhodamine 6G/methanol solution having a concentration of 5 mg/mL. **(b)** Fluorescence image of the same area in **a** after high intensity laser exposure at 75 µW for 5 minutes. **(c)** Difference image created by subtracting **b** from **a**. **(d)** Plot of the normalized width-averaged line section from the difference image. Data points are given by the red dots yielding a FWHM of 5.3 µm. The solid blue line is a Gaussian curve representing the photo-bleaching due to direct laser excitation and was obtained by fitting the data with Equation 3.1 assuming no plasmon propagation. The width of the Gaussian curve is comparable to the laser component obtained for the analysis of the BlIPP data shown in Figure 3.3h. It is important to note that the conditions (laser power and exposure time) for the dye film were similar to the BlIPP experiments performed on the NP chains.

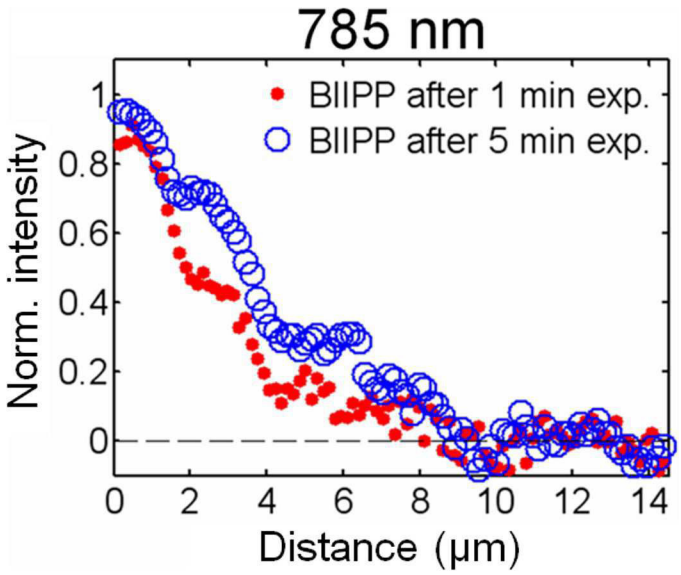

Figure 3.12 BlIPP for a NP chain as a function of exposure time for 785 nm excitation. The red and blue data points show the normalized photo-bleach intensity line sections obtained for two different exposure times of 1 and 5 minutes, respectively. The fluorescence images were recorded using 30 nW while end excitation was carried out at a higher exposure power of 30.3 μW.

To ensure though that the results for 514 nm were not due to a difference in relative efficiency for coupling light into the waveguide, we varied the laser power and exposure time for 785 and 514 nm excitation. While for 785 nm the bleach intensity along the chain increased due to plasmon propagation (Figure 3.12), for 514 nm, only direct laser excitation caused photo-bleaching despite using higher laser powers and longer exposure times (Figure 3.13). These results also rule out the possibility of thermally-induced photobleaching. We can furthermore neglect the presence of the dye itself as the cause for the observed energy transport because destroying a section of the dye on a waveguide prior to the BlIPP measurement had no effect on the propagation distance (Figure. 3.14). However, similar to other far-field measurements of SP propagation it is possible that BLIPP is more sensitive to certain modes. For example, leakage radiation is only a measure of propagating plasmons within the substrate light cone[105, 106].

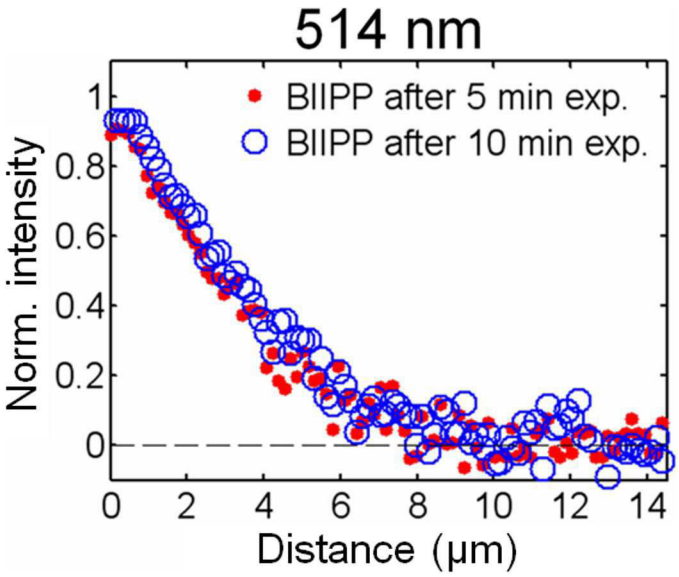

Figure 3.13 BIIPP for a NP chain as a function of exposure time for 514 nm excitation. The red and blue data points show the normalized photo-bleach intensity line sections obtained for two different exposure times of 5 and 10 minutes, respectively. The fluorescence images were recorded using 31 nW while end excitation was carried out at a higher exposure power of 75 μW.

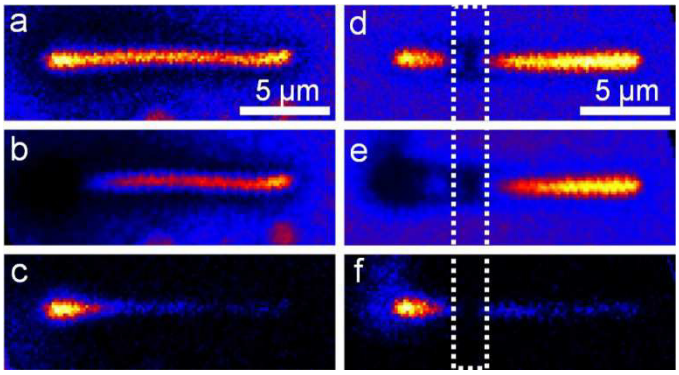

Figure 3.14 Effect of dye on the propagation distance. **(a)** Fluorescence image of a Au NW using a laser power of 66 nW at 785 nm acquired with an integration time of 10 ms/pixel. **(b)** Fluorescence image of the same area in **a** after exposure to 7.5 µW of 785 nm laser light for 40 minutes. **(c)** Difference image created by subtracting **b** from **a**. **(d)** Fluorescence image of another Au NW using a laser power of 66 nW acquired with an integration time of 10 ms/pixel. The large gap in fluorescence in the middle of the NW (highlighted by the dotted line) was created by photobleaching the dye by direct excitation at that spatial location by 785 nm laser light at an exposure power of 10 µW for 5 minutes. **(e)** Fluorescence image of the same area in **d** after exposure to 10 µW of 785 nm laser light for 40 minutes at the left end of the NW. **(f)** Difference image created by subtracting **e** from **d**. Photobleaching due to plasmon propagation is clearly visible along the entire length of the NW despite the noticeable gap in the fluorescence in the middle of the wire. The sample was prepared by drop-casting a solution of Au NWs (12-18 µm x 50-100 nm) onto a cleaned glass slide. The thin film dye coating was created by spin coating 30 µL of a 0.05% solution of cardiogreen in methanol onto the sample at 6000 rpm. No methanol rinse was performed after the spin coating procedure, which causes a larger residual background fluorescence in these images compared to the NP chains. Both Au NWs were found to have comparable propagation distances indicating that the presence of the dye has no significant effect on the determination of the propagation distance. This experiment was performed because gain media like dye molecules can in principle compensate absorption losses and therefore enhance the plasmon propagation distance. This however, requires strong optical pumping of the gain medium to achieve population inversion. In our BlIPP experiments, intense photo-excitation was limited to only one end of the chain and furthermore quickly destroyed the dye molecules there at the beginning of the experiment, while photo-bleaching along the NP chain slowly accumulated over time through interactions with a much weaker plasmon near-field. In fact, because of enhanced losses due to ground state absorption by the chromophores, BlIPP might slightly underestimate the plasmon propagation distance in these NP chains. These experiments on the Au NWs shown here further confirm that coupling between plasmon and dye excitations do not play any other role than to monitor the intrinsic plasmonic near-field that decays exponentially along the waveguide structure. The NW was chosen for this test because bleaching of the dye in the middle of the waveguide leads to plasmon propagation for the NP chains as illustrated in Figure 3.9.

A generalized Mie theory simulation both supports our experimental results and contributes new insights. The simulated near-field intensity for a 10 μm long NP chain excited at 785 nm indeed confirmed long plasmon propagation (Figure 3.15a). By fitting the intensity profile along the NP chain an exponential decay distance of L_0 = 1.7 µm was obtained(Figure 3.15b). The shorter theoretical propagation distance is likely because the calculations. The simulated charge distribution (Figure 3.16) confirmed the sub-radiant

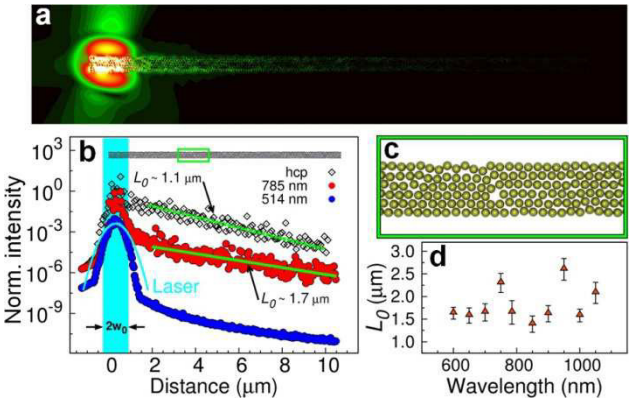

Figure 3.15 Generalized Mie theory simulations of plasmon propagation in Au NP chains. **(a)** Near-field intensity of the laser profile and plasmon propagation in a 1200 NP chain for excitation at 785 nm. **(b)** Decay of the width-averaged near-field intensity along the NP chain for 785 nm (red) compared to 514 nm (blue) excitation. The latter mimicked the laser intensity (cyan) confirming minimal energy propagation for excitation near the single NP plasmon resonance because of the strong intrinsic damping of Au. In contrast, the coupled plasmon modes excited at 785 nm sustained energy transport due to minimized losses with a propagation distance of L_0 = 1.7 μm. A hexagonal close-packed (hcp) arrangement gave a shorter propagation distance of L_0 = 1.1 μm (black, open symbols), illustrating that disorder enhances energy transport. **(c)** Section of the chain modeled in **a**, showing closely spaced 50 nm spherical Au NPs with random positions to account for local disorder. The minimum surface to surface separation was always kept at 1 nm. **(d)** Propagation distances for different wavelengths demonstrating the large bandwidth that is achievable for plasmon propagation via low-loss sub-radiant modes. The errors were calculated by simulating different random NP arrangements.

nature of this plasmon mode[30, 92, 96, 107]. However, 514 nm excitation resulted in minimal actual NPs were faceted and packed in three dimensions with separations possibly smaller than the minimum separation of 1 nm used in the energy propagation. It is important to note that, because of strong coupling that results from the small inter-particle distances, 15 multipole modes were considered in these simulations. In contrast, it is primarily the dipole mode that contributes in assemblies with larger inter-particle distances[32, 108].

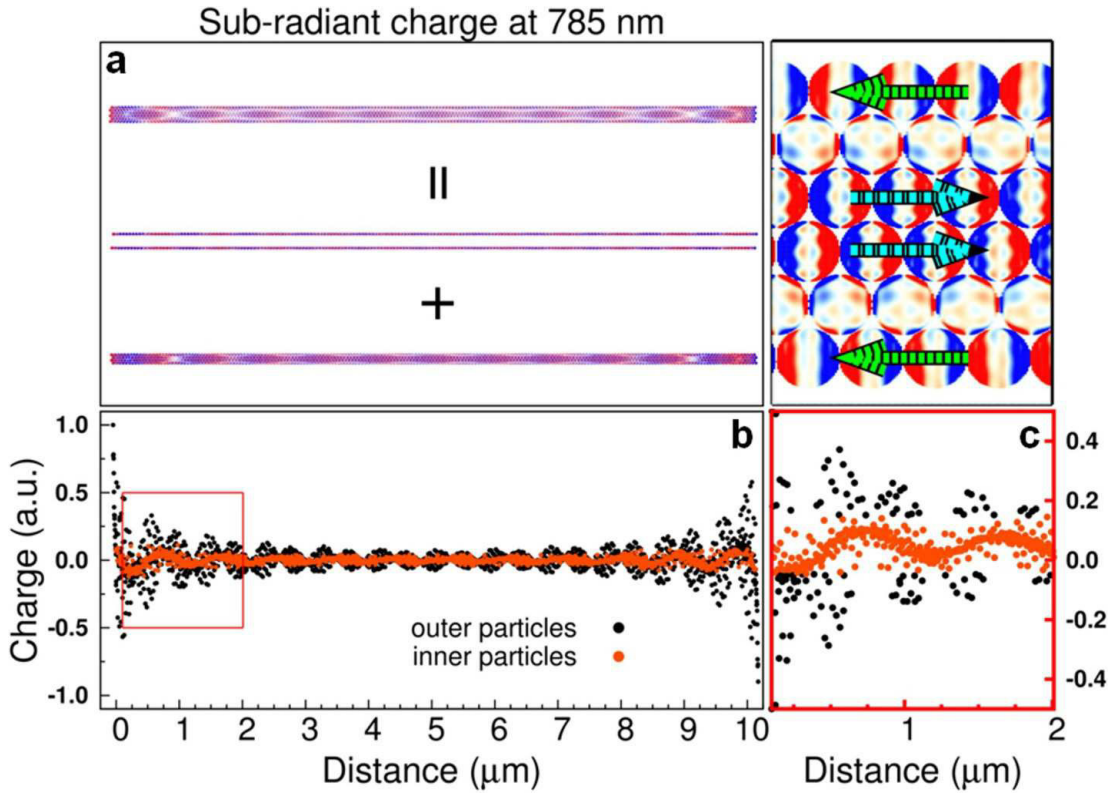

Figure 3.16 Sub-radiant response of a hexagonal close-packed array of 50 nm Au NPs upon coherent plane wave excitation at 785nm. **(a)** The sub-radiant nature of the excited plasmon modes is identified by bands of alternating positive and negative charge domains (red and blue, respectively) along the length of the chain in the calculated charge plots. Charge contributions can be separated into domains of different phase, being localized to regions on the edge and within the interior of the NP assembly as further highlighted by the higher magnification charge plot in the right-hand panel. **(b)** Width-averaged line section of the surface charge highlights the standing wave oscillations, characteristic of the sub-radiant eigen-response of the system. **(c)** Closer inspection (red-box) of the charge oscillations illustrates that the resonant domains are roughly 180° out of phase.

Interestingly, the new information provided by the simulations is the discovery that including disorder of the NP arrangement in the simulations to represent the experimental structures increased the plasmon propagation distance, similar to effects observed in photonic quasicrystals[109]. The NP chain was modeled as a random 2-dimensional assembly (Figure 3.15c). Comparing different random NP arrangements to an ordered hexagonal close-packed (hcp) array showed enhanced plasmon propagation if local disorder was included (Figure 3.15b and Figure 3.17).

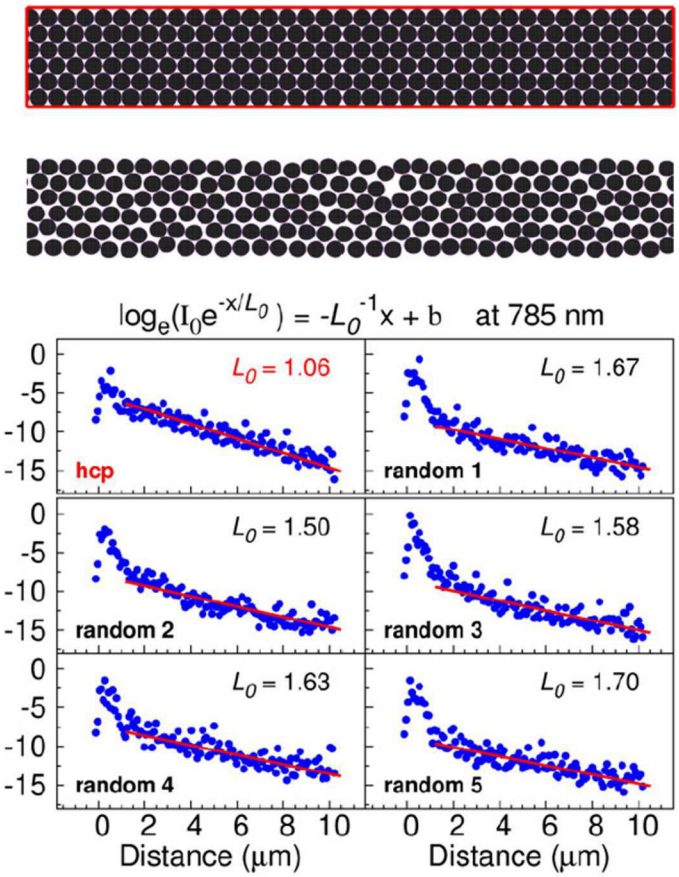

Figure 3.17 Comparison of the plasmon propagation distances for a 2-dimensional hexagonal closed-packed Au NP chain vs. five randomly created NP assemblies in which disorder has been introduced. Excitation at 785 nm for a hexagonal closed-packed arrangement of 50 nm Au NPs resulted in a shorter propagation distance compared to chain structures of the same length with added local disorder.

Furthermore, sub-radiant plasmon modes have the advantage of a large frequency bandwidth[30]. To show this, we calculated plasmon propagation distances for excitation wavelengths in the range of 600 -1050 nm (Figure 3.18). As summarized in Figure 3.15d, a propagation distance as long as L_0 = 2.6 μm was obtained at 950 nm, while all values were larger than 1.5 μm for the entire bandwidth sampled.

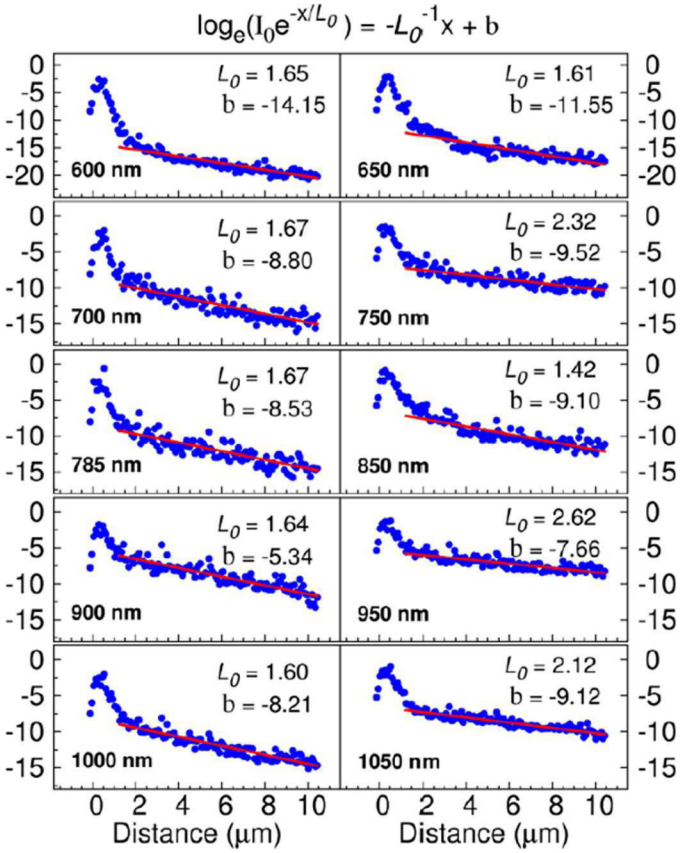

Figure 3.18 Decay of the width-averaged near-field intensity along a NP chain for different excitation wavelengths. The intensity is plotted on a logarithmic scale and fitting of the data points to the right of the laser response yielded 1/e propagation distances L_0, which are summarized in Figure 3.15d.

The long energy propagation in these NP chains was observed to be highly reproducible. The dark-mode 785 nm BlIPP experiment was repeated for 59 structures, and evidence was found for energy transport in ~ 90% of the chains. Figures 3.19 and 3.20 show two additional examples of plasmon propagation along the entire length of the chain, as found for ~ 40% of the waveguides yielding an average propagation distance of $L_0 = 3.9 \pm 0.6$ μm. Long range plasmon propagation also does not require broad chains (Figure 3.21), as reducing the width of the chains to about 3 NPs had no measurable effect on the propagation distance. Further reducing the width of the chains to only one NP while avoiding larger gaps (see below) is, however, challenging with the current procedure. Simulations indicate that such a system, while offering stronger confinement,

is not necessarily desirable, as the calculated propagation distance is reduced by a factor of 3 (Figure 3.22). A similar tradeoff between confinement and propagation distance has also been observed for other plasmonic waveguides[106].

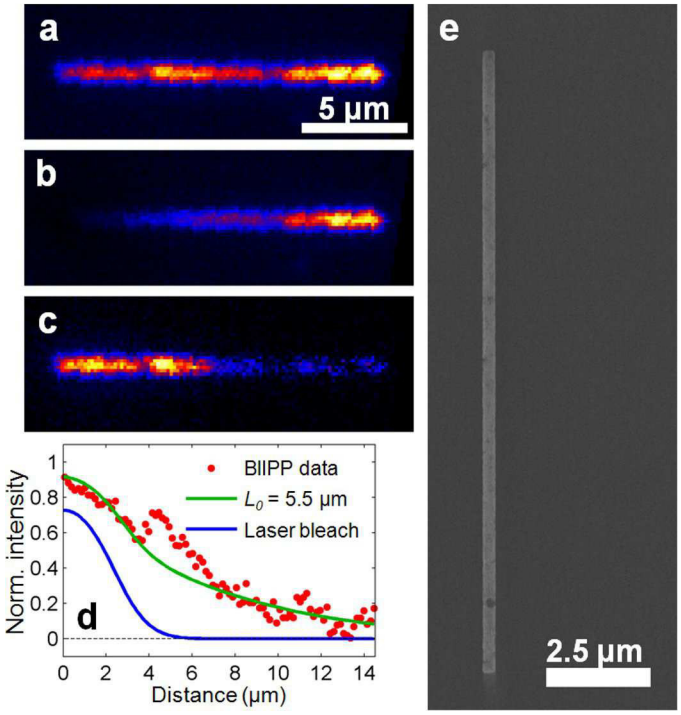

Figure 3.19 BlIPP experiment for a NP chain using 785 nm excitation. **(a)** Fluorescence image of a chain using a laser power of 66 nW acquired with an integration time of 10 ms/pixel. **(b)** Fluorescence of the same area in **a** after exposure to 7.2 µW of 785 nm circularly polarized laser light for 20 minutes. **(c)** Difference image created by subtracting **b** from **a**. **(d)** Plot of the normalized width-averaged line section of the photo-bleach intensity along the NP chain in **c** is shown by the red dots. The green line is a fit of the BlIPP data to the model presented above, giving a propagation distance of L_0 = 5.5 µm. The sold blue line indicates the contribution of direct laser bleaching to the BlIPP data. **(e)** SEM image of the chain shown in **a**. This sample is different from the chains shown in Figure 3.3 and Figure 3.20.

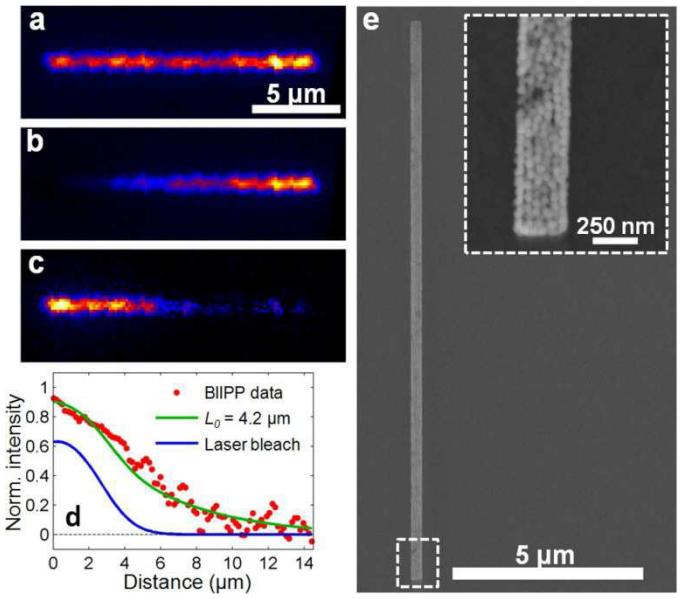

Figure 3.20 BlIPP experiment for a NP chain using 785 nm excitation. **(a)** Fluorescence image of a chain using a laser power of 66 nW acquired with an integration time of 10 ms/pixel. **(b)** Fluorescence of the same area in **a** after exposure to 7.2 µW of 785 nm circularly polarized laser light for 20 minutes. **(c)** Difference image created by subtracting **b** from **a**. **(d)** Plot of the normalized width-averaged line section of the photo-bleach intensity along the NP chain in **c** is shown by the red dots. The green line is a fit of the BlIPP data to the model presented above, giving a propagation distance of L_0 = 4.2 µm. The sold blue line indicates the contribution of direct laser bleaching to the BlIPP data. **(e)** SEM image of the chain shown in **a**. The inset shows a magnified SEM image at the end of the chain where laser excitation was carried out. The image was taken after the BlIPP experiment and shows no damage due laser heating. This sample is different from the chains shown in Figure 3.3 and Figure 3.19.

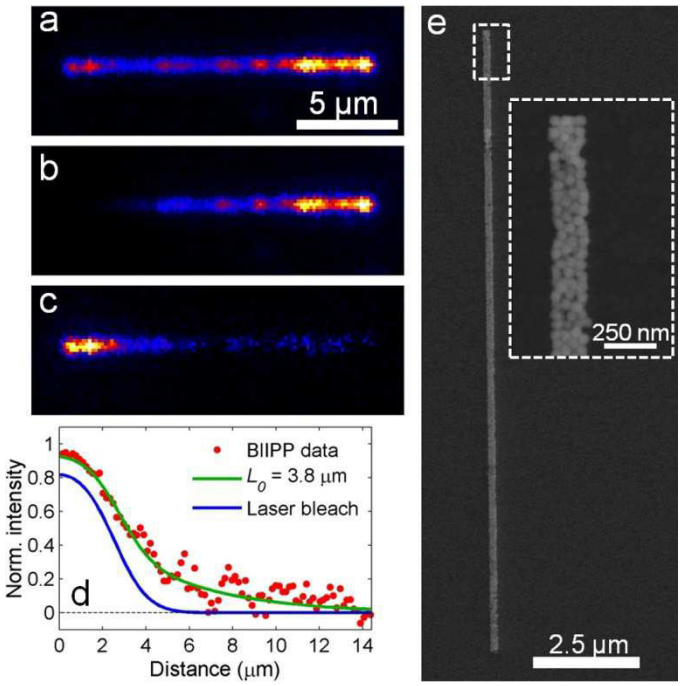

Figure 3.21 BlIPP experiment for a narrower NP chain using 785 nm excitation. **(a)** Fluorescence image of a Au NP chain having a width of 200 nm using a laser power of 30 nW acquired with an integration time of 10 ms/pixel. **(b)** Fluorescence of the same area in **a** after exposure to 24 µW of 785 nm laser light for 30 minutes. **(c)** Difference image created by subtracting **b** from **a**. **(d)** Plot of the normalized width-averaged line section of the photo-bleach intensity along the NP chain in **c** is shown by the red dots. The green line is a fit of the BlIPP data to the model presented above, giving a propagation distance of L_0 = 3.8 µm. The sold blue line indicates the contribution of direct laser bleaching to the BlIPP data. **(e)** SEM image of the chain shown in **a**. The high magnification image in the inset shows that the chain is ~ 3 NPs wide, and 1 – 2 layers high.

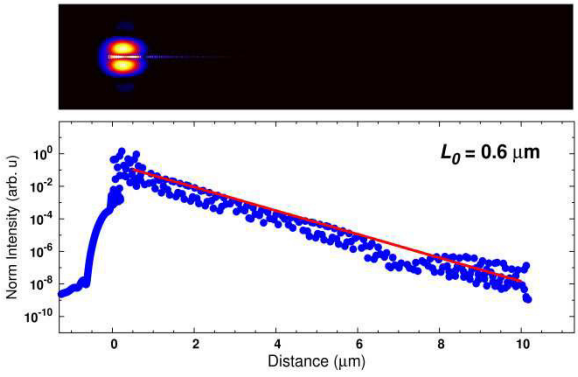

Figure 3.22 Generalized Mie theory simulation of a one particle wide chain. **(a)** Near-field intensity of the laser profile and plasmon propagation in a 200 NP long ideal linear chain for excitation at 785 nm. The total length of the chain is the same as for all other chains modeled. **(b)** Decay of the width-averaged near-field intensity along the NP chain for 785 nm, shown in blue. Fitting reveals a measured propagation length of 0.6 µm as shown by the red line.

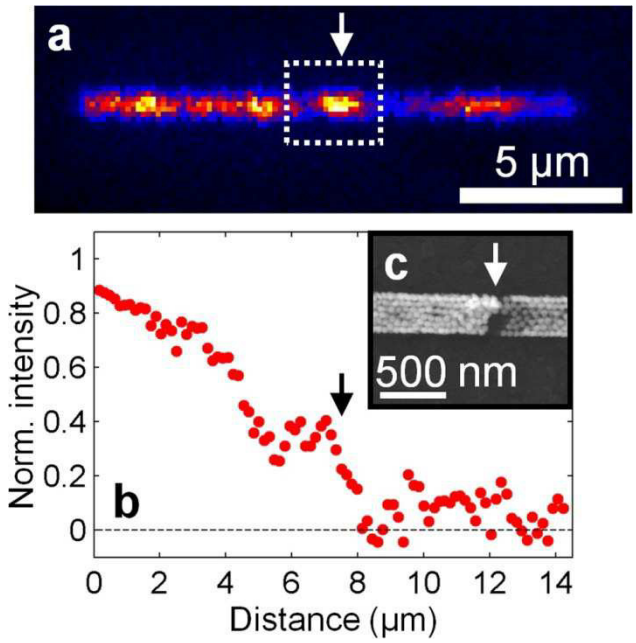

Figure 3.23 Energy localization at a chain defect. (**a)** Fluorescence image of a Au NP chain coated with cardiogreen and excited at 785 nm with a laser power of 63 nW. The white arrow highlights a region of increased fluorescence intensity. **(b)** Normalized photo-bleaching intensity along the NP chain obtained from the BlIPP analysis. The location of the area shown in **a** is highlighted by the black arrow and is associated with a sharp decrease of the bleach intensity indicating a break in the plasmon propagation for this waveguide. **(c)** SEM image of the same chain region demonstrates that energy propagation was hindered by the presence of a large defect composed of several missing NPs.

In contrast, energy transport is strongly damped at large-scale defects along the NP chain (Figure 3.23 and Figures 3.24 and 3.25). The fluorescence image in Figure 3.23a, taken before photo-bleaching, shows an area of increased fluorescence intensity at 7.5 μm, which corresponds to an abrupt drop in the bleach intensity (Figure 3.23b). SEM images revealed a large hole defect in the NP arrangement at this position (Figure 3.23c). This explains why 50% of the chains showed energy transport but could not be fitted to an exponential decay. The larger hole defects, when examined in the SEM images, are of the same dimensions as the inter-particle separations for top-down fabricated chains. This emphasizes why long range energy transport was not observed before in such structures.

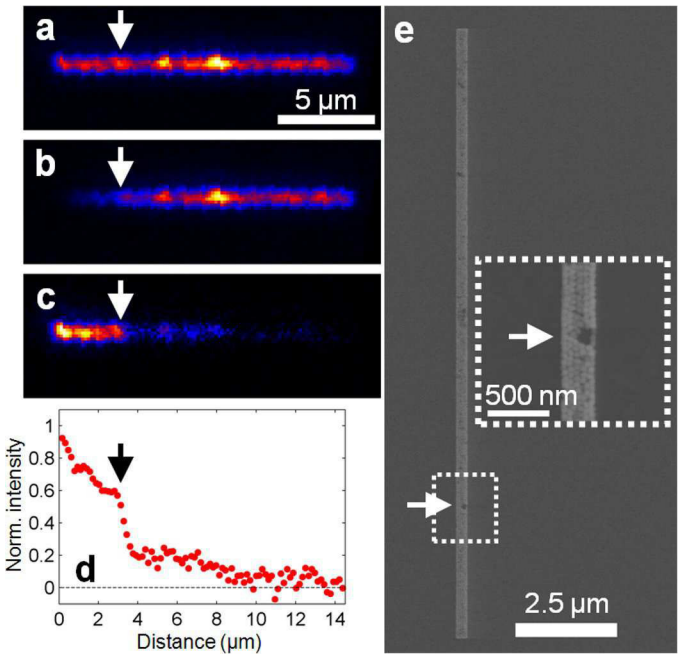

Figure 3.24 Correlation of breaks in plasmon propagation to chain defects. **(a)** Fluorescence image of a chain using 785 nm laser excitation recorded at a power of 30 nW with an integration time of 10 ms/pixel. **(b)** Fluorescence of the same area in **a** after an exposure period of 5 minutes with 24 µW. **(c)** Difference image created by subtracting **b** from **a**. **(d)** Plot of the width-averaged line section of the photo-bleach intensity along the NP chain in **c** is shown by the red dots. **(e)** SEM image of the chain shown in **a**. The chain was excited at the bottom end in the SEM image. The white arrows in **a**, **b**, **c**, and **e** and the black arrow in **d** highlight the same region of the chain as shown in the higher magnification SEM image in the inset of **e**. The drop in the photo-bleach intensity and hence plasmon propagation in **d** is directly correlated with a large defect composed of missing NPs as shown in the inset of **e**. This sample is different from the chains shown in Figure 3.23 and Figure 3.25.

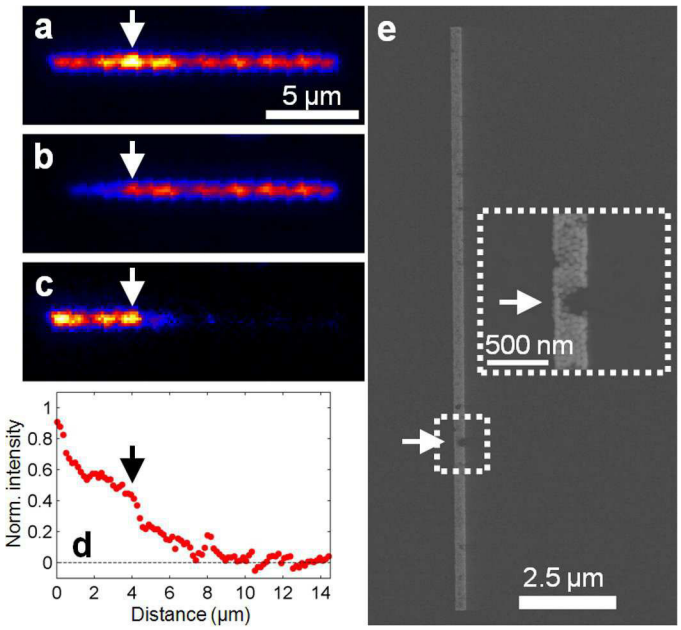

Figure 3.25 Correlation of breaks in plasmon propagation to chain defects. **(a)** Fluorescence image of a chain using 785 nm laser excitation recorded at a power of 30 nW with an integration time of 10 ms/pixel. **(b)** Fluorescence of the same area in **a** after an exposure period of 3 minutes with 24 µW. **(c)** Difference image created by subtracting **b** from **a**. **(d)** Plot of the width-averaged line section of the photo-bleach intensity along the NP chain in **c** is shown by the red dots. **(e)** SEM image of the chain shown in **a**. The chain was excited at the bottom end in the SEM image. The white arrows in **a**, **b**, **c**, and **e** and the black arrow in **d** highlight the same region of the chain as shown in the higher magnification SEM image in the inset of **e**. The drop in the photo-bleach intensity and hence plasmon propagation in **d** is directly correlated with a large defect composed of missing NPs as shown in the inset of **e**. This sample is different from the chains shown in Figure 3.23 and Figure 3.24.

3.5 Conclusions

In summary, we present evidence that dark-mode plasmon propagation in strongly-coupled Au NPs can be exploited to obtain micrometer-scale energy transport. Additionally, simulations suggest that the intrinsic heterogeneity of bottom-up NP preparations can actually increase propagation distances. Finally, the combination of large area printing methods to create ordered templates[110], together with bottom-up NP synthesis and assembly, opens the possibility of preparing inexpensive chain assemblies for novel plasmonic opto-electronic applications. These results have important implications for engineering ultra-compact opto-electronic devices with NP plasmons, in

that they suggest the possibility for large area fabrication of NP assemblies that yield close inter-particle distances, while tolerating or even exploiting the types of heterogeneity intrinsic to bottom-up assembly methods.

3.6 Acknowledgements

This work was funded by the Robert A. Welch Foundation (C-1664), the Office of Naval Research (N00014-10-1-0989), NSF (CHE-0955286), the ACS Petroleum Research Fund (50191-DNI6), and a 3M Nontenured Faculty Grant. DS was supported by an NSF Graduate Research Fellowship Grant No. (0940902) and PS acknowledges support from the Royal Thai Government. We thank Dr. Christy Landes for help preparing the manuscript.

CHAPTER 4

A MECHANISTIC STUDY OF BLEACH-IMAGED PLASMON PROPAGATION (BLIPP)[3]

4.1 Abstract

Bleach-imaged plasmon propagation, BlIPP, is a far-field microscopy technique developed to characterize the propagation length of SPPs in metallic waveguides. To correctly extract the propagation length from the measured photobleach intensity, it is necessary to understand the mechanism by which dye photobleaching occurs. In particular, 1- vs. 2-photon bleaching reactions yield different propagation lengths based on a kinetic model for BlIPP. Because a number of studies have reported on the importance of 2-photon processes for dye photobleaching, we investigate here the nature of the photobleaching step in BlIPP. We are able to demonstrate that only 1-photon absorption is relevant for typical BlIPP conditions as tested here for a thin film of indocyanine green fluorescent dye molecules coated over Au NWs and excited at a wavelength of 785 nm. These results are obtained by directly measuring the excitation intensity dependence of the photobleaching rate constant of the dye in the presence of the metallic waveguide.

4.2 Introduction

Sub-wavelength wide plasmonic waveguides have the ability to confine electromagnetic energy on length scales below the diffraction limit and to transfer this

[3] Reprinted (adapted) with permission from "A Mechanistic Study of Bleach-Imaged Plasmon Propagation (BlIPP)" by David Solis Jr., Aniruddha Paul, Wei-Shun Chang and Stephan Link, *The Journal of Physical Chemistry B* **ASAP**, XX, (XX), XXXX-XXXX. Copyright 2013 American Chemical Society.

energy over distances much larger than the lateral size of the waveguide through coupling of incident light to coherent oscillations of the free electrons, known as SPPs.[1, 9, 18, 31, 37, 111] Metallic waveguides are, however, inherently prone to loss, and many studies have been aimed at understanding and minimizing these unwanted losses. Examples include controlling the waveguide morphology and crystallinity,[30, 47, 112-114] optimizing light coupling schemes,[63, 115] and using metamaterials[76] and different surface coatings.[42, 78, 116, 117] The damping of a SPP is characterized by an exponential decay of the near-field intensity from the point of optical excitation. This plasmon propagation length, L_0, has been measured through several methods such as near-field scanning optical microscopy,[40, 63] leakage radiation microscopy,[42, 113, 118] and far-field fluorescence microscopy including direct fluorescence imaging[28, 43] and its inverse analogue bleach-imaged plasmon propagation (BlIPP).[26, 27, 29]

In fluorescence microscopy methods, a thin film of a fluorescent dye or polymer is coated on top of the plasmonic waveguide and indirect excitation of the chromophore by the near-field of the propagating SPP is read out by a standard far-field microscope. Direct fluorescence imaging and BlIPP are in many aspects complementary to each other and have different advantages. Direct fluorescence imaging is usually carried out by imaging the fluorescence intensity directly on a CCD camera to spatially resolve the fluorescence intensity along the plasmonic waveguide while exciting one end with a laser. This method is characterized by short acquisition times and allows multiple measurements on the same waveguide. However, the laser excitation itself creates a strong fluorescence background that, especially for short propagation distances, can completely mask weaker fluorescence induced by the plasmonic near-field.

Photobleaching of the dye film for high laser excitation intensities and long or repeated exposure times can also potentially affect the measured plasmon propagation length.

BlIPP, on the other hand, utilizes the photobleaching of the fluorescent molecules to create a permanent map of the plasmonic near-field, which is then read out by a low intensity, non-destructive probe beam. Because direct photobleaching by the excitation laser stops when all dye molecules are bleached, short propagation lengths as well as weak modes can be amplified in comparison, as indirect photobleaching through the plasmonic near-field continuously increases with increasing exposure time. Furthermore, by taking into account the spatial intensity profile of the excitation beam, BlIPP has successfully been used to record plasmon propagation lengths shorter than 2 μm in Au NW excited at 532 nm[27]. However, as with other indirect detection schemes, the correct extraction of the plasmon propagation length using BlIPP strongly depends on the underlying mechanism of the dye photobleaching reaction on top of the plasmonic waveguide structures. In previous BlIPP studies, the photobleaching mechanism was assumed to be based on a one-photon process,[26, 27, 29] although at high excitation intensities two-photon induced photobleaching is also possible.[119-121]

In this study we examine in detail the photobleaching reaction in BlIPP measurements and its effect on the determination of the plasmon propagation length. We first present a kinetic model describing the measured signal intensity in BlIPP and then take a closer look at the excitation intensity, I, dependence of the photobleaching rate constant, k_{bl}. In particular, we investigate if photobleaching on top of a Au NW occurs solely via one-photon absorption or whether two-photon absorption also plays a role as these two photobleaching mechanisms give plasmon propagation lengths that differ by a

factor of 2. This is important because both 1- and 2-photon photobleaching reactions are well-documented in the literature.[119-122] We therefore determined k_{bl} as a function of I, where a 1-photon process should give a linear relationship between k_{bl} and I, whereas a 2-photon process should show a quadratic dependence with k_{bl} being proportional to I^2.[119, 121]

4.3 Experimental

4.3.1 Materials and Sample Preparation

Samples were prepared by first drop casting a solution of CTAB (cetyltrimethylammoniun bromide) capped Au NWs (10-15 μm long with a diameter of 90 ± 10 nm) onto a clean glass coverslip. Excess CTAB was removed from the substrate by washing with ethanol followed by drying under a nitrogen flow. The Au NWs were synthesized via tip selective growth of purified pentahedrally twinned Au nanorods, a method which has been shown to produce smooth, highly crystalline NWs.[26, 51] The Au NWs were coated with a thin dye film, which was created by spin coating 30 μL of a 0.5 mg/mL indocyanine green (ICG, Sigma Aldrich) solution in methanol onto a glass coverslip decorated with Au NWs at 6000 rpm for 50 seconds. The dye film thickness was measured to be 5 ± 1 nm as determined by atomic force microscopy (Veeco).[26] This sample was then placed on a home-built confocal fluorescence microscope, which used a diode laser (Power Technology) with an operating wavelength of 785 nm for the measurements reported here. Circular polarized light with a ratio of the minor polarization axis to the major polarization axis > 0.6 was used and the laser intensity was varied using neutral density filters. The small degree of elliptical polarization had no

effect on the fluorescence enhancement and dye photobleaching. The laser beam was directed into the body of an inverted microscope (Zeiss) where it was reflected by a dichroic mirror into a 50× objective (numerical aperture of 0.8) and focused onto the dye coated side of the Au NW sample, which was attached to a XYZ piezo scanning stage (Physik Instrumente). Fluorescence from the excited dye molecules was then collected by the same objective in an epi-fluorescence geometry and focused onto an avalanche photo-diode detector (Perkin Elmer). Fluorescence images were acquired by scanning the sample with the piezo stage which was controlled by a surface probe microscope controller (RHK Technology).[68] Fluorescence intensity time transients were collected on a separate counter board (Becker & Hickl). Fluorescence intensity data and image processing were performed using Matlab. The beam waist of the focused laser at the sample, as defined by the diameter measured at the $1/e^2$ intensity values, was measured to be 1000 ± 60 nm using the confocal scattering signal from individual Au nanorods and was used to calculate the excitation intensity per unit area.

4.3.2 BlIPP Experimental Overview

BlIPP at 785 nm is demonstrated in Figure 4.1 for Au NWs overcoated with ICG. A fluorescence image of the dye emission was first collected at a low excitation intensity by scanning the sample over a tightly focused laser beam. This low excitation intensity was found to cause negligible photobleaching as evaluated in Figure 4.2. The fluorescence of the ICG molecules was enhanced on top of the Au NW due to coupling to the NW plasmon modes.[68, 123] The image in Figure 4.1A shows the Au NW on top of background fluorescence. The Au NW was then positioned in such a way that the same

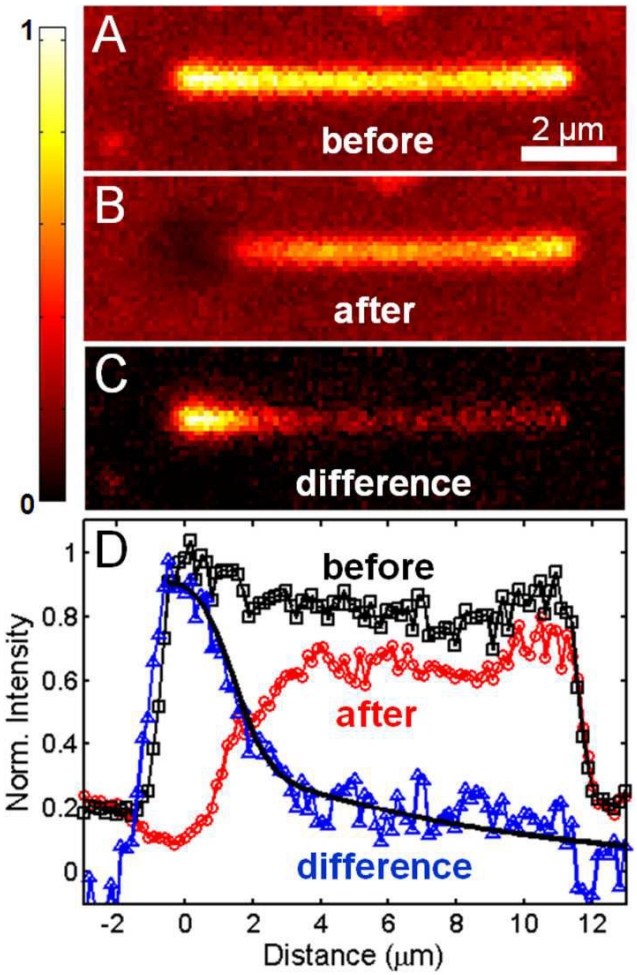

Figure 4.1 Bleach-Imaged Plasmon Propagation (BlIPP). **(A)** Sample scanned confocal fluorescence image of an Au NW coated with ICG dye excited at 785 nm using a laser intensity of 8.0 W/cm^2. **(B)** Fluorescence image of the same area after irradiating with a laser intensity of 1.25 kW/cm^2 at the left end of the NW for 20 minutes. **(C)** Difference image obtained by subtracting (B) from (A) yielding the bleach intensity. **(D)** Width-averaged intensity line-sections along the long NW axis shown for before (black squares) and after (red circles) photobleaching as well as the beach intensity line section (blue triangles) extracted from the difference image, where each point of the difference line-section has been normalized to its corresponding point in the fluorescent image before photobleaching. The black line is a fit to equation 7 yielding a propagation length of $L_0 = 7.5 \pm 1.0$ μm.

excitation laser was exciting one of the NW ends (the left end for Figure 4.1) at a higher excitation intensity. Because of symmetry breaking at the NW end the laser can couple to propagating SP modes, which decay exponentially along the NW due to mostly intrinsic non-radiative damping.[9, 34, 36, 40] The near-field of the propagating plasmon modes, however, also excited the ICG molecules, which due to their limited photostability, photobleached as the end-excitation was continued for 20 minutes. This photobleaching

was then measured by acquiring another fluorescence image (Figure 4.1B) with the original lower excitation intensity. Because photobleaching also occurred from direct laser excitation at the NW end, it is easier to visualize the degree of photobleaching along the NW by creating a difference image (Figure 4.1C). The photobleach intensity averaged over the width of the NW as shown in Figure 4.1D (blue data points) is then used to extract the plasmon propagation length, L_0. For Au NWs as the one shown in Figure 4.1 we previously obtained an average propagation length of $\langle L_0 \rangle = 7.5 \pm 2.0$ µm, which corresponds to the higher order $m = 1$ mode because the fundamental $m = 0$ mode is quenched under these experimental conditions.[26]

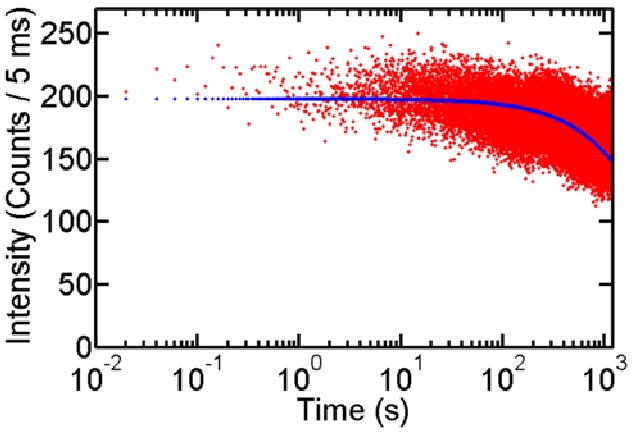

Figure 4.2 Fluorescence intensity as a function of time for a total exposure time of 20 minutes and at an excitation intensity of 8.0 W/cm^2 corresponding to the low intensity value that was used to acquire fluorescence images before photobleaching in BlIPP experiments. This data demonstrates that the low excitation intensity of 8.0 W/cm^2 still leads to photobleaching for long exposure times. However, considering the associated photobleaching rate of $k_{bl} = (3.5 \pm 1.1)*10^{-4}$ s^{-1} and average exposure time per area given by the speed of image acquisition, we can conclude that this low excitation intensity leads to overall negligible photobleaching. In particular, for typical fluorescence images of 20 µm x 20 µm with a resolution of 128 x 128 pixels and an integration time of 10 ms/pixel we estimate that the average exposure time for an area corresponding to the laser beam with a beam waist of 1 µm (diameter measured at the 1/e^2 intensity values) is approximately 320 ms. This analysis yields a negligible 0.01 % loss of fluorescence intensity.

4.3.3 Mechanism Dependent Bleach Intensity Function

BlIPP is based on photobleaching, which renders the dye molecule non-emissive after repeated absorption and emission cycles. In addition to the radiative process of emission, which typically occurs from the lowest excited singlet state, an excited molecule can also relax non-radiatively to the ground state or relax into a dark triplet state.[124, 125] While in the triplet state, aided by its longer lifetime, the molecule can undergo an irreversible reaction effectively turning off the fluorescence. In many cases it is singlet oxygen, which reacts with the photoexcited molecule in its triplet ground state. This photobleaching mechanism can be described by a 3-level system[122, 126] which requires the absorption of only one photon. However, at high excitation intensities it has been shown that a 5-level system[122, 127] or 2-photon photobleaching mechanism may dominate, where the molecule in the triplet state first absorbs a second photon before undergoing an irreversible chemical reaction, or the molecule may absorb a second photon while in the first excited state and then undergoes intersystem crossing from the excited singlet state to an excited triplet state, followed again by an irreversible chemical reaction. This 2-photon absorption brings the molecule to a more reactive higher energy triplet state, thereby increasing the likelihood of a photobleaching event to occur. The photobleaching rate constant, k_{bl}, therefore depends on the excitation intensity: in the case of a 1-photon process, $k_{bl} \propto I$, whereas for the 2-photon mechanism, $k_{bl} \propto I^2$.[119, 121] This difference in excitation intensity dependence of the photobleaching reaction may lead to an erroneous estimation of the propagation length in plasmonic waveguides using BlIPP. We show first how the type of photobleaching reaction leads to different propagation lengths by presenting in detail the derivation of the rate equation model used to fit the

photobleach intensity in Figure 4.1D and then experimentally determine whether photobleaching in our BlIPP measurements occurs via a 1- or 2-photon pathway.

Assuming a first order reaction, the fluorescence intensity, F, at time, t, can be expressed by Equation 4.1, where F_0 is the initial fluorescence intensity at time zero.

$$F(t) = F_0 \exp\left(-k_{bl} t\right) \qquad \textbf{Equation 4.1}$$

For a spatially varying excitation intensity, $I(x)$, with the direction along the plasmonic waveguide taken to be the x direction and considering first a one photon reaction, k_{bl} can be written as given by Equation 4.2.

$$k_{bl} = k_0 I\left(x\right) \qquad \textbf{Equation 4.2}$$

where k_0 represents the product of several intrinsic properties of the dye, including the composite microscopic rate constants of photobleaching from all possible excited states, the absorption cross section, and the radiative rate constant.[120, 122] Substituting Equation 4.2 into Equation 4.1 and rearranging Equation 4.1, we can write the ratio of fluorescence intensities at time t over the initial fluorescence intensity as a function of position x according to Equation 4.3.

$$\frac{F(t)}{F_0} = \exp\left(-k_0 \left(I_G\left(x\right) + I_{SPP}\left(x\right)\right) t\right) \qquad \textbf{Equation 4.3}$$

Here $I_G(x)$ is the spatial intensity distribution of the Gaussian laser beam with σ describing its width and centered at the point of excitation (x = 0), which corresponds to the center of the laser exciting the NW end, as given by Equation 4.4. $I_{spp}(x)$ is the spatial intensity distribution of the near-field of the propagating SP wave that can be described by a exponential decay curve with propagation length, L_0, according to Equation 4.5.

$$I_G\left(x\right) = I_{G,0} e^{\frac{-x^2}{2\sigma^2}} \qquad \textbf{Equation 4.4}$$

$$I_{SPP}(x) = I_{SPP,0} e^{\frac{-x}{L_0}}$$ **Equation 4.5**

$I_{G,0}$ and $I_{SPP,0}$ are the maximum intensities at $x = 0$. Upon substitution of Equation 4.4 and Equation 4.5 into Equation 4.3 we obtain Equation 4.6, which describes the fluorescence intensity normalized by the initial fluorescence intensity as a function of time, t, and position, x.

$$\frac{F(t)}{F_0} = \exp\left(-t \left(k_0 I_{G,0} e^{\frac{-x^2}{2\sigma^2}} + k_0 I_{SPP,0} e^{\frac{-x}{L_0}} \right) \right)$$ **Equation 4.6**

The photobleach intensity measured by BlIPP is then given by subtracting Equation 4.6 from the value of 1, the initial fluorescence intensity in this normalized equation. This yields Equation 4.7, which describes the intensity of fluorescence bleaching at time t and position x.

$$I_{bl}(x,t) = 1 - \exp\left(-t \left(k_0 I_{G,0} e^{\frac{-x^2}{2\sigma^2}} + k_0 I_{SPP,0} e^{\frac{-x}{L_0}} \right) \right)$$ **Equation 4.7**

Equation 4.7 well describes the BlIPP data as verified by performing time-dependent measurements.[26, 27] The propagation length, L_0, is then determined by fitting the width-averaged line-section of the photobleach intensity along the NW (x direction) to Equation 4.7 (see black line in Figure 4.1D). The coefficients, $k_0 I_{G,0}$ and $k_0 I_{SPP,0}$, are treated as variables, typically within a fairly narrow range of ~ 20% ($1.2 \times 10^{-3} \pm 2.2 \times 10^{-4}$ s^{-1} and $4.1 \times 10^{-4} \pm 0.8 \times 10^{-4}$ s^{-1}, respectively) to achieve the best agreement between the fit and the experimental data from NW to NW. Small variations can be explained by differences in the local film thickness, which is expected to lead to changes in $I_{G,0}$ as the intensity is modified by the absorption of individual and aggregated dye molecules, and considering the fact that the shape of the NW tips often varies, therefore affecting the coupling

efficiency between photons with the propagating plasmons and hence $I_{SPP,0}$. The width of the Gaussian laser profile, σ, was obtained separately by performing BlIPP experiments on dye coated glass coverslips where no NWs were present. In those experiments the bleach intensity line-section was described by only the Gaussian intensity profile of the laser resulting in values of σ = 1.5 ± 0.2 μm. In our fitting routine σ was then adjusted within this range of the experimental error. It should be noted that σ of the Gaussian intensity profile for the photobleaching was slightly larger than the excitation beam spot profile itself (see experimental section) because scattered light from the NW end and the glass substrate might also contribute to photobleaching of the dye.

Equation 4.7 follows from a 1-photon photobleaching mechanism, but as mentioned above, at higher excitation intensities 2-photon pathways are also possible.[122] Instead of Equation 4.2 we now have to consider that the photobleaching rate constant depends on the square of the excitation intensity according to Equation 4.8, which then results in Equation 4.9 and Equation 4.10 following the same derivation as outlined above for Equation 4.7.

$$k_{bl} = k_0 I^2(x) \qquad \textbf{..Equation 4.8}$$

$$\frac{F(x)}{F_0} = \exp\left(-k_0 \left(I_G(x) + I_{spp}(x)\right)^2 t\right) \qquad \textbf{Equation 4.9}$$

$$I_{bl}(x,t) = 1 - \exp\left(-k_0 t \left(I_{G,0}^2 e^{\left(\frac{-x^2}{\sigma^2}\right)} + 2I_{G,0} I_{SPP,0} e^{\left(\frac{-x^2}{2\sigma^2} + \frac{-x}{L_0}\right)} + I_{SPP,0}^2 e^{\left(\frac{-x}{\left(\frac{L_0}{2}\right)}\right)}\right)\right) \qquad \textbf{Equation 4.10}$$

Away from the point of laser excitation (large x values) the first two terms in Equation 4.10 become very small so that the contribution from the SP intensity dominates the bleaching intensity. Equation 4.10 can hence be simplified as given by Equation 4.11.

$$I_{bl,\ \text{large x}}(x,t) = 1 - \exp\left(-t\left(k_0 I_{SPP,0}^2 e^{\left(\frac{-x}{\left(\frac{L_0}{2}\right)}\right)}\right)\right) \qquad \textbf{Equation 4.11}$$

The difference between Equation 4.7 and Equation 4.11 is the factor of 2 in the denominator of the exponential, which means that, if a 2-photon process dominates the photobleaching mechanism in a BlIPP measurement, the true propagation length of the plasmonic waveguide would be twice of the value that is obtained with Equation 4.7. It is therefore important to experimentally verify if the primary photobleaching mechanism in BlIPP occurs via a 1- or 2-photon process. We therefore measured the photobleaching rate constant, k_{bl}, as a function of excitation intensity both on single Au NWs and on areas on the glass coverslip where only dye molecules were present.

4.4 Results and discussion

To measure k_{bl} for the dye photobleaching on the Au NW we positioned the stage such that the laser was focused onto a single NW. The middle region of an Au NW was chosen to minimize the effect of enhanced scattering at the NW tips while still probing the dye fluorescence enhanced by the metal. The integrated fluorescence intensity for the chosen sample position was measured with a single element avalanche photo-diode detector as a function of time using a photon counting board set to a time resolution of 5 ms and a total acquisition time of 5 minutes. This experiment was repeated for different

Au NWs and different excitation intensities, which were comparable to the values used for BlIPP. The same measurements were then carried out under identical conditions with the sample positioned so that the laser excited a background area where no Au NW was present, but where strong fluorescence from the continuous dye film could be observed.

The fluorescence images in Figures 4.3A and 4.3B illustrate these experiments by showing a sample area with a Au NW before and after localized photobleaching was performed on top of the NW as well as next to it. Figure 4.3C shows a typical example of a fluorescence transient recorded on top of a Au NW with an excitation intensity of 1.2 kW/cm^2. The decrease in the fluorescence intensity with time is due to laser induced photobleaching.

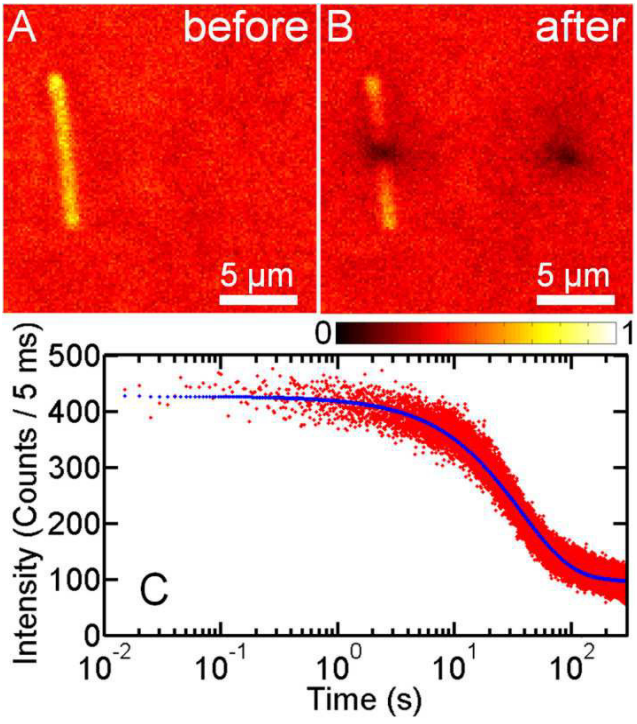

Figure 4.3 (A) Fluorescence image of a 20 µm x 20 µm area containing a Au NW acquired with a low excitation intensity of 7.8 W/cm^2 **(B)** Fluorescence image of the same area recorded after measuring k_{bl} in the middle of the NW and in a background area to the right of the NW at a laser intensity of 1.2 kW/cm^2. **(C)** Fluorescence intensity observed on top of a Au NW as a function of time. The laser excitation intensity was 1.2 kW/cm^2 at 785 nm. The experimental data is shown in red and a biexponential fit with decay constants of $k_1 = 3.1 \times 10^{-2}$ s^{-1} and $k_2 = 2.7 \times 10^{-3}$ s^{-1} is given by the blue line. k_1 is assigned to k_{bl}.

Each fluorescence transient as the one shown in Figure 4.3C was best described by a biexponential decay instead of the monoexponential behavior given by Equation 4.1.[120] We assign the fast component, k_1, of the fitted biexponential curve to the photobleaching rate constant of the dye, k_{bl}. The 5 ms bin time did not allow us to resolve fast photoblinking events from single molecules, which would have also been averaged out by the high dye concentration of the film.[120, 128, 129] The second slow photobleaching component, k_2, originates from the spatially non-uniform Gaussian excitation beam. In a theoretical treatment, Berglund[130] has shown that photobleaching by an excitation source with a spatially varying intensity profile such as a Gaussian laser beam follows a non-exponential behavior independent of the underlying mechanism (1- vs. 2-photon), but can be described by a sum of exponential decay functions. For the present case, we have chosen the simplest version of a sum of two exponential decays, where the fast component represents the photobleaching of the dye molecules in close proximity to the Gaussian beam center, while the slow component corresponds to photobleaching of the dye molecules at the edges of the laser spot where the excitation intensity is much lower. This approach is consistent with the fact that in these experiments with the single element detector without scanning the sample, no spatial information was obtained as with the BlIPP measurements. The spatially integrated signal was chosen because we were able to acquire the fluorescence transients with a higher time resolution compared to imaging. Another explanation for the non-exponential decay of the fluorescence intensity in Figure 4.3C is that non-uniformities in the dye concentration of the thin film may also lead to heterogeneities in the observed photobleaching dynamics, as reported previously.[131, 132]

The assignment of k_1 to k_{bl} is furthermore consistent with the observation that the decay times fitted for the slow component, k_2, varied randomly within the range of 8-20 minutes.

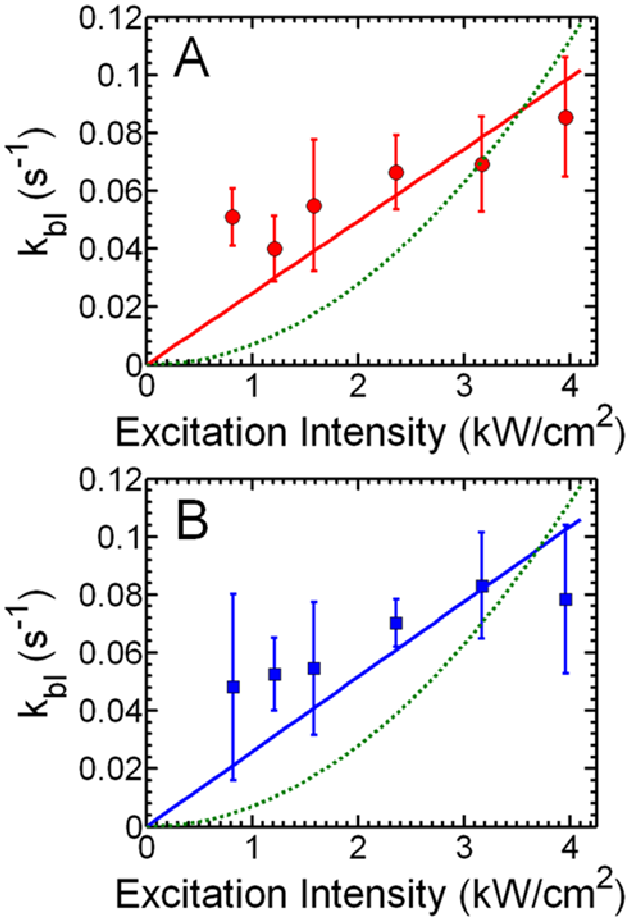

Figure 4.4 Intensity dependence of the photobleaching rate constant k_{bl}. **(A)** Dependence of k_{bl} on the excitation intensity measured for the plasmon enhanced fluorescence on top of Au NWs. **(B)** Same as (A) but measured in the background near the Au NWs, where the dye is deposited only on glass. k_{bl} was obtained as the first component of a biexponential fit to time transients such as the one shown in Figure 4.3C. The solid lines in (A) and (B) are linear fits to the data points based on Equation 4.2. For each intensity, the measurements were repeated at least 8 times and the error bars represent the standard deviation. The variation in the values for k_{bl} are likely due to local difference in the dye film. The solid lines in (A) and (B) are linear fits to the data points based on Equation 4.2, while the dashed lines correspond to fits according to a quadratic intensity dependence according to Equation 4.8.

A linear relationship of k_{bl} with excitation intensity verifies a 1-photon photobleaching mechanism of BlIPP for this system of plasmonic waveguide and dye. Figures 4.4A and 4.4B summarize the values of k_{bl} obtained for all experiments carried out on top of the Au NWs (4.4A) and for the dye film only (4.4B) as a function of

excitation intensity. The error bars were calculated as the standard deviation from at least 8 measurements on 7 independent samples. The trends in Figures 4.4A and 4.4B show a linear relationship in agreement with Equation 4.2, establishing that the photobleaching mechanism of the ICG dye film used in these BlIPP studies is based on a 1-photon process. Fits associated with the 2-photon photobleaching mechanism (Equation 4.8) are given in Figure 4.4 as shown by the green dashed line, and fail to describe the experimental data. Furthermore, the slopes of the linear fits in Figures 4.4A and 4.4B are identical within the error bounds at a value of 2.5×10^{-2} $(s^{-1})/(kW/cm^2)$. This last conclusion indicates that, while the fluorescence is enhanced over the Au NWs, coupling between the dye molecules and the plasmonic near-field has no or little effect on the photobleaching rate constant, k_{bl}, and hence the chemical reaction causing the photobleaching.

Further experimental verification of the 1-photon photobleaching mechanism was obtained by comparing BlIPP experiments carried out for different Au NWs as a function of excitation intensity. Using the bleach intensity recorded by BlIPP instead of direct laser excitation measurements as in Figures 4.3 and 4.4 allows for the observation of the intensity dependent photobleaching due to the indirect excitation of the dye molecules via the propagating SP near-field. Figure 4.5A shows the width-averaged line-sections from the difference images of three different Au NWs measured by BlIPP at 0.6 kW/cm^2, 3.5 kW/cm^2, and 7.8 kW/cm^2. This comparison is important because photobleaching by the plasmonic near-field occurs on much slower time scales compared to direct laser excitation and it was difficult to access such a low excitation intensity regime in Figure 4.4 with direct laser excitation as the measurement noise increased dramatically with

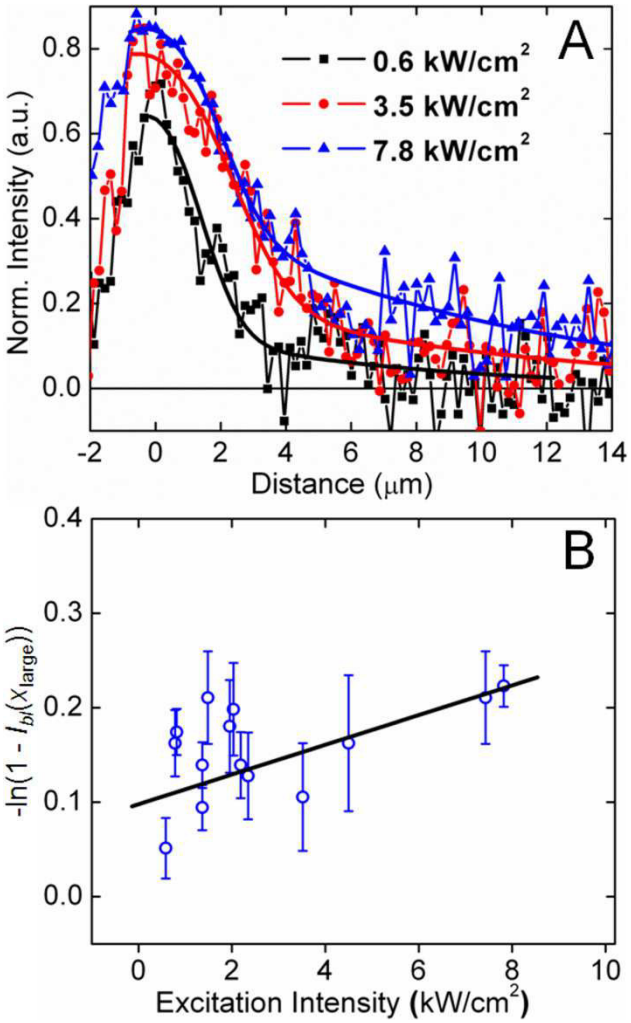

Figure 4.5 Intensity dependence of BlIPP at exposure time, t = 20 min. **(A)** Width-averaged bleach intensity line-sections along the long NW axis as extracted from the difference images for 3 different Au NWs exposed to laser intensities of 0.6 kW/cm^2, 3.5 kW/cm^2 and 7.8 kW/cm^2 with fits (lines) according to Equation 4.7. **(B)** Laser excitation intensity dependence of the bleach intensity according to Equation 4.13 measured for Au NWs excited with a 785 nm laser at x_{large} = 8.5 μm away from the NW tip that was exposed during the BlIPP measurements. Each data point was measured for a different Au NW and extracted from the corresponding width-averaged bleach intensity line-section, such as those shown in (A). The error bars were estimated from individual BlIPP traces, by calculating the average deviation of ± 3 data points from the central data point.

lower laser intensities. The bleach intensity line-sections in Figure 4.5A demonstrate that an increase in the excitation intensity increases the total bleach intensity signal along each Au NW. For the first 3 μm closest to the point of laser excitation it appears that the two higher excitation intensities have caused saturation of the photobleach intensity. Photobleaching in this region is dominated by direct photobleaching by the incident laser,

whereas photobleaching far from the point of excitation along the NW is most indicative of the excitation intensity dependent coupling and bleaching of the dye molecules by the near-field of the propagating plasmon modes.

To quantitatively analyze the excitation intensity dependence of the BlIPP signal in Figure 4.5A, we first rewrite Equation 4.7 according to Equation 4.12 to demonstrate the exponential relationship of the photobleach intensity I_{bl} with the excitation intensity at a given position, x, along the NW.

$$-\ln\left(1-I_{bl}\left(x,t\right)\right)=tk_0\left(I_G\left(x\right)+I_{SPP}\left(x\right)\right) \qquad \textbf{Equation 4.12}$$

In Figure 4.5B, we therefore plot $-\ln(1-I_{bl}(x,t))$ at a given exposure time, t = 20 min, and at a large distance of x_{large} = 8.5 μm away from the excited NW tip as a function of laser excitation intensity, where we assume that I_{SPP} is directly proportional to the laser intensity. At distances far from the point of excitation, the contribution of the Gaussian excitation beam approaches zero, which means that Equation 4.12 can be further simplified as given by Equation 4.13.

$$-\ln\left(1-I_{bl}\left(x_{\text{large}},t\right)\right)=tk_0\left(I_{SPP}\left(x_{\text{large}}\right)\right) \qquad \textbf{Equation 4.13}$$

The data shown in Figure 4.5B was collected from 15 NWs. The spread in measured values is likely due to the fact that each measurement at a different excitation intensity had to be carried out on another NW with a slightly different tip geometry and width, which both influence the coupling efficiency of the excitation light to the propagating SP modes and hence cause variations in I_{SPP}. Nevertheless, the dependence of the dye photobleaching on the intensity of the SP near-field follows the linear trend given by Equation 4.13, i.e. $-\ln(1-I_{bl}(x,t))$ linearly depends on $I_{SPP}(x)$, rather than a quadratic relationship scaling with $(I_{SPP}(x))^2$. Bleach intensities were furthermore evaluated at x = 5

μm and x = 10 μm as shown in Figure 4.6, and the same linear dependence as in the case of x = 8.5 μm is observed. These results indicate that both direct excitation of the dye by the laser and indirect excitation by the near-field of the propagating plasmon follow a 1-photon photobleaching mechanism.

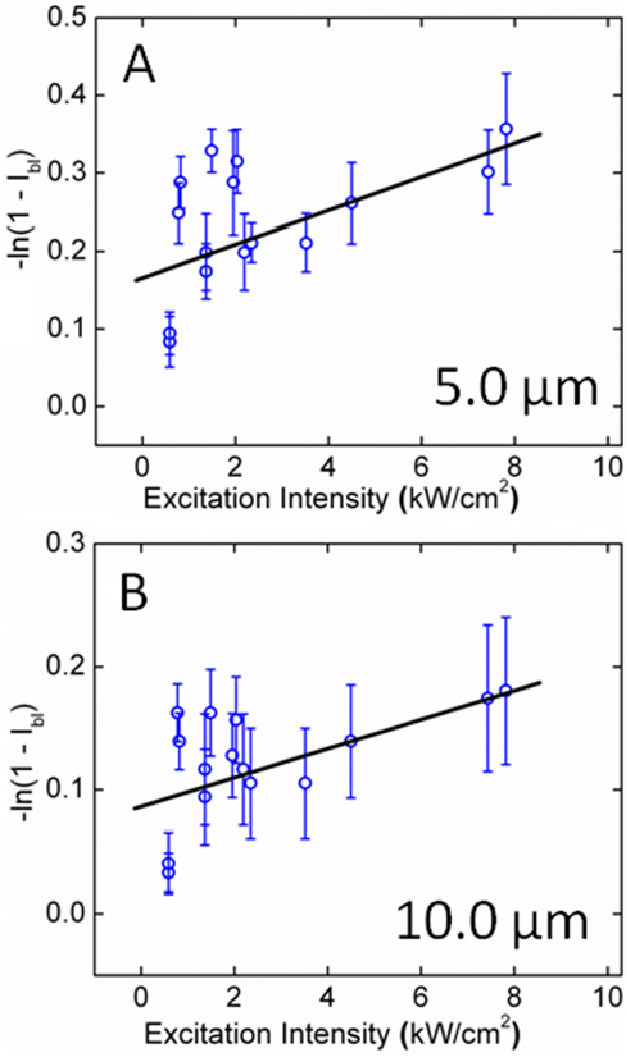

Figure 4.6 Laser excitation intensity dependence of the bleach intensity according to Equation 4.13 measured for Au NWs excited with a 785 nm laser at (A) x_{large} = 5.0 μm (B) x_{large} = 10.0 μm away from the NW tip that was exposed during the BlIPP measurements. Each data point was measured for a different Au NW and extracted from the corresponding width-averaged bleach intensity line-section. The error bars were estimated from individual BlIPP traces, by calculating the average deviation of ± 3 data points from the central data point.

4.5 Conclusion

In conclusion, we have investigated the excitation intensity dependence of the photobleaching reaction that gives rise to the signal in BlIPP. Our experimental results show that photobleaching of the dye ICG coated over Au NWs occurs via a 1-photon photobleaching mechanism. It is important to establish the dye photobleaching mechanism, as the kinetic model developed for BlIPP predicts that a 2-photon process would lead to a propagation length that is larger by a factor of 2. Our results also show that the coupling between the dye molecules and the plasmonic near-field has no or little effect on the chemical reaction responsible for the photobleaching. Furthermore, it is worth pointing out that with the values determined for the photobleaching rate constant, k_{bl}, under the conditions evaluated here for ICG molecules, it should be possible to extract from the fitting values the initial intensity of the excited SP modes at the NW tip, $I_{SPP,0}$. This means that with further careful BlIPP studies, NW in-coupling efficiencies may be experimentally determined. This will be further tested with NWs having different tip geometries.

4.6 Acknowledgements

This work was funded by the Robert A. Welch Foundation (C-1664), the Office of Naval Research (N00014-10-1-0989), and NSF (CHE-0955286). DS was supported by an NSF Graduate Research Fellowship (Grant No. 0940902). We thank Professor Eugene Zubarev and Leonid Vigderman for supplying the Au NW sample used in these studies.

CHAPTER 5

TURNING THE CORNER: EFFICIENT ENERGY TRANSFER ALONG BENT CHAIN WAVEGUIDES[4]

5.1 Abstract

Application of plasmonic waveguiding components such as NWs, grooves, and stripes onto small scale optical circuit chips has remained a difficult problem in the field of plasmonics. Recently closely packed metallic chain structures made of small NPs has demonstrated excellent waveguiding properties with the added benefit of being created with precise control over chain geometry by using electron beam lithography to define the chain structures. In this work we use the BlIPP method to observe the efficient transfer of energy along Ag NP (AgNP) chain waveguides over long distances along straight waveguides and around sharp 90º corners via coupling of light to subradiant propagating modes when excited at 633 nm. Straight and bent chain structures made of closely packed 54 ± 5 nm AgNPs were studied with BlIPP to measure a propagation length for both straight and bent structures of 8.0 ± 0.7 μm and 8.0 ± 0.4 μm respectively with no significant bending losses around the corner in the case of the bent waveguides. Polarization dependent BlIPP studies also revealed an insensitivity of plasmon propagation along straight and bent chains to incident polarization.

[4] This chapter is based on the manuscript titled "Turning the Corner: Efficient Energy Transfer Along Bent Chain Waveguides" by David Solis Jr., Aniruddha Paul, Jana Olson, Liane S. Slaughter, Pattanawit Swanglap, and Stephan Link, and is a manuscript in progress to be submitted.

5.2 Introduction

A growing need to transfer information at high speeds and subdiffraction length scales has fueled the development of many novel optical waveguide structures.[1, 9, 18, 35, 48, 133-135] Metallic NWs,[11, 25, 26, 28, 37, 38, 40, 58, 136] stripes,[54, 79, 137] and patterned thin films such as grooves in a metal[24, 45] have been studied for their ability to couple light to coherent waves of electrons, known as SPPs.[9, 12, 31] Energy losses due to interband transitions within plasmonic materials,[118, 138] radiative leakage at lattice imperfections or breaks in the geometry of a waveguide,[38, 42, 46, 47, 113] as well as inefficient light input and output coupling lead to reduced plasmon propagation distances.[36, 39, 59] An effort to reduce such decay channels has remained a priority in achieving lossless plasmonic energy transfer along straight metallic waveguides. In addition to propagating energy efficiently along straight waveguides, in plasmonic circuit applications, it will be necessary to guide energy around complex structures such as bends and splits. In the case of waveguiding along bent structures another energy loss mechanism due to the momentum mismatch at the bend leads to an added attenuation factor to the SPP intensity, known as the bending loss. [45, 139]

Typically in bent NWs and grooves, the bend must be gradual to avoid creating a sudden change in the SPP momentum which would lead to the emission of photons and is typically designed with an arc corresponding to the curvurture radius of a circle.[139-141] In NWs which use kinks to achieve a bent structure, light has been observed emitting from the kink as in the case of antenna sites.[139] Both forms of radiative energy losses at a bend in a NW have been described as bending losses which increase the attenuation of the SPP without changing the intrinsic plasmon propagation length of the waveguide.[45, 139] For

previous studies bending losses of nearly 5 dB for a curvature radius as large as 30 μm for NWs at 785 nm[139] and nearly 3 dB for a curvature radius of 0.83 μm for S shaped V groove patterns at longer wavelengths of 1425 nm[45] or a 1.9 dB bend loss in the case of a 90° sharp bend in Au stripe have been reported.[54] These studies show that in the case of a straight waveguide the SPP signal would be much more intense than the SPP signal at the end of a waveguide with added bending losses.

Recently, closely packed NP chains with small gaps of ~ 1-5 nm, have demonstrated plasmonic waveguiding properties similar to NWs.[29, 30] These structures, created by using a top down method via the use of e-beam lithography for trench pattern creation are assembled through deposition of NPs from solution into the trenches under normal lab conditions. This method of sample preparation allows for the creation of complex waveguide designs without the need for micromanipulators[48] or optical trapping[52, 53] to bring each waveguide into position on a substrate one structure at a time. In previous work,[29] plasmon propagation lengths for AuNP chains were measured to be 3.9 ± 0.6 μm with the use of BlIPP.[26, 27, 29, 44] In these closely packed chain structures subradiant propagating modes were formed, allowing energy to transfer from particle to particle with suppressed radiative energy losses over long distances. This particle to particle mechanism of energy transfer in chain structures was further believed to have beneficial properties in efficient energy transfer around bent structures,[31] however, only straight chains were studied to verify the long distance plasmon propagation possible in tightly packed chain structures.

In this work, we report on the highly efficient transfer of energy around chains of spherical Ag NPs with a sharp 90º bend via coupling to the sub-radiant response of the

waveguide at an excitation wavelength of 633 nm. In comparison to straight AgNP chains of similar size we observe no strong evidence of bending losses in the case of bent chains and using BlIPP we measure propagation lengths of 8.0 ± 0.4 μm for the bent structures and 8.0 ± 0.7 μm for the straight structures. We further verify that these long propagation lengths occur when coupling light to subradiant propagating modes of the chain structure through the use of extinction spectroscopy, dark field-scattering spectroscopy and comparison of BlIPP measurements for 785 nm excitation. For 785 nm, the propagation length is shortened drastically due to the coupling of light to super-radiant modes of the chain, where radiative energy losses are dominant.

5.3 Experimental

5.3.1 Materials and Sample Preparation

The AgNP chain structures were made by first creating trench patterns into a polymer resist film using e-beam lithography. In preparation for lithography, the indium tin oxide (ITO) glass substrate (8-12 ohms, Delta technologies) was first cleaned by sonicating the slide for 20 min in a 1:4:20 ammonium hydroxide, hydrogen peroxide, and water mixture, then sonicating in deionized water twice for 10 min, followed by plasma cleaning (Harrick Plasma). The ITO slide was then coated with a thin film of photoresist, poly(methyl methacrylate) (PMMA) from a 4% 495 kg/mol PMMA in anisole solution (MicroChem).

Electron beam lithography (JEOL 6500) was then used to cut an array of 15 μm x 200 nm rectangular trenches and 90 degree "L" shaped rectangular structures of 200 nm in width and side lengths of 7.5 μm into the photoresist. The trenches were developed in

methyl isobutyl ketone in isopropanal (MIBK) (Sigma-Aldrich) solution for 25 s followed by a stop bath of isopropanal.

After lithography was completed the trenches were then filled by drop casting 10 uL of citrate capped 54 ± 5 nm spherical AgNP (Ted Pella, PELCO NanoXact) in solution onto the center of the trench array and allowing the droplet to dry in air at a slight angle of 10-20 degrees. As the droplet evaporated AgNP filled into the trenches leaving close-packed AgNP chain structures surrounded by PMMA film. The sample was then inspected with a combination of dark-field and bright-field microscopy to determine the quality of trench filling. In many samples 2-3 such depositions were necessary to achieve a significant number of well filled trenches. The polymer surrounding newly formed AgNP chains was then lifted off by dipping the sample into a beaker of acetone with slight agitation (gentle stirring of the sample in acetone) for 10 s and drying the sample with a gentle nitrogen gas stream. A second rinse of the polymer was then performed by placing the beaker of acetone into a sonicator and dipping the sample into the beaker for periods of no more that 1 s at a time for up to 5 s total (10 s total as the maximum in order to avoid loss of particles from the formed chains).

Scanning electron microscopy (SEM) was then used to screen the free standing AgNP chain samples at low magnification and to locate unbroken close-packed chains which would be used for optical measurements later. Examples of the free standing straight and bent chain structures can be seen in Figures 5.1A and 5.1F, respectively. These SEM images were taken after the BlIPP experiments were completed to further avoid the possibility of melting from e-beam exposure during high magnification imaging. For BlIPP measurements, the samples were then coated with a dye film. For 633 nm

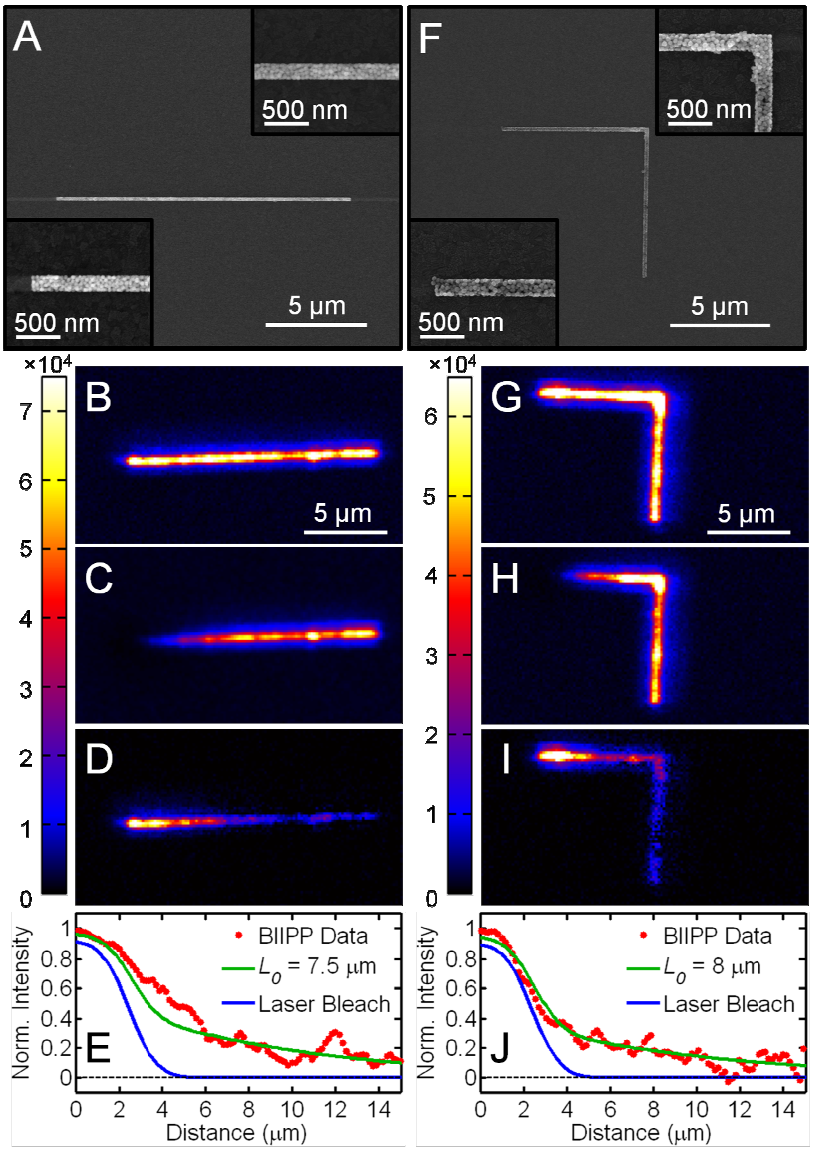

Figure 5.1 SEM and 633 nm BlIPP data for AgNP straight and bent chains. **(A)** SEM of the 15 µm by 200 nm straight chain structure taken after the BlIPP experiment. Insets show high resolution images of the end excited during BlIPP, bottom left, and an area from the middle section of the chain, upper right. **(B)** Fluorescence image taken at a power of 27 nW of the straight chain structure shown in A before the bleach exposure. **(C)** Fluorescence image taken at 27 nW after 20 min photobleach exposure at 12.0 µW. **(D)** Difference fluorescence image created by subtracting the after exposure image, C, from the initial image, A. **(E)** The width averaged line section from the region over the chain structure in D is shown by the BlIPP data in red. BlIPP fitting of the linesection data is shown in green and yields a propagation length of L_0= 7.5 µm. The contribution of photobleaching due to direct laser excitation is shown by the laser bleach data shown in blue. **(F)** SEM image of a bent AgNP chain taken after the BlIPP experiment is shown and the insets show high resolution images of the point of excitation, bottom left, and at the bend of the chain, upper right. **(G)** Fluorescence image taken at 36 nW before photobleaching. **(H)** Fluorescence image taken at 36 nW after photobleaching the structure at 12.0 µW for 20 min. **(I)** Difference image created by subtracting image H from image G. **(J)** Shows the width averaged line section of the difference image (red), BlIPP fitting of the width average line section data (L_0 = 8.0 µm, green), and the contribution of the laser bleach spot (blue).

excitation experiments the sample was spin coated with 60 μL of 0.2 mg/mL solution of LDS821 dye (Exciton) in methanol at 6000x RPM for 40 s. In the case of 785 nm excitation the sample was spin coated with 30 μL of 0.1 mg/mL solution of Cardiogreen (Sigma-Aldrich) in methanol at 6000x RPM for 40 s.

The sample was then loaded onto an XYZ piezo stage (Physik Instrumente) mounted on a fluorescence confocal microscope (Zeiss Axiovert 200). The laser excitation source was then directed into the microscope and focused onto the dye coated chain sample by a 50× Zeiss air space objective (NA 0.8). Two lasers were used in these studies, a 633 nm He-Ne laser (JDSU) and a 785 nm diode laser (Power Technology Inc.). Fluorescence from the dye was then captured by the objective and directed and focused onto an avalanche photodiode detector (APD, Perkin Elmer SPCM-AQR-15). Raster scanning of the sample was then performed to assemble a fluorescence image of the sample as shown in Figure 5.1B and 5.1G with the use of imaging software (XPM Pro) and an RHK Technology piezo stage controller (SPM 100).

5.3.2 BlIPP Experimental Overview

The BlIPP method was performed by first taking an initial fluorescence image of the region of interest on a particular chain structure, Figure 5.1B and 5.1G. The piezo stage was then positioned in such a way that the laser was focused directly above the end of the chain structure. The laser power was then increased from the image scanning power in the range of 27 - 42 nW, to a bleaching power in the range of 12.0 - 12.6 μW for an exposure period of 5 min. After the exposure time, the power was decreased back to the scanning power and a second image was taken. This bleaching procedure was

performed 3 more times, which finally gave us the image shown in Figures 5.1C and 5.1H which were taken after 20 minutes of total exposure to the bleaching laser. The four step bleaching process was used in order to fit the propagation length of the BlIPP curve with the evolution of photobleaching over time. During the high power bleaching exposure at the end of the chain structure, laser light was coupled to propagating plasmons which created a near-field intensity that decayed exponentially from the point of excitation. Over time, interaction between the plasmonic near-field and the fluorescent dye above the structure lead to irreversible photobleaching.[44] This photobleaching resulted in the significant loss of fluorescence intensity along the waveguide after each exposure, which can be seen in the after exposure image shown in Figures 5.1C and 5.1H.

To highlight photobleaching along the NP chain due to the propagating SP a difference image was created by subtracting the after exposure image from the initial image before exposure, shown in Figures 5.1D and 5.1I. A width averaged line section was then taken from the area over the chain as shown by the red dotted data set in Figures 5.1E. Acquiring the line section from the bent structure as shown in Figure 5.1J was done by first cutting and rotating the region of the chain after the corner, then stitching the images together and proceeding with the width averaged linesection as in the case of straight NP chains. The BlIPP equation was then used to fit the linesection data and determine the propagation length of the SP.[44] The fitting analysis was performed with Matlab. Sigma values to describe the Gaussian beam profile of the excitation laser used in the fitting equation were found experimentally by performing the BlIPP experiment on dye coated glass slides. $\sigma_{633nm} = 1.5 \pm 0.1$ μm and $\sigma_{785nm} = 1.5 \pm 0.2$ μm were used.

5.4 Results and discussion

Using BlIPP to characterize the propagation length for close-packed AgNP straight chains, we measured a propagation length of 8.0 ± 0.7 μm, substantially larger than the propagation length reported for AuNP chains previously.[29] Further, study of plasmon propagation along chains with the same width, length, and materials but that incorporates a sharp 90º bend at the midpoint of the chain as shown in Figure 5.1F, revealed that the propagation length does not change, with a measured propagation length of 8.0 ± 0.4 μm. Analysis of the linesection of the difference image for the bent structure, Figure 5.1I, also demonstrates that at the point of the bend, 7.5 μm along the chain, there is no significant drop in bleaching intensity. The fact that the bleach intensity does not drop at the bend and the propagation length does not change for bent structures demonstrates that plasmon propagation around this sharp bend does not suffer bending losses, unlike in other bent waveguide structures.[45, 139] Recently, work by Hasegawa et al.[142] demonstrated theoretically that large radiative losses of the SPP at an infinitely sharp corner of a waveguide reduced by embedding a small SPP microresonator such as a spherical NP which creates an alternative transmission channel for the SPP to couple thereby mitigating energy losses at the corner, which ultimately increases the propagation efficiency of the SPP around the corner, reported transmission coefficient increased from .07 to .17 with the addition of 1 NP.[142] The efficient and low bend loss propagation of the SPP in bent chain structures is attributed to a similar effect though on a much larger scale as in the chain structure the bend region is composed of nearly 60 AgNPs in 3 dimensions each of which transfers energy to its neighbors in all directions via sub-

radiant collective modes thereby opening several alternative non-radiative transfer channels to propagate the SPP efficiently around the sharp corner.

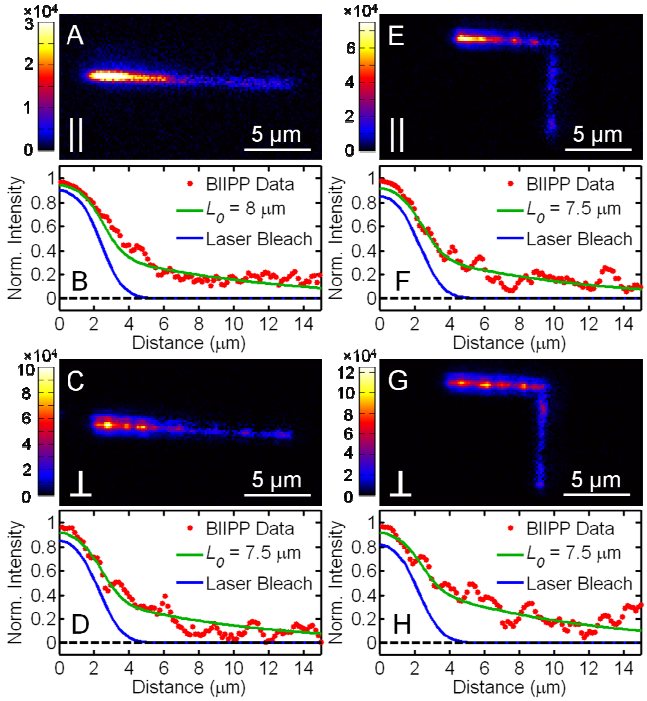

Figure 5.2 AgNP chain excitation polarization dependence. **(A)** BIIPP difference image after 20 min bleaching exposure of 12.2 μW parallel polarized 633 nm light for a straight chain. The fluorescence image taken at 42 nW. **(B)** The width averaged line section from the region over the chain shown in A is shown in red along with the BIIPP fit (green) with a propagation length of L_0 = 8.0 μm and the curve showing the component of bleaching associated with direct laser excitation (blue). **(C)** and **(D)** show similar data sets as A and B for a straight AgNP chain excited with perpendicularly polarized light after 20 min exposure at 12.1 μW (fluorescence image taken at 39 nW). **(E)** and **(F)** show similar data to A and B for a bent chain excited with parallel polarized light after 20 min exposure at 12.2 μW, (fluorescence image taken at 42 nW). **(G)** and **(H)** show similar data to A and B for a bent chain excited with perpendicularly polarized light after 20 min exposure at 12.1 μW (fluorescence image taken at 39 nW).

Polarization dependent studies were also carried out on the AgNP straight and bent chains as shown in Figure 5.2. Previous studies with nanowire waveguides have demonstrated control of output intensity with incident polarization.[48, 59, 115] For parallel excitation we measure propagation lengths of 8.2 ± 0.3 μm and 7.7 ± 0.3 μm for straight and bent chains respectively. Under perpendicular excitation at the same power and for the same exposure period we measure propagation lengths of and 7.7 ± 0.3 μm and 7.7 ± 0.6 μm for straight and bent chains respectively. We find from these studies that no

significant differences in propagation length and bleaching intensity were observed for polarized excitation consistent with studies indicating that plasmon propagation along chain structures is independent of polarization for straight structures.[29] We also find that propagation of energy around the sharp corner is also unaffected by excitation polarization. Again, the 3 dimensional coupling of disordered tightly packed AgNPs in the chain is believed to cause an overall mixing of any polarization dependence shortly after coupling to the waveguide.

Extinction spectra of the AgNP chains as shown in Figure 5.3A revealed a peak at 734 nm which corresponds to enhanced scattering at the super radiant mode as indicated by the dark field scattering spectra taken in the same region as shown in the inset of Figure 5.3A. From this scattering spectra, we also confirm that the scattering intensity is much larger at 785 nm than at 633 nm for the structure, signifying that at 633 nm radiative losses are strongly suppressed whereas at 785 nm excitation radiative losses are dominant. By exciting at a blue shifted wavelength, 633 nm, from the super-radiant response at 734 nm we were able to suppress radiative losses by coupling to the chain's band of sub-radiant modes.[30] This assignment was further verified by BlIPP measurements of AgNP straight chains at energies which were red-shifted from the extinction peak. BlIPP measurement at 785 nm yielded a propagation length of only 3.6 μm as shown in Figures 5.3B and 5.3C. The radiative energy losses associated with the coupling of light to super-radiant modes at an excitation wavelength of 785 nm resulted in a significant reduction of the plasmon propagation length and may be avoided by choosing an excitation wavelength blue shifted from the maximum extinction and which lies in the sub-radiant bandwidth of NP chains, such as excitation at 633 nm .

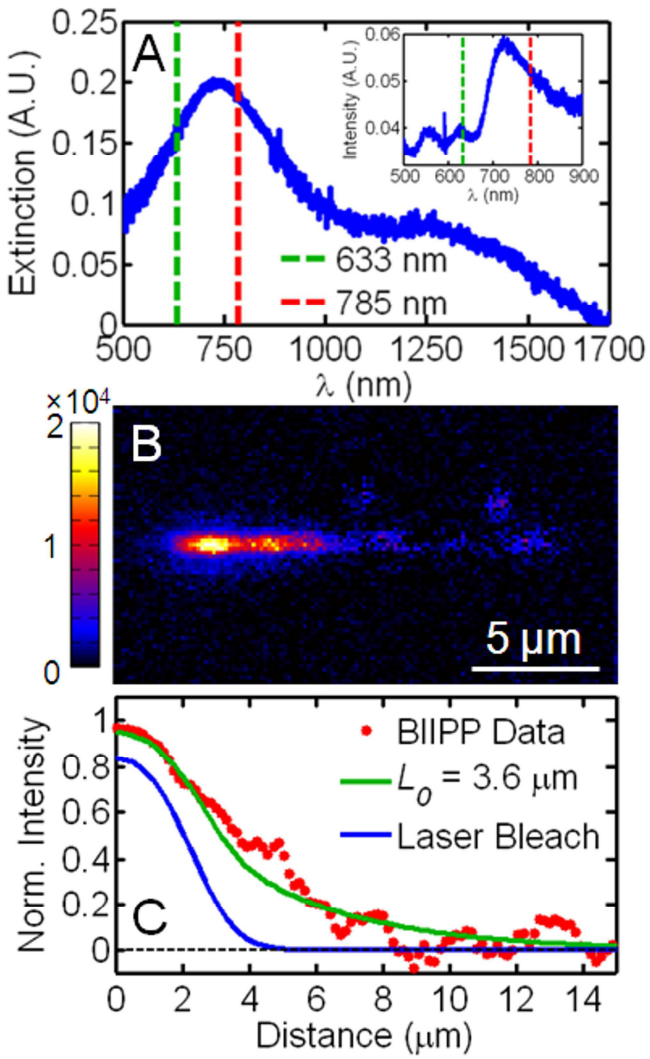

Figure 5.3 (A) Extinction spectra of the AgNP chain structure with peak at 734 nm. Excitation wavelength of 633 nm and 785 nm are shown in green and red respectively. The inset shows scattering spectra taken at the same location as the extinction spectra. **(B)** 785 nm excitation BlIPP difference image of the AgNP chain after bleaching for 20 min. at a bleach power of 12.6 μW. **(C)** Width average line section BlIPP data at 785 nm excitation is shown in red. The BlIPP fit in green yields a propagation length of L_0 = 3.6 μm. The blue line shows the photobleaching associated with direct excitation from the laser beam.

In our previous BlIPP study of sub-radiant SPP propagation in AuNP chains at an excitation wavelength of 785 nm a propagation length of 3.9 ± 0.6 μm was measured.[29] In this study we find that at an excitation wavelength of 633 nm we are able to couple to sub-radiant modes, where we measure a propagation length of 8.0 ± .7 μm for straight AgNP chains, nearly double the propagation length of the AuNP chains of the first study

which we attribute to low damping losses in the visible for AgNPs in comparison to AuNPs. Further, no significant differences in propagation length for different excitation polarizations were observed for both the AuNP and AgNP chain studies.

In light of previous AgNW[26, 40] studies we find that the propagation length measured for the AgNP bent and straight structures when excited in the sub-radiant band is on average similar, though slightly less, than the propagation length measured in other work, 11.3 μm[58] at 650 nm excitation for 100 nm AgNW, 10 ± 0.4 μm[115] at 628 nm excitation for 100 nm AgNW, 11.6 μm[47] for 200 nm wide AgNW, and 10 μm[40] for AgNWs of approximately 100 nm in diameter. At 633 nm excitation of AgNW we might expect a decrease in the propagation length which would make the propagation length of AgNP chains longer than AgNWs, because the propagation length of NWs is dependent on the diameter of the waveguide as well, which would increase the propagation length of AgNWs substantially when the diameter is doubled[26, 28, 40] to the same width as the AgNP chains, 200 nm.

5.5 Conclusions

In conclusion, sub-radiant SPP modes of AgNP chains exhibited long SPP propagation for straight and bent chains, i.e. $L_{0,straight}$ = 8.0 ± .7 μm and $L_{0,bent}$ = 8.0 ± .4 μm, with minimized radiative losses at sharp 90º corners as compared to straight AgNP chains of the same dimensions. Parallel and perpendicular polarization excitation studies at 633 nm demonstrated insensitivity of plasmon propagation in the chain system to incident polarization due to the nature of the interparticle energy transfer of these close-packed chain structures. Extinction and scattering spectra verified the subradiant nature

of long plasmon propagation in these chain waveguides. BlIPP measurement at an excitation wavelength of 785 nm, yielded a short propagation length of 3.6 μm which is consistent with radiative losses attributed to super-radiant modes. The unique ability of closely packed NP chains to propagate energy across long distances via sub-radiant modes also allows for lossless energy transfer around sharp corners and brings the concept of designed plasmonic circuits one step closer to reality. In future studies it will be interesting to study the energy splitting in "Y" or "T" shaped NP chain structures,[31] the use of high aspect ratio metallic nanorods to make the chains,[143] and investigation of the subradiant mode bandwidth tunability in chains of spherical NP shells[144].

5.5 Acknowledgements

This work was funded by the Robert A. Welch Foundation (C-1664), the Office of Naval Research (N00014-10-1-0989), and NSF (CHE-0955286). DS and JO were supported by an NSF Graduate Research Fellowship Grant No. (0940902) and PS acknowledges support from the Royal Thai Government. We thank Dr. Wei-Shun Chang and Dr. Britain Willingham for helpful discussion in preparation of this manuscript.

CHAPTER 6

CONCLUSIONS

The goal of one day using plasmonic devices and circuitry as a real answer to the future problems of electronic device performance and miniaturization is a difficult one to reach. The research presented, reveals many unique and beneficial characteristics for the propagation of energy in chain waveguides via sub-radiant modes.

First, the chain structure itself is quite versatile. The chain structure is created by filling trenches made by electron beam lithography with small metallic NPs, followed by a polymer lift-off procedure. As demonstrated by the study of straight and bent Ag NP chains, the chains can be made into any complex design by simply changing the design used in e-beam lithography. Further the filling technique used in this study was rather simple and was performed under normal laboratory conditions. For this reason several topics may be addressed in future work for optimized filling of the trenches, such as temperature and humidity to control the evaporation rate of the droplet, surface functionalization to increase the efficiency of the NP deposition, and investigation into the NP size and its effect on efficient trench filling.

Second, despite the issues mentioned above for chain creation, not addressed in this work, multi-layered, tightly packed chain structures were still able to be created and studied with the use of BlIPP, and demonstrated excellent waveguiding properties in comparison to their solid NW counterparts. Using BlIPP, we were able to measure long propagation lengths for Au NP chains and Ag NP chains. These long propagation lengths were attributed to the coupling of light to sub-radiant propagating modes of the structure.

When coupled to these modes, radiative channels of energy losses are suppressed resulting in longer propagation lengths for the waveguide. Further, we were able to demonstrate the highly efficient propagation of energy, through these sub-radiant modes around bent chain structures with no significant bending losses. These results are highly promising for future plasmonic applications in electronic devices as the chain structures may be written into any complex structure and our findings support the idea that even in such configurations, plasmon propagation in chains will not be negatively affected. The propagation length of chains might also be optimized by exploring NP size, NP material, and the use of tunable nanoshells rather than solid NPs as used in these studies.

Perhaps the most important contribution of this research to the field as a whole is the development of the BlIPP method used to characterize the propagation lengths of these waveguides. Several new waveguide structures with various geometries and materials are developed every year, with this research we reveal a new addition to the tools for propagation length measurement and comparison. BlIPP may be performed on any fluorescence confocal microscope imaging setup with no need for other specialized equipment so long as the dye is correctly chosen for the excitation wavelength.

In the future, BlIPP studies on other complex chain structures will be important such as the study of plasmon propagation in Y structures where the energy is split, and more importantly in logic systems where phase interference of the propagating plasmon may result in selective and predictable emission or non emission of light from particular waveguide branches.

Bibliography

(1) Ozbay, E. Plasmonics: Merging Photonics and Electronics at Nanoscale Dimensions. *Science* **2006,** 311, (5758), 189-193.

(2) Brongersma, M. L.; Shalaev, V. M. The Case for Plasmonics. *Science* **2010,** 328, (5977), 440-441.

(3) Guo, L. J. Nanoimprint Lithography: Methods and Material Requirements. *Adv. Mater.* **2007,** 19, (4), 495-513.

(4) Vieu, C.; Carcenac, F.; Pepin, A.; Chen, Y.; Mejias, M.; Lebib, A.; Manin-Ferlazzo, L.; Couraud, L.; Launois, H. Electron Beam Lithography: Resolution Limits and Applications. *Appl. Surf. Sci.* **2000,** 164, 111-117.

(5) Kish, L. B. End of Moore's Law: Thermal (Noise) Death of Integration in Micro and Nano Electronics. *Phys. Lett. A* **2002,** 305, (3-4), 144-149.

(6) Wang, K. L. Issues of Nanoelectronics: A Possible Roadmap. *J. Nanosci. Nanotechnol.* **2002,** 2, (3-4), 235-266.

(7) Haurylau, M.; Chen, G. Q.; Chen, H.; Zhang, J. D.; Nelson, N. A.; Albonesi, D. H.; Friedman, E. G.; Fauchet, P. M. On-Chip Optical Interconnect Roadmap: Challenges and Critical Directions. *IEEE J. Sel. Top. Quantum Electron.* **2006,** 12, (6), 1699-1705.

(8) Beyond the Diffraction Limit. *Nat Photon* **2009,** 3, (7), 361-361.

(9) Gramotnev, D. K.; Bozhevolnyi, S. I. Plasmonics Beyond the Diffraction Limit. *Nat. Photon.* **2010,** 4, (2), 83-91.

(10) Maier, S. A.; Atwater, H. A. Plasmonics: Localization and Guiding of Electromagnetic Energy in Metal/Dielectric Structures. *J. Appl. Phys.* **2005,** 98, (1).

(11) Lal, S.; Hafner, J. H.; Halas, N. J.; Link, S.; Nordlander, P. Noble Metal Nanowires: From Plasmon Waveguides to Passive and Active Devices. *Accounts of Chemical Research* **2012,** 45, (11), 1887-95.

(12) Barnes, W. L.; Dereux, A.; Ebbesen, T. W. Surface Plasmon Subwavelength Optics. *Nature* **2003,** 424, (6950), 824-830.

(13) Bozhevolnyi, S. I.; Volkov, V. S.; Devaux, E.; Ebbesen, T. W. Channel Plasmon-Polariton Guiding by Subwavelength Metal Grooves. *Phys. Rev. Lett.* **2005,** 95, (4).

(14) Oulton, R. F.; Sorger, V. J.; Genov, D. A.; Pile, D. F. P.; Zhang, X. A Hybrid Plasmonic Waveguide for Subwavelength Confinement and Long-Range Propagation. *Nat. Photon.* **2008,** 2, (8), 496-500.

(15) Boltasseva, A.; Nikolajsen, T.; Leosson, K.; Kjaer, K.; Larsen, M. S.; Bozhevolnyi, S. I. Integrated Optical Components Utilizing Long-Range Surface Plasmon Polaritons. *J. Lightwave Technol.* **2005,** 23, (1), 413-422.

(16) Berini, P.; Charbonneau, R.; Lahoud, N.; Mattiussi, G. Characterization of Long-Range Surface-Plasmon-Polariton Waveguides. *J. Appl. Phys.* **2005,** 98, (4).

(17) Kelly, K. L.; Coronado, E.; Zhao, L. L.; Schatz, G. C. The Optical Properties of Metal Nanoparticles: The Influence of Size, Shape, and Dielectric Environment. *J. Phys. Chem. B* **2003,** 107, (3), 668-677.

(18) Schuller, J. A.; Barnard, E. S.; Cai, W. S.; Jun, Y. C.; White, J. S.; Brongersma, M. L. Plasmonics for Extreme Light Concentration and Manipulation. *Nat. Mater.* **2010,** 9, (3), 193-204.

(19) Hess, O.; Pendry, J. B.; Maier, S. A.; Oulton, R. F.; Hamm, J. M.; Tsakmakidis, K. L. Active Nanoplasmonic Metamaterials. *Nat Mater* **2012,** 11, (7), 573-584.

(20) Krenn, J. R.; Lamprecht, B.; Ditlbacher, H.; Schider, G.; Salerno, M.; Leitner, A.; Aussenegg, F. R. Non-Diffraction-Limited Light Transport by Gold Nanowires. *Europhys. Lett.* **2002,** 60, (5), 663-669.

(21) Krenn, J. R.; Weeber, J. C. Surface Plasmon Polaritons in Metal Stripes and Wires. *Philos. Trans. R. Soc. Lond. Ser. A-Math. Phys. Eng. Sci.* **2004,** 362, (1817), 739-756.

(22) Lamprecht, B.; Krenn, J. R.; Schider, G.; Ditlbacher, H.; Salerno, M.; Felidj, N.; Leitner, A.; Aussenegg, F. R.; Weeber, J. C. Surface Plasmon Propagation in Microscale Metal Stripes. *Appl. Phys. Lett.* **2001,** 79, (1), 51-53.

(23) Bozhevolnyi, S. I.; Volkov, V. S.; Devaux, E. s.; Laluet, J.-Y.; Ebbesen, T. W. Channel Plasmon Subwavelength Waveguide Components Including Interferometers and Ring Resonators. *Nature* **2006,** 440, (7083), 508-511.

(24) Volkov, V. S.; Gosciniak, J.; Bozhevolnyi, S. I.; Rodrigo, S. G.; Martin-Moreno, L.; Garcia-Vidal, F. J.; Devaux, E.; Ebbesen, T. W. Plasmonic Candle: Towards Efficient Nanofocusing with Channel Plasmon Polaritons. *New J. Phys.* **2009,** 11.

(25) Sanders, A. W.; Routenberg, D. A.; Wiley, B. J.; Xia, Y. N.; Dufresne, E. R.; Reed, M. A. Observation of Plasmon Propagation, Redirection, and Fan-out in Silver Nanowires. *Nano Lett.* **2006,** 6, (8), 1822-1826.

(26) Paul, A.; Solis, D., Jr.; Bao, K.; Chang, W. S.; Nauert, S.; Vidgerman, L.; Zubarev, E. R.; Nordlander, P.; Link, S. Identification of Higher Order Long-Propagation-Length Surface Plasmon Polariton Modes in Chemically Prepared Gold Nanowires. *ACS Nano* **2012,** 6, (9), 8105-13.

(27) Solis, D., Jr.; Chang, W.-S.; Khanal, B. P.; Bao, K.; Nordlander, P.; Zubarev, E. R.; Link, S. Bleach-Imaged Plasmon Propagation (Blipp) in Single Gold Nanowires. *Nano Lett.* **2010,** 10, (9), 3482-3485.

(28) Wild, B.; Cao, L. N.; Sun, Y. G.; Khanal, B. P.; Zubarev, E. R.; Gray, S. K.; Scherer, N. F.; Pelton, M. Propagation Lengths and Group Velocities of Plasmons in Chemically Synthesized Gold and Silver Nanowires. *ACS Nano* **2012,** 6, (1), 472-482.

(29) Solis, D., Jr.; Willingham, B.; Nauert, S. L.; Slaughter, L. S.; Olson, J.; Swanglap, P.; Paul, A.; Chang, W.-S.; Link, S. Electromagnetic Energy Transport in Nanoparticle Chains Via Dark Plasmon Modes. *Nano Lett.* **2012,** 12, (3), 1349-53.

(30) Willingham, B.; Link, S. Energy Transport in Metal Nanoparticle Chains Via Sub-Radiant Plasmon Modes. *Opt. Express* **2011,** 19, (7), 6450-6461.

(31) Maier, S. A.; Brongersma, M. L.; Kik, P. G.; Meltzer, S.; Requicha, A. A. G.; Atwater, H. A. Plasmonics - a Route to Nanoscale Optical Devices. *Adv. Mater.* **2001,** 13, (19), 1501-1505.

(32) Maier, S. A.; Kik, P. G.; Atwater, H. A.; Meltzer, S.; Harel, E.; Koel, B. E.; Requicha, A. A. G. Local Detection of Electromagnetic Energy Transport Below the Diffraction Limit in Metal Nanoparticle Plasmon Waveguides. *Nat. Mater.* **2003,** 2, (4), 229-232.

(33) Raether, H., *Surface-Plasmons on Smooth and Rough Surfaces and on Gratings*. Springer: New York, 1988.

(34) Barnes, W. L. Surface Plasmon-Polariton Length Scales: A Route to Sub-Wavelength Optics. *J. Opt. A: Pure Appl. Opt.* **2006,** 8, (4), S87-S93.

(35) Han, Z. H.; Bozhevolnyi, S. I. Radiation Guiding with Surface Plasmon Polaritons. *Rep. Prog. Phys.* **2013,** 76, (1), 16402-16402.

(36) Staleva, H.; Skrabalak, S. E.; Carey, C. R.; Kosel, T.; Xia, Y. N.; Hartland, G. V. Coupling to Light, and Transport and Dissipation of Energy in Silver Nanowires. *Phys. Chem. Chem. Phys.* **2009,** 11, (28), 5889-5896.

(37) Dickson, R. M.; Lyon, L. A. Unidirectional Plasmon Propagation in Metallic Nanowires. *J. Phys. Chem. B* **2000,** 104, (26), 6095-6098.

(38) Knight, M. W.; Grady, N. K.; Bardhan, R.; Hao, F.; Nordlander, P.; Halas, N. J. Nanoparticle-Mediated Coupling of Light into a Nanowire. *Nano Lett.* **2007,** 7, (8), 2346-2350.

(39) Fang, Z. Y.; Lu, Y. W.; Lin, C. F.; Zhu, X. Antenna-Mediated Coupling of Light into Ag Nanowire. *J. Nanosci. Nanotechnol.* **2010,** 10, (11), 7171-7174.

(40) Ditlbacher, H.; Hohenau, A.; Wagner, D.; Kreibig, U.; Rogers, M.; Hofer, F.; Aussenegg, F. R.; Krenn, J. R. Silver Nanowires as Surface Plasmon Resonators. *Phys. Rev. Lett.* **2005,** 95, (25), 257403.

(41) Dorfmuller, J.; Vogelgesang, R.; Weitz, R. T.; Rockstuhl, C.; Etrich, C.; Pertsch, T.; Lederer, F.; Kern, K. Fabry-Perot Resonances in One-Dimensional Plasmonic Nanostructures. *Nano Lett.* **2009,** 9, (6), 2372-2377.

(42) Grandidier, J.; Des Francs, G. C.; Massenot, S.; Bouhelier, A.; Markey, L.; Weeber, J. C.; Dereux, A. Leakage Radiation Microscopy of Surface Plasmon Coupled Emission: Investigation of Gain-Assisted Propagation in an Integrated Plasmonic Waveguide. *J. Microsc.* **2010,** 239, (2), 167-72.

(43) Ditlbacher, H.; Krenn, J. R.; Felidj, N.; Lamprecht, B.; Schider, G.; Salerno, M.; Leitner, A.; Aussenegg, F. R. Fluorescence Imaging of Surface Plasmon Fields. *Appl. Phys. Lett.* **2002,** 80, (3), 404-406.

(44) Solis, D.; Paul, A.; Chang, W.-S.; Link, S. Mechanistic Study of Bleach-Imaged Plasmon Propagation (Blipp). *J. Phys. Chem. B* **2012**.

(45) Volkov, V. S.; Bozhevolnyi, S. I.; Devaux, E.; Ebbesen, T. W. Bend Loss for Channel Plasmon Polaritons. *Appl. Phys. Lett.* **2006,** 89, (14).

(46) Flynn, R. A.; Bussmann, K.; Simpkins, B. S.; Vurgaftman, I.; Kim, C. S.; Long, J. P. Propagation Length of Surface Plasmon Polaritons Determined by Emission from Introduced Surface Discontinuities. *J. Appl. Phys.* **2010,** 107, (1).

(47) Song, M. X.; Bouhelier, A.; Bramant, P.; Sharma, J.; Dujardin, E.; Zhang, D. G.; Colas-des-Francs, G. Imaging Symmetry-Selected Corner Plasmon Modes in Penta-Twinned Crystalline Ag Nanowires. *ACS Nano* 5, (7), 5874-5880.

(48) Wei, H.; Li, Z. P.; Tian, X. R.; Wang, Z. X.; Cong, F. Z.; Liu, N.; Zhang, S. P.; Nordlander, P.; Halas, N. J.; Xu, H. X. Quantum Dot-Based Local Field Imaging Reveals Plasmon-Based Interferometric Logic in Silver Nanowire Networks. *Nano Lett.* **2011,** 11, (2), 471-475.

(49) Huang, J.-S.; Callegari, V.; Geisler, P.; Bruning, C.; Kern, J.; Prangsma, J. C.; Wu, X.; Feichtner, T.; Ziegler, J.; Weinmann, P.; Kamp, M.; Forchel, A.; Biagioni, P.;

Sennhauser, U.; Hecht, B. Atomically Flat Single-Crystalline Gold Nanostructures for Plasmonic Nanocircuitry. *Nat. Commun.* **2010,** 1, 150.

(50) Khanal, B. P.; Zubarev, E. R. Purification of High Aspect Ratio Gold Nanorods: Complete Removal of Platelets. *J. Am. Chem. Soc.* **2008,** 130, (38), 12634-12635.

(51) Critchley, K.; Khanal, B. P.; Górzny, M. Ł.; Vigderman, L.; Evans, S. D.; Zubarev, E. R.; Kotov, N. A. Near-Bulk Conductivity of Gold Nanowires as Nanoscale Interconnects and the Role of Atomically Smooth Interface. *Adv. Mater.* **2010,** 22, (21), 2338-2342.

(52) Yan, Z. J.; Jureller, J. E.; Sweet, J.; Guffey, M. J.; Pelton, M.; Scherer, N. F. Three-Dimensional Optical Trapping and Manipulation of Single Silver Nanowires. *Nano Lett.* **2012,** 12, (10), 5155-5161.

(53) Yan, Z. J.; Sweet, J.; Jureller, J. E.; Guffey, M. J.; Pelton, M.; Scherert, N. F. Controlling the Position and Orientation of Single Silver Nanowires on a Surface Using Structured Optical Fields. *ACS Nano* **2012,** 6, (9), 8144-8155.

(54) Weeber, J. C.; Gonzalez, M. U.; Baudrion, A. L.; Dereux, A. Surface Plasmon Routing Along Right Angle Bent Metal Strips. *Appl. Phys. Lett.* **2005,** 87, (22).

(55) Cui, Y.; Bjork, M. T.; Liddle, J. A.; Sonnichsen, C.; Boussert, B.; Alivisatos, A. P. Integration of Colloidal Nanocrystals into Lithographically Patterned Devices. *Nano Lett.* **2004,** 4, (6), 1093-1098.

(56) Malaquin, L.; Kraus, T.; Schmid, H.; Delamarche, E.; Wolf, H. Controlled Particle Placement through Convective and Capillary Assembly. *Langmuir* **2007,** 23, (23), 11513-11521.

(57) Slaughter, L. S.; Willingham, B. A.; Chang, W.-S.; Chester, M. H.; Ogden, N.; Link, S. Toward Plasmonic Polymers. *Nano Lett.* **2012,** 12, (8), 3967-3972.

(58) Yan, R. X.; Pausauskie, P.; Huang, J. X.; Yang, P. D. Direct Photonic-Plasmonic Coupling and Routing in Single Nanowires. *Proc. Natl. Acad. Sci. U. S. A.* **2009,** 106, (50), 21045-21050.

(59) Li, Z. P.; Bao, K.; Fang, Y. R.; Huang, Y. Z.; Nordlander, P.; Xu, H. X. Correlation between Incident and Emission Polarization in Nanowire Surface Plasmon Waveguides. *Nano Lett.* **2010,** 10, (5), 1831-1835.

(60) Johnson, P. B.; Christy, R. W. Optical Constants of the Noble Metals. *Phys. Rev. B* **1972,** 6, (12), 4370.

(61) Wiley, B. J.; Lipomi, D. J.; Bao, J. M.; Capasso, F.; Whitesides, G. M. Fabrication of Surface Plasmon Resonators by Nanoskiving Single-Crystalline Gold Microplates. *Nano Lett.* **2008,** 8, (9), 3023-3028.

(62) Allione, M.; Temnov, V. V.; Fedutik, Y.; Woggon, U.; Artemyev, M. V. Surface Plasmon Mediated Interference Phenomena in Low-Q Silver Nanowire Cavities. *Nano Lett.* **2008,** 8, (1), 31-35.

(63) Verhagen, E.; Spasenovic, M.; Polman, A.; Kuipers, L. Nanowire Plasmon Excitation by Adiabatic Mode Transformation. *Phys. Rev. Lett.* **2009,** 102, (20), 4.

(64) Douillard, L.; Charra, F.; Korczak, Z.; Bachelot, R.; Kostcheev, S.; Lerondel, G.; Adam, P. M.; Royer, P. Short Range Plasmon Resonators Probed by Photoemission Electron Microscopy. *Nano Lett.* **2008,** 8, (3), 935-940.

(65) Graff, A.; Wagner, D.; Ditlbacher, H.; Kreibig, U. Silver Nanowires. *Eur. Phys. J. D.* **2005,** 34, (1-3), 263-269.

(66) Anger, P.; Bharadwaj, P.; Novotny, L. Enhancement and Quenching of Single-Molecule Fluorescence. *Phys. Rev. Lett.* **2006,** 96, (11), 113002.

(67) Chen, Y.; Munechika, K.; Ginger, D. S. Dependence of Fluorescence Intensity on the Spectral Overlap between Fluorophores and Plasmon Resonant Single Silver Nanoparticles. *Nano Lett.* **2007,** 7, (3), 690-696.

(68) Chan, Y. H.; Chen, J. X.; Wark, S. E.; Skiles, S. L.; Son, D. H.; Batteas, J. D. Using Patterned Arrays of Metal Nanoparticles to Probe Plasmon Enhanced Luminescence of Cdse Quantum Dots. *ACS Nano* **2009,** 3, (7), 1735-1744.

(69) Kinkhabwala, A.; Yu, Z. F.; Fan, S. H.; Avlasevich, Y.; Mullen, K.; Moerner, W. E. Large Single-Molecule Fluorescence Enhancements Produced by a Bowtie Nanoantenna. *Nat. Photon.* **2009,** 3, (11), 654-657.

(70) Seelig, J.; Leslie, K.; Renn, A.; Kuhn, S.; Jacobsen, V.; van de Corput, M.; Wyman, C.; Sandoghdar, V. Nanoparticle-Induced Fluorescence Lifetime Modification as Nanoscopic Ruler: Demonstration at the Single Molecule Level. *Nano Lett.* **2007,** 7, (3), 685-689.

(71) Akimov, A. V.; Mukherjee, A.; Yu, C. L.; Chang, D. E.; Zibrov, A. S.; Hemmer, P. R.; Park, H.; Lukin, M. D. Generation of Single Optical Plasmons in Metallic Nanowires Coupled to Quantum Dots. *Nature* **2007,** 450, (7168), 402-406.

(72) Fedutik, Y.; Temnov, V. V.; Schops, O.; Woggon, U.; Artemyev, M. V. Exciton-Plasmon-Photon Conversion in Plasmonic Nanostructures. *Phys. Rev. Lett.* **2007,** 99, (13), 4.

(73) Wei, H.; Ratchford, D.; Li, X. Q.; Xu, H. X.; Shih, C. K. Propagating Surface Plasmon Induced Photon Emission from Quantum Dots. *Nano Lett.* **2009,** 9, (12), 4168-4171.

(74) Noginov, M. A.; Zhu, G.; Belgrave, A. M.; Bakker, R.; Shalaev, V. M.; Narimanov, E. E.; Stout, S.; Herz, E.; Suteewong, T.; Wiesner, U. Demonstration of a Spaser-Based Nanolaser. *Nature* **2009,** 460, (7259), 1110-1112.

(75) Boltasseva, A.; Atwater, H. A. Low-Loss Plasmonic Metamaterials. *Science* **2011,** 331, (6015), 290-291.

(76) Soukoulis, C. M.; Wegener, M. Optical Metamaterials -- More Bulky and Less Lossy. *Science* **2010,** 330, (6011), 1633-1634.

(77) Vlasov, Y. A.; O'Boyle, M.; Hamann, H. F.; McNab, S. J. Active Control of Slow Light on a Chip with Photonic Crystal Waveguides. *Nature* **2005,** 438, (7064), 65-69.

(78) Gather, M. C.; Meerholz, K.; Danz, N.; Leosson, K. Net Optical Gain in a Plasmonic Waveguide Embedded in a Fluorescent Polymer. *Nat. Photon.* **2010,** 4, (7), 457-461.

(79) De Leon, I.; Berini, P. Amplification of Long-Range Surface Plasmons by a Dipolar Gain Medium. *Nat. Photon.* **2010,** 4, (6), 382-387.

(80) Stockman, M. I. Criterion for Negative Refraction with Low Optical Losses from a Fundamental Principle of Causality. *Phys. Rev. Lett.* **2007,** 98, (17), 177404.

(81) Vakil, A.; Engheta, N. Transformation Optics Using Graphene. *Science* **2011,** 332, (6035), 1291-1294.

(82) Oulton, R. F.; Sorger, V. J.; Zentgraf, T.; Ma, R. M.; Gladden, C.; Dai, L.; Bartal, G.; Zhang, X. Plasmon Lasers at Deep Subwavelength Scale. *Nature* **2009,** 461, (7264), 629-632.

(83) Walters, R. J.; van Loon, R. V. A.; Brunets, I.; Schmitz, J.; Polman, A. A Silicon-Based Electrical Source of Surface Plasmon Polaritons. *Nat. Mater.* **2010,** 9, (1), 21-25.

(84) Koller, D. M.; Hohenau, A.; Ditlbacher, H.; Galler, N.; Reil, F.; Aussenegg, F. R.; Leitner, A.; List, E. J. W.; Krenn, J. R. Organic Plasmon-Emitting Diode. *Nat. Photon.* **2008,** 2, (11), 684-687.

(85) Brongersma, M. L.; Hartman, J. W.; Atwater, H. A. Electromagnetic Energy Transfer and Switching in Nanoparticle Chain Arrays Below the Diffraction Limit. *Phys. Rev. B* **2000,** 62, (24), 16356-16359.

(86) Barrow, S. J.; Funston, A. M.; Gomez, D. E.; Davis, T. J.; Mulvaney, P. Surface Plasmon Resonances in Strongly Coupled Gold Nanosphere Chains from Monomer to Hexamer. *Nano Lett.* **2011,** 11, (10), 4180-4187.

(87) Braun, G. B.; Lee, S. J.; Laurence, T.; Fera, N.; Fabris, L.; Bazan, G. C.; Moskovits, M.; Reich, N. O. Generalized Approach to Sers-Active Nanomaterials Via Controlled Nanoparticle Linking, Polymer Encapsulation, and Small-Molecule Infusion. *J. Phys. Chem. C* **2009,** 113, (31), 13622-13629.

(88) Yin, Y.; Lu, Y.; Gates, B.; Xia, Y. Template-Assisted Self-Assembly: A Practical Route to Complex Aggregates of Monodispersed Colloids with Well-Defined Sizes, Shapes, and Structures. *J. Am. Chem. Soc.* **2001,** 123, (36), 8718-8729.

(89) Chang, W. S.; Slaughter, L. S.; Khanal, B. P.; Manna, P.; Zubarev, E. R.; Link, S. One-Dimensional Coupling of Gold Nanoparticle Plasmons in Self-Assembled Ring Superstructures. *Nano Lett.* **2009,** 9, (3), 1152-1157.

(90) Liu, K.; Nie, Z.; Zhao, N.; Li, W.; Rubinstein, M.; Kumacheva, E. Step-Growth Polymerization of Inorganic Nanoparticles. *Science* **2010,** 329, (5988), 197-200.

(91) Nie, Z.; Fava, D.; Kumacheva, E.; Zou, S.; Walker, G. C.; Rubinstein, M. Self-Assembly of Metal-Polymer Analogues of Amphiphilic Triblock Copolymers. *Nat. Mater.* **2007,** 6, (8), 609-614.

(92) Fan, J. A.; Wu, C. H.; Bao, K.; Bao, J. M.; Bardhan, R.; Halas, N. J.; Manoharan, V. N.; Nordlander, P.; Shvets, G.; Capasso, F. Self-Assembled Plasmonic Nanoparticle Clusters. *Science* **2010,** 328, (5982), 1135-1138.

(93) Chen, J. I. L.; Chen, Y.; Ginger, D. S. Plasmonic Nanoparticle Dimers for Optical Sensing of DNA in Complex Media. *J. Am. Chem. Soc.* **2010,** 132, (28), 9600-9601.

(94) Kawata, S.; Ono, A.; Verma, P. Subwavelength Colour Imaging with a Metallic Nanolens. *Nat. Photon.* **2008,** 2, (7), 438-442.

(95) Liu, M.; Lee, T.-W.; Gray, S. K.; Guyot-Sionnest, P.; Pelton, M. Excitation of Dark Plasmons in Metal Nanoparticles by a Localized Emitter. *Phys. Rev. Lett.* **2009,** 102, (10), 107401.

(96) Nordlander, P. Plasmonics: Subwavelength Imaging in Colour. *Nat. Photon.* **2008,** 2, (7), 387-388.

(97) Chen, H.-Y.; He, C.-L.; Wang, C.-Y.; Lin, M.-H.; Mitsui, D.; Eguchi, M.; Teranishi, T.; Gwo, S. Far-Field Optical Imaging of a Linear Array of Coupled

Gold Nanocubes: Direct Visualization of Dark Plasmon Propagating Modes. *ACS Nano* **2011,** 5, (10), 8223-8229.

(98) Stockman, M. I. Nanoscience: Dark-Hot Resonances. *Nature* **2010,** 467, (7315), 541-542.

(99) Gerardy, J. M.; Ausloos, M. Absorption Spectrum of Clusters of Spheres from the General Solution of Maxwell's Equations. Ii. Optical Properties of Aggregated Metal Spheres. *Phys. Rev. B* **1982,** 25, (6), 4204-4229.

(100) Doicu, A.; Wriedt, T. Computation of the Beam-Shape Coefficients in the Generalized Lorenz-Mie Theory by Using the Translational Addition Theorem for Spherical Vector Wave Functions. *Appl. Opt.* **1997,** 36, (13), 2971-2978.

(101) Lubachevsky, B. D.; Stillinger, F. H. Geometric-Properties of Random Disk Packings. *J. Stat. Phys.* **1990,** 60, (5-6), 561-583.

(102) Lubachevsky, B. D.; Stillinger, F. H.; Pinson, E. N. Disks Vs Spheres - Contrasting Properties of Random Packings. *J. Stat. Phys.* **1991,** 64, (3-4), 501-524.

(103) Berkovitch, N.; Orenstein, M. Thin Wire Shortening of Plasmonic Nanoparticle Dimers: The Reason for Red Shifts. *Nano Lett.* **2011,** 11, (5), 2079-2082.

(104) Citrin, D. S.; Wang, Y.; Zhou, Z. P. Far-Field Optical Coupling to Semi-Infinite Metal-Nanoparticle Chains. *J. Opt. Soc. Am. B-Opt. Phys.* **2008,** 25, (6), 937-944.

(105) Bouhelier, A.; Wiederrecht, G. P. Surface Plasmon Rainbow Jets. *Opt. Lett.* **2005,** 30, (8), 884-886.

(106) Maier, S., *Plasmonics: Fundamentals and Applications*. Springer: New York, 2007.

(107) Hentschel, M.; Saliba, M.; Vogelgesang, R.; Giessen, H.; Alivisatos, A. P.; Liu, N. Transition from Isolated to Collective Modes in Plasmonic Oligomers. *Nano Lett.* **2010,** 10, (7), 2721-2726.

(108) Markel, V. A.; Sarychev, A. K. Propagation of Surface Plasmons in Ordered and Disordered Chains of Metal Nanospheres. *Phys. Rev. B* **2007,** 75, (8), 085426/1-11.

(109) Levi, L.; Rechtsman, M.; Freedman, B.; Schwartz, T.; Manela, O.; Segev, M. Disorder-Enhanced Transport in Photonic Quasicrystals. *Science* **2011,** 332, (6037), 1541-1544.

(110) Chanda, D.; Shigeta, K.; Gupta, S.; Cain, T.; Carlson, A.; Mihi, A.; Baca, A. J.; Bogart, G. R.; Braun, P.; Rogers, J. A. Large-Area Flexible 3d Optical Negative Index Metamaterial Formed by Nanotransfer Printing. *Nat. Nanotechnol.* **2011,** 6, (7), 402-407.

(111) Lal, S.; Link, S.; Halas, N. J. Nano-Optics from Sensing to Waveguiding. *Nat. Photon.* **2007,** 1, (11), 641-648.

(112) Nagpal, P.; Lindquist, N. C.; Oh, S.-H.; Norris, D. J. Ultrasmooth Patterned Metals for Plasmonics and Metamaterials. *Science* **2009,** 325, (5940), 594-597.

(113) Kolomenski, A.; Kolomenskii, A.; Noel, J.; Peng, S. Y.; Schuessler, H. Propagation Length of Surface Plasmons in a Metal Film with Roughness. *Appl. Opt.* **2009,** 48, (30), 5683-5691.

(114) Laroche, T.; Vial, A.; Roussey, M. Crystalline Structure's Influence on the near-Field Optical Properties of Single Plasmonic Nanowires. *Appl. Phys. Lett.* **2007,** 91, (12), 123101.

(115) Pyayt, A. L.; Wiley, B.; Xia, Y. N.; Chen, A.; Dalton, L. Integration of Photonic and Silver Nanowire Plasmonic Waveguides. *Nat. Nanotechnol.* **2008,** 3, (11), 660-665.

(116) Li, Z. P.; Bao, K.; Fang, Y. R.; Guan, Z. Q.; Halas, N. J.; Nordlander, P.; Xu, H. X. Effect of a Proximal Substrate on Plasmon Propagation in Silver Nanowires. *Phys. Rev. B* **2010,** 82, (24), 241402.

(117) Sridharan, D.; Waks, E.; Solomon, G.; Fourkas, J. T. Reversible Tuning of Photonic Crystal Cavities Using Photochromic Thin Films. *Appl. Phys. Lett.* **2010,** 96, (15), 153303.

(118) Ma, Y. G.; Li, X. Y.; Yu, H. K.; Tong, L. M.; Gu, Y.; Gong, Q. H. Direct Measurement of Propagation Losses in Silver Nanowires. *Opt. Lett.* **2010,** 35, (8), 1160-1162.

(119) Eggeling, C.; Volkmer, A.; Seidel, C. A. M. Molecular Photobleaching Kinetics of Rhodamine 6g by One- and Two-Photon Induced Confocal Fluorescence Microscopy. *ChemPhysChem* **2005,** 6, (5), 791-804.

(120) Zondervan, R.; Kulzer, F.; Kol'chenko, M. A.; Orrit, M. Photobleaching of Rhodamine 6g in Poly(Vinyl Alcohol) at the Ensemble and Single-Molecule Levels. *J. Phys. Chem. A* **2004,** 108, (10), 1657-1665.

(121) Dittrich, P. S.; Schwille, P. Photobleaching and Stabilization of Fluorophores Used for Single-Molecule Analysis with One- and Two-Photon Excitation. *Appl. Phys. B* **2001,** 73, (8), 829-837.

(122) Eggeling, C.; Widengren, J.; Rigler, R.; Seidel, C. A. M. Photobleaching of Fluorescent Dyes under Conditions Used for Single-Molecule Detection: Evidence of Two-Step Photolysis. *Anal. Chem.* **1998,** 70, (13), 2651-2659.

(123) Leong, K.; Chen, Y. C.; Masiello, D. J.; Zin, M. T.; Hnilova, M.; Ma, H.; Tamerler, C.; Sarikaya, M.; Ginger, D. S.; Jen, A. K. Y. Cooperative near-Field Surface Plasmon Enhanced Quantum Dot Nanoarrays. *Adv. Funct. Mater.* **2010,** 20, (16), 2675-2682.

(124) Lakowicz, J. R., *Principles of Fluorescence Spectroscopy*. 3 ed.; Springer Science: New York, 2006.

(125) Atkins;, P.; Paula, J. D., *Physical Chemistry for the Life Sciences*. 2 ed.; W. H. Freeman and Company: New York, 2011.

(126) Wennmalm, S.; Rigler, R. On Death Numbers and Survival Times of Single Dye Molecules. *J. Phys. Chem. B* **1999,** 103, (13), 2516-2519.

(127) Molski, A. Statistics of the Bleaching Number and the Bleaching Time in Single-Molecule Fluorescence Spectroscopy. *J. Chem. Phys.* **2001,** 114, (3), 1142-1147.

(128) Yeow, E. K. L.; Melnikov, S. M.; Bell, T. D. M.; De Schryver, F. C.; Hofkens, J. Characterizing the Fluorescence Intermittency and Photobleaching Kinetics of Dye Molecules Immobilized on a Glass Surface. *J. Phys. Chem. A* **2006,** 110, (5), 1726-1734.

(129) Zondervan, R.; Kulzer, F.; Orlinskii, S. B.; Orrit, M. Photoblinking of Rhodamine 6g in Poly(Vinyl Alcohol): Radical Dark State Formed through the Triplet. *J. Phys. Chem. A* **2003,** 107, (35), 6770-6776.

(130) Berglund, A. J. Nonexponential Statistics of Fluorescence Photobleaching. *J. Chem. Phys.* **2004,** 121, (7), 2899-2903.

(131) Prummer, M.; Weiss, M. Bulk Fluorescence Measurements Cannot Probe the Survival-Time Distribution of Single Molecules. *Phys. Rev. E* **2006,** 74, (2), 021115.

(132) Fureder-Kitzmuller, E.; Hesse, J.; Ebner, A.; Gruber, H. J.; Schutz, G. J. Non-Exponential Bleaching of Single Bioconjugated Cy5 Molecules. *Chem. Phys. Lett.* **2005,** 404, (1-3), 13-18.

(133) Kauranen, M.; Zayats, A. V. Nonlinear Plasmonics. *Nat. Photon.* **2012,** 6, (11), 737-748.

(134) Halas, N. J.; Lal, S.; Link, S.; Chang, W. S.; Natelson, D.; Hafner, J. H.; Nordlander, P. A Plethora of Plasmonics from the Laboratory for Nanophotonics at Rice University. *Adv. Mater.* **2012,** 24, (36), 4842-4877.

(135) Anderson, L. J. E.; Payne, C. M.; Zhen, Y. R.; Nordlander, P.; Hafner, J. H. A Tunable Plasmon Resonance in Gold Nanobelts. *Nano Lett.* **2011,** 11, (11), 5034-5037.

(136) Shegai, T.; Miljkovic, V. D.; Bao, K.; Xu, H. X.; Nordlander, P.; Johansson, P.; Kall, M. Unidirectional Broadband Light Emission from Supported Plasmonic Nanowires. *Nano Lett.* **2011,** 11, (2), 706-711.

(137) Steinberger, B.; Hohenau, A.; Ditlbacher, H.; Aussenegg, F. R.; Leitner, A.; Krenn, J. R. Dielectric Stripes on Gold as Surface Plasmon Waveguides: Bends and Directional Couplers. *Appl. Phys. Lett.* **2007,** 91, (8).

(138) Khurgin, J. B.; Sun, G. Practicality of Compensating the Loss in the Plasmonic Waveguides Using Semiconductor Gain Medium. *Appl. Phys. Lett.* **2012,** 100, (1).

(139) Wang, W. H.; Yang, Q.; Fan, F. R.; Xu, H. X.; Wang, Z. L. Light Propagation in Curved Silver Nanowire Plasmonic Waveguides. *Nano Lett.* **2011,** 11, (4), 1603-1608.

(140) Bozhevolnyi, S. I.; Volkov, V. S.; Leosson, K. Surface Plasmon Polariton Propagation Along a 90 Degrees Bent Line Defect in a Periodically Corrugated Metal Surface. *Opt. Commun.* **2001,** 196, (1-6), 41-45.

(141) Volkov, V. S.; Bozhevolnyi, S. I.; Devaux, E.; Ebbesen, T. W. Compact Gradual Bends for Channel Plasmon Polaritons. *Opt. Express* **2006,** 14, (10), 4494-4503.

(142) Hasegawa, K.; Nöckel, J. U.; Deutsch, M. Curvature-Induced Radiation of Surface Plasmon Polaritons Propagating around Bends. *Physical Review A* **2007,** 75, (6), 063816.

(143) Cui, W.; Zhu, Y.; Huang, W.; Li, H. Subwavelength Plasmon Solitons in a One-Dimensional Chain of Coupled Metallic Nanorods. *Phys. Rev. E* **2012,** 86, (6), 066604.

(144) Wang, M.; Cao, M.; Chen, X.; Gu, N. Subradiant Plasmon Modes in Multilayer Metal-Dielectric Nanoshells. *J. Phys. Chem. C* **2011,** 115, (43), 20920-20925.